Chirality control of mercury sulfide nanoparticles based on ligand coordination

久野純平

Contents

Chapter 1
Introduction: Chiral Chemistry of Inorganic Nanocrystals

1-1. Nanoscale chirality in inorganics.

Chirality is one of the most fascinating occurrences in the natural world and plays a crucial role in the fields of chemistry, biology, pharmacology, and medicine. The majority of chiral chemistry has been based on molecular science, ranging from small organic molecules, polymers, supramolecular assemblies, to metal complexes. Chirality is manifested in inorganic systems as well. A variety of inorganic crystals, such as quartz,[1,2] cinnabar,[3,4] $NaClO_3$,[5,6] selenium,[7,8] and tellurium[9,10] are known as chiral minerals with chiral crystalline structures. Since these minerals appear as a racemic mixture in nature, researchers have made efforts to synthesize them with controlled handedness.[4,7,9]

A relatively new field linking the properties of chirality with inorganic nanomaterials has emerged in 1998 with the first demonstration of optical activity in gold nanoclusters stabilized by L-glutathione as a chiral ligand, whereby circular dichroism (CD) was measured in electronic transitions of the inorganic gold core.[11] Many groups have subsequently reported the successful synthesis of optically active metal nanoclusters through the use of various chiral ligands, indicating the transfer of chiral information from the ligand to the nanocluster core.[12-17] A milestone in the field was the determination of the crystal structure of $Au_{102}(p\text{-MBA})_{44}$ (p-MBA = $para$-mercaptobenzoic acid), which showed a chiral pattern for the arrangement of the gold−sulfur staple motifs on the cluster surface despite the use of the achiral ligand (Figure 1-1a).[18] Interestingly, the asymmetric pattern of the ligands around the achiral Au core could generate a strong Cotton effect in CD.[19] Similarly, optical activity was also observed in $Au_{28}(SR)_{20}$, $Au_{38}(SR)_{24}$, and $Au_{40}(SR)_{24}$ (SR = achiral thiolate ligand) nanoclusters with a chiral arrangement of achiral ligands (Figure 1-1b).[20-24] Unlike bulk systems, the gold nanoclusters with the intrinsic chirality adopt lower symmetry chiral structures that would minimize their total energies.[12,25] Optical activity in metal nanoclusters can thus stem from a chiral electronic interaction between chiral ligands and achiral core or an intrinsically chiral atomic arrangement.[26,27] This proposed concept motivated researchers towards an enantioselective synthesis of other inorganic nanomaterials.
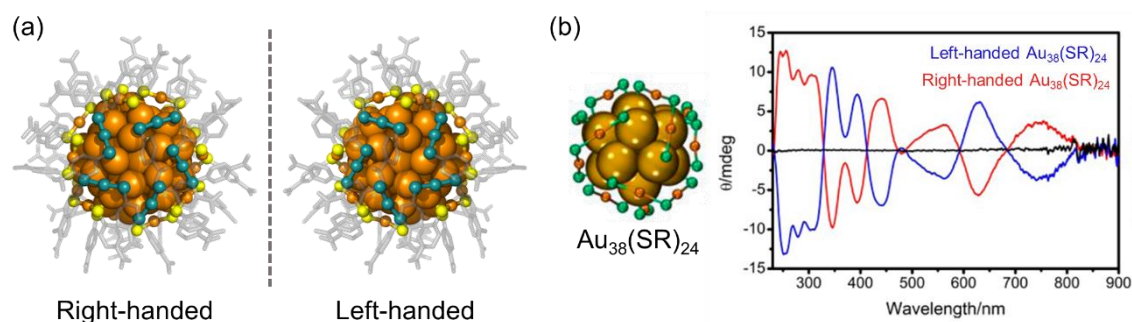
Figure 1-1. (a) Crystal structure of the $Au_{102}(p\text{-MBA})_{44}$ cluster. Au, orange; sulfur, yellow; other, gray; the five dimetric staples are highlighted in green.[19] (b) Crystal structure and CD spectra of the enantiomeric $Au_{38}(SR)_{24}$ cluster.[23] Au_{core}, yellow; Au_{adatom}, orange; sulfur, green.

1-2. Chiral semiconductor nanocrystals.

Semiconductor colloidal quantum dots (QDs) with size-dependent optical properties have been intensively studied for decades. The use of chiral stabilizing molecules has opened an exciting avenue in the area of QD research. In 2007, the first chiral semiconductor QDs, CdS QDs capped with penicillamine (Pen), were prepared by the use of microwave-induced heating in the presence of racemic (*rac*), D-, and L-Pen as stabilizers.[28] CD studies of these QDs have shown that D- and L-Pen stabilized QDs exhibited mirror image CD spectra, whereas the QDs with the *rac* mixture showed a negligible signal (Figure 1-2a).[28] The density functional theory (DFT) calculations of these electronic states have demonstrated that CD over 300 nm is associated with near-surface cadmium atoms that are enantiomerically distorted by chiral Pen ligands, while the QD core is found to remain undistorted and achiral (Figure 1-2b).[29] Later, chiral CdSe QDs,[30-32] CdTe QDs,[30,33] and chiral CdS nanotetrapods[34] capped with chiral ligands have been reported. All of the chiral nanostructures showed characteristic CD responses within the band-edge region of the spectra. From these studies, it was assumed that the ligand chirality could be translated to chiral surface defects resulting in chiroptical effects in QDs.[27,35,36] This concept of chirally distorted QD shell was confirmed in the experimental works, where CdTe QDs also exhibited optical activity even after ligand exchange from a chiral cysteine derivative (MeCys) to achiral 1-dodecanethiol (Figure 1-3).[30]
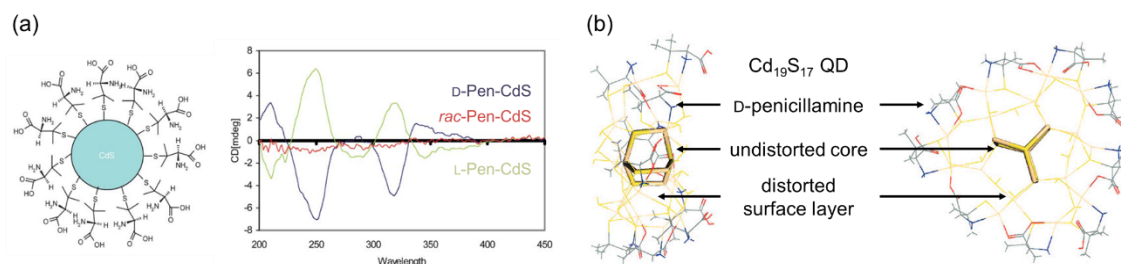
Figure 1-2. (a) Schematic presentation of the D-penicillamine stabilized CdS QDs and CD spectra of the D- (blue), L- (green) and *rac*-penicillamine stabilized CdS QDs.[28] (b) top and side views of optimized cluster model of CdS QDs covered with D-penicillamine.[29] (Cd, brown; S, yellow; C, grey; O, red; N, blue; thin lines, upper CdS layer and penicillamine; solid line, dipper CdS layer)
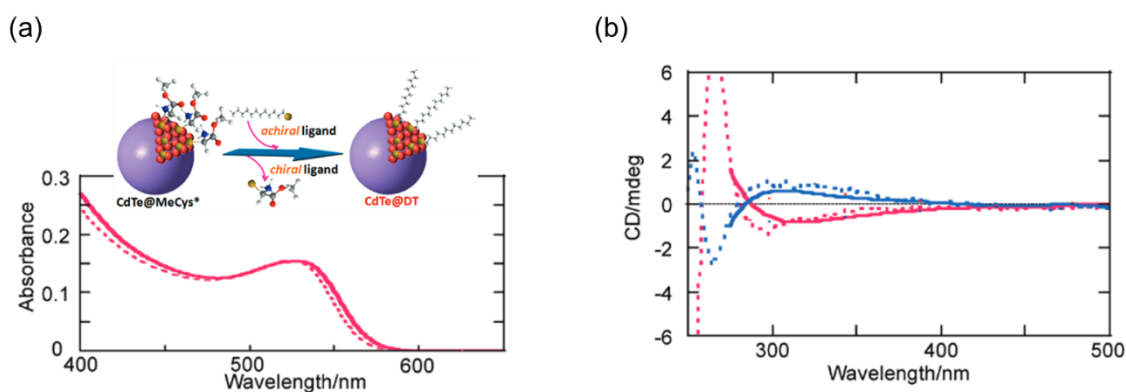
Figure 1-3. (a) Schematic illustration of ligand-exchange reaction from chiral to achiral ligand. (a) UV-vis absorption spectra of D-MeCys-capped CdTe QDs (dotted line) and dodecanthiol-capped CdTe QDs (solid line) after ligand exchange from D-MeCys.[30] (b) CD spectra of CdTe QDs before (dotted lines and after (solid lines) the ligand exchange from D-MeCys (red) and L-MeCys (blue).[30]

However, optical activity in QDs can arise from not necessarily only by chiral surface defects but also by other factors. Balaz and co-workers demonstrated that chiral capping ligands, D- and L-cysteine (Cys), induced circular dichroism in CdSe QDs with achiral core (Figure 1-4).[37] Cys-capped CdSe QDs prepared from the achiral triphenyl phosphine oxide (TOPO) oleic acid (OA)-capped QDs by post-synthetic ligand exchange exhibited mirror-image CD spectra in the visible region from 350 to 570 nm in response to the enantiomeric Cys ligands used for the post-synthetic ligand exchange. In addition, it was found that the CD profile and magnitude varied with the size of CdSe QDs.[38] They have also performed time dependent (TD) DFT calculations showing that the attachment of D- and L-Cys to the surface of model (CdSe)$_{13}$ nanoclusters can induce measurable opposite CD signals for the excitonic band of the nanocluster.[38] The origin of the induced chirality is consistent with the electronic hybridization of highest occupied CdSe molecular orbitals with those of the chiral Cys ligand.[38]

Following this initial work, the phenomenon of induced chiroptical activity in semiconductor QDs has been intensively studied to manipulate the optical activity of the QDs. The shape of CD spectra including CD intensity for chiral QDs depends on many factors, including the chemical composition (CdX X=S, Se, Te),[39,40] the size of the QD core,[38,41] QD shape,[40,42-44] thickness of the QD shell,[44-46] and coordination modes of the chiral ligands.[39,47-49]
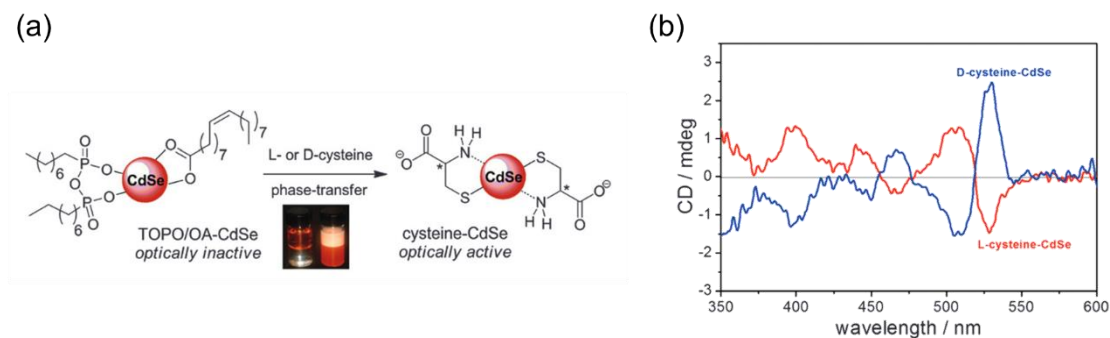

Figure 1-4. (a) Ligand exchange on achiral TOPO/OA-CdSe QDs using enantiomers of cysteine. Pictures: TOPO/OA-CdSe in toluene (left vial) and cysteine-CdSe in water (right vial).[37] (b) CD spectra of L-cysteine-CdSe (red) and D-cysteine-CdSe QDs (blue) after the ligand exchange. [37]

As explained above, the synthetic methods towards chiral semiconductor QDs are divided into two types which include direct synthesis in the presence of chiral ligands and post-modification of the QDs with chiral ligand molecules. Although many theoretical works on their chiral structure have been constructed to elucidate their optical activity, the absolute structure of chiral QDs has not yet been revealed. The chiral QDs with optical activity have exhibited many potential applications in the fields of biology, chemistry, and physics.[27,35,50] Yet, the optical activity of the currently reported QDs is far from satisfaction. It is still a challenge to prepare the chiral semiconductor nanoparticles (NPs) with giant optical activity.

1-3. Intrinsically chiral cinnabar mercury sulfide nanoparticles.

A new class of chiral inorganic NPs has emerged with the first synthetic demonstration by G. Markovich and co-workers of intrinsically chiral cinnabar (α-HgS) NPs (Figure 1-5), which crystallize in the chiral trigonal space group $P3_121$ (or its enantiomorph $P3_221$).[51] The use of the chiral Pen molecule led to the formation of chiral α-HgS NPs via the transient formation of the achiral phase of metacinnabar (β-HgS) NPs.[51-53] The enantiomeric molecule is considered to direct the preferential formation of one-handed cinnabar NPs, controlling the enantiomeric excess of NP ensembles. The obtained α-HgS NPs exhibit a strong chiroptical response arising from the crystallographic chirality of the inorganic core (Figure 1-5c). The dissymmetry factor ($\Delta\varepsilon/\varepsilon=\Delta A/A$) value in absorption, g_{abs}

($g_{abs} = \Delta\varepsilon/\varepsilon$), was 0.012,[51] which was several orders of magnitude larger than the optical activity of the aforementioned semiconductor QDs (CdS, CdSe, CdTe, and ZnSe) with intrinsically achiral crystalline systems. This report on the successful synthesis of α-HgS NPs proposed a new concept of inorganic NPs on the basis of chiral crystal symmetry groups. Many studies on intrinsically chiral NPs, such as Se,[54] Te,[54] TbPO$_4$·H$_2$O NPs,[55] have been succeeding.
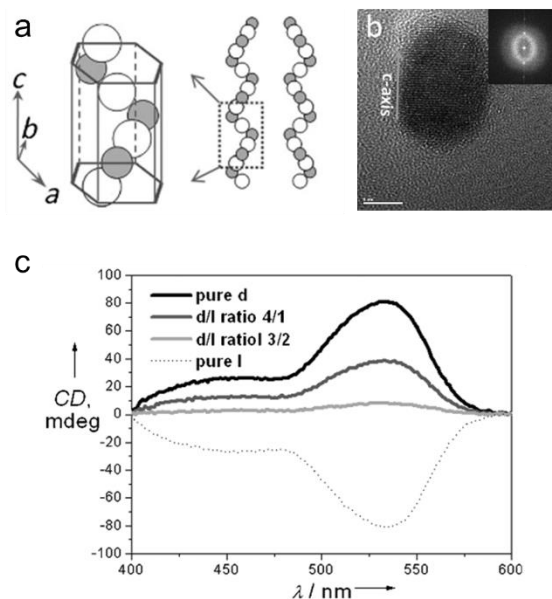
Figure 1-5. (a) Schematic illustration of the opposite Hg-S spirals with a fraction of one spiral reconstructed inside the frame of the hexagonal unit cell. (b) High-resolution TEM images of the individual α-HgS NP; arrow marks the c-axis direction of the NP,[51] Scale bar is 5 nm. (c) CD spectra of α-HgS NPs obtained at different molar ratio of D- and L-penicillamine.[51]

In more recent works, Ouyang and co-workers achieved the preparation of α-HgS nanostructures with independently controlled chiral crystalline lattice and chiral twisted morphology (Figure 1-6).[56,57] They demonstrated that both the crystallographic and morphological chirality of α-HgS nanotwists (NTs) have a definitive effect on the CD spectral profiles.[56] For the NTs, the CD activity around 540 nm is attributed to the crystallographic chirality, whereas one below 500 nm is determined by the interplay between chiral morphology and chiral lattice. Later, some other investigations have been performed to get a fundamental understanding of the optical activity of the α-HgS NPs because of their significant CD responses.[52,58,59] Meanwhile, the mechanism of how the crystallographic chirality in the core of NPs is controlled by surface chiral ligands had yet to be figured out.

Figure 1-6. (a) Schematic preparation of α-HgS NTs with both crystallographic and morphological chirality form α-HgS NPs. (b) High-resolution TEM images of α-HgS NTs with right-handed (left) and left-handed twisted morphology.[56]

1-4. Objectives and scope of this thesis.

The large variety of chiral inorganic nanomaterials has been emerging for only two decades and rapidly developed due to their significant chiral properties as discussed above.[27,35,50,53] Nevertheless, a central question in the field of nano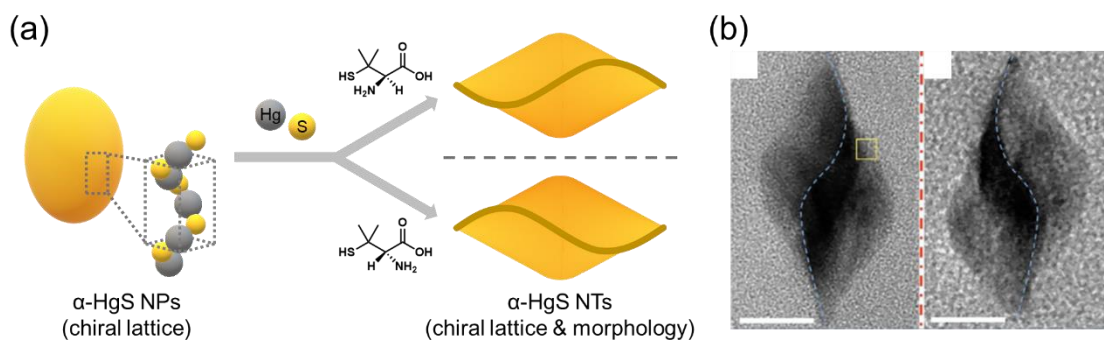scale chirality still remains unanswered: How does chirality transfer operate from a chiral ligand to an inorganic structure? I assumed that difficulty in the evaluation of detailed structures of such inorganic nanomaterials is the major issue. To the best of my knowledge, very limited studies have been reported to unveil their chiral structures[60] including gold and silver nanoclusters which afforded single crystals for X-ray analysis.[18-24] The X-ray crystal structures have enabled researchers to discuss the origin of chiral structure in the multiscale dimension in an unambiguous manner. In contrast, the detailed investigations on the structure of semiconductor NPs have mostly relied on transmission electron microscopy (TEM) since their sizes are suitable for the technique, and the finite size distribution prevents the formation of single crystals. However, even the high-resolution imaging technique is unable to shed light on the chiral defect or chiral arrangement of ligands on the surface, which have been considered to be one of the origins of chirality in NPs. In this dissertation work, I expected that the NPs composed of cinnabar (α-HgS) with an intrinsically chiral crystalline system could be an ideal model to discuss how the chirality of surface ligand operates on the controlled synthesis of chiral NPs and vice versa (how the chirality of the core operates on the surface ligands). The employment of intrinsically chiral inorganics makes the discussion simpler since their crystallographic structures adopt either of right- or left-handed chiral atomic arrangement. Furthermore, the giant chiroptical response originating from the crystallographic chirality is advantageous to explore the formation and temporal evolution of chiral NPs. It was also reported that the synthesis of α-HgS NPs proceeds via the transient formation of metastable β-HgS which could be monitored by the absorption spectral change.[51] I suppose that this β-to-α phase transition is a chirality

induction process in the NPs in which the presence of chiral ligands should have an effect.

In the intrinsically chiral nanomaterial systems, the chiral surface can be displayed at a low Miller index surface. These nanomaterials have attracted much interest as a chiral source, affording enantioselective processes such as a catalyst.[61,62] Nevertheless, there are few studies on chirality transfer from inorganic nanomaterials to adsorbed molecules on their surface.[63-67]

This thesis aims to (1) reveal the underlying mechanism to translate chirality of ligand molecules to HgS NPs, and (2) challenge the chirality transfer from chiral α-HgS NPs to surface ligand molecules.

The study of chiral α-HgS NPs is just at the infant stage with full of potential and challenges. In 2016, when I started this dissertation research, there was only one report on the chiral α-HgS NPs, which described the synthesis of the NPs with unknown enantioselectivity.[51] The thesis, therefore, proceeds first with a discussion of ligand effects on the optical activity and induction of chirality in HgS NPs (Chapter 2). The arrangement of chiral ligands on the NP surface through bidentate binding modes facilitates the chiral induction. Interestingly, a slight difference in chemical structures of chiral ligands with an identical stereochemistry (L-cysteine and N-acetyl-L-cysteine) resulted in the reversal of chirality in the α-HgS core. This result proposed that the difference in the bidentate coordination structures of chiral ligands could lead to chirality inversion. Moreover, a chiral memory effect of the NPs is also demonstrated by the ligand exchange with achiral ligands.

In Chapter 3, the optical activity inversion in the synthesis of α-HgS NPs using even an identical chiral ligand is shown. This inversion is considered to be triggered by a change in the coordination structures of N-acetyl-L-cysteine ligand on the NP surface. The mechanism of optical activity inversion is discussed through experimental and theoretical studies in Chapter 3. It is demonstrated that chiral molecules bind to the surface with nearly mirror-image configurations, which can give rise to the preferential formation of α-HgS with opposite handedness.

In Chapter 4, I discuss spontaneous amplification of enantioselectivity of the chiral α-HgS NPs in the Ostwald ripening process. It has been assumed that the use of chiral Pen ligand led to the highly enantioselective formation of α-HgS NPs by various groups.[51-53] However, the origin of high enantioselectivity had been unclear. Given the results in Chapter 3, the use of enantiopure ligands can not necessarily provide enantiopure α-HgS NPs with identical handedness. A detailed study on the formation and growth of the HgS NPs was conducted in Chapter 4, leading to a significant finding that the Ostwald ripening-aided growth amplifies enantioselectivity in the synthesis of α-HgS NPs.

In Chapter 5, I develop a new approach to generate CPL-active materials system composed of chiral inorganic NPs and achiral luminescent ligands. The achiral molecule adsorbed on the surface of α-HgS NTs (Figure 1-6) exhibited intense CPL signals, whereas no CPL was observed for the same ligand bound to the α-HgS NPs with achiral morphology. In addition, the handedness of the CPL can be controlled not by the crystallographic chirality but by the morphological chirality of the NTs. The achiral luminescent molecules are considered to be arranged in a chiral manner on the chiral-shaped

NT surface, resulting in CPL generation.

1-5. References.

1   A. D. Vries, Determination of the Absolute Configuration of α-Quartz, *Nature* **1958**, 181, 1193.

2   R. M. Hazen, D. S. Sholl, Chiral selection on inorganic crystalline surfaces, *Nature Mater.* **2003**, 2, 367–374.

3   K. L. Aurivillius, *Acta Chem. Scand.* **1950**, 4, 1413–1436.

4   A. R. Bungay, Y. P. Svirko, N. I. Zheludev, *Phys. Rev. Lett.* **1993**, 70, 3039–3042.

5   D. K. Kondepudi, R. J. Kaufman, N. Singh, Chiral Symmetry Breaking in Sodium Chlorate Crystallization, *Science* **1990**, 250, 975–976.

6   C. Viedma, Chiral Symmetry Breaking During Crystallization: Complete Chiral Purity Induced by Nonlinear Autocatalysis and Recycling, *Phys. Rev. Lett.* **2005**, 065504.

7   F. D. Saeva, G. R. Olin, J. Y. C. Chu, Circular Dichroism of Trigonal Selenium Formed in a Chiral Polymer Matrix, *Mol. Cryst. Liq. Cryst.* **1977**, 41, 5–9.

8   B. Gate, B. Mayers, B. Cattle, Y. Xia, Synthesis and characterization of uniform nanowires of trigonal selenium. *Adv. Mater.* **2002**, 12, 219–227.

9   K. C. Nomura, Optical Activity in Tellurium, *Phys. Rev. Lett.* **1960**, 5, 500–501.

10   Z. Tangs, Y. Wang, K. Sun, N. A. Kotov, Spontaneous Transformation of Stabilizer-Depleted Binary Semiconductor Nanoparticles into Selenium and Tellurium Nanowires, *Adv. Mater.* **2005**, 17, 358–363.

11   T. G. Schaaff, G. Knight, M. N. Shafigullin, R. F. Borkman, R. L. Whetten, Isolation and Selected Properties of a 10.4 kDa Gold: Glutathione Cluster Compound, *J. Phys. Chem. B* **1998**, 52, 10643–10646.

12   T. G. Schaaff, R. L. Whetten, Giant Gold−Glutathione Cluster Compounds: Intense Optical Activity in Metal-Based Transitions, *J. Phys. Chem. B* **2000**,104, 2630 –2641.

13   J. T. Petty, J. Zhang, N. V. Hud, R. M. Dickson, DNA-Templated Ag Nanocluster Formation, *J. Am. Chem. Soc.* **2004**, 126, 5207–5212.

14   C. Gautier, T. Bürgi, Chiral *N*-Isobutyryl-cysteine Protected Gold Nanoparticles: Preparation, Size Selection, and Optical Activity in the UV−vis and Infrared, *J. Am. Chem. Soc.* **2006**, 128, 11079–11087.

15   H. Yao, T. Fukui, K. Kimura, Chiroptical Responses of D-/L-Penicillamine-Capped Gold Clusters under Perturbations of Temperature Change and Phase Transfer, *J. Phys. Chem. C* **2007**, 111, 14968–14976.

16   N. Nishida, H. Yao, T. Ueda, A. Sasaki, K. Kimura, Synthesis and Chiroptical Study of D/L-Penicillamine-Capped Silver Nanoclusters, *Chem. Mater.* **2007**, 19, 2831–2841.

17   J. Kumar, T. Kawai, T. Nakashima, Circularly polarized luminescence in chiral silver

nanoclusters, *Chem. Commun*. **2017**, 53, 1269–1272.

18   P. D. Jadzinsky, G. Calero, C. J. Ackerson, D. A. Bushnell, R. D. Kornberg, Structure of a thiol monolayer-protected gold nanoparticle at 1.1 Å resolution. *Science* **2007**, 318, 430−433.

19   S. Knoppe, A. A. Wong, S. Malola, H. Häkkinen, T. Bürgi, T. Verbiest, C. J. Ackerson, Chiral Phase Transfer and Enantioenrichment of Thiolate-Protected Au_{102} Clusters, *J. Am. Chem. Soc.* **2014**, 136, 4129–4132.

20   C. Zheng, T. Li, A. Das, N. L. Rosi, R. Jin, Chiral Structure of Thiolate-Protected 28-Gold-Atom Nanocluster Determined by X-ray Crystallography, *J. Am. Chem. Soc.* **2013**, 135, 10011–10013.

21   S. Knoppe, S. Malola, L. Lehtovaara, T. Bürgi, H. Häkkinen, Electronic Structure and Optical Properties of the Thiolate-Protected $Au_{28}(SMe)_{20}$ Cluster, *J. Phys. Chem.* A **2013**, 117, 10526–10533.

22   H. Qian, W. T. Eckenohoff, Y, Zhu, T. Pintauer, R. Jin, Total Structure Determination of Thiolate-Protected Au_{38} Nanoparticles, *J. Am. Chem. Soc.* **2010**, 132, 8280–8281.

23   I. Dolamic, S. Knoppe, A. Dass, T. Bürgi, First enantioseparation and circular dichroism spectra of Au_{38} clusters protected by achiral ligands, *Nat. Commun*. **2012**, 3, 798.

24   S. Knoppe, I. Dolamic, A. Dass, T. Bürgi, Separation of Enantiomers and CD Spectra of $Au_{40}(SCH_2CH_2Ph)_{24}$: Spectroscopic Evidence for Intrinsic Chirality, *Angew. Chem., Int. Ed.* **2012**, 51, 7589–7591.

25   C. Zeng, R. Jin, Chiral Gold Nanoclusters: Atomic Level Origins of Chirality, *Chem. Asian J.* **2017**, 12, 1839.

26   S. Knoppe, T. Bürgi, Chirality in Thiolate-Protected Gold Clusters, *Acc. Chem. Res.* **2014**, 47, 1318–1326.

27   J. Kumar, K. G. Thomas, L. M. Liz-Marzán, Nanoscale chirality in metal and semiconductor nanoparticles, *Chem. Commun.* **2016**, 52, 12555–12569.

28   M. P. Moloney, Y. K. Gun'ko, J. M. Kelly, Chiral highly luminescent CdS quantum dots, *Chem. Commun.* **2007**, 38, 3900–3902.

29   S. Elliott, M. P. Moloney, Y. K. Gun'ko, Chiral Shells and Achiral Cores in CdS Quantum Dots, *Nano Lett*. **2008**, 8, 2452–2457.

30   T. Nakashima, Y. Kobayashi, T. Kawai, Optical Activity and Chiral Memory of Thiol-Capped CdTe Nanocrystals, *J. Am. Chem. Soc.* **2009**, 131, 10342–10343.

31   S. A. Gallagher, M. P. Moloney, M. Wojdyla, S. J. Quinn, J. M. Kelly, Y. K. Gun'ko, Synthesis and spectroscopic studies of chiral CdSe quantum dots, *J. Mater. Chem.* **2010**, 20, 8350–8355.

32   M. Wojdyla, S. A. Gallagher, M. P. Moloney, Y. K. Gun'ko, J. M. Kelly, L. M. Magno, S. J. Quinn, I. P. Clark, G. M. Greetham, M. Towrie, Picosecond to Millisecond Transient Absorption Spectroscopy of Broad-Band Emitting Chiral CdSe Quantum Dots, *J. Phys. Chem.* C **2012**, 116, 16226–16236.

33   V. A. Gérard, M. Freeley, E. Defrancq, A. V. Fedorov, Y. K. Gun'ko, Optical Properties and In Vitro Biological Studies of Oligonucleotide-Modified Quantum Dots, *J. Nanomater.* 2013, 463951.

34   J. E. Govan, E. Jan, A. Querejeta, N. A. Kotov, Y. K. Gun'ko, Chiral luminescent CdS nano-tetrapods, *Chem. Commun.* **2010**, 46, 6072–6074.

35   F. P. Milton, J. Govan, M. V. Mukhina, Y. K. Gun'ko, The Chiral Nano-World: Chiroptically Active Quantum Nanostructures. *Nanoscale Horiz.* **2016**, 1, 14−26.

36   A. Visheratina, N. A. Kotov, Inorganic Nanostructures with Strong Chiroptical Activity, *CCS Chem.* **2020**, 2, 583–604.

37   U. Tohgha, K. Varga, M. Balaz, Achiral CdSe quantum dots exhibit optical activity in the visible region upon post-synthetic ligand exchange with D- or L-cysteine, *Chem. Commun.* **2013**, 49, 1844–1846.

38   U. Tohgha, K. K. Deol, A. G. Porter, S. G. Bartko, J. K. Choi, B. M. Leonard, K. Varga, J. Kubelka, G. Muller, M. Balaz, Ligand Induced Circular Dichroism and Circularly Polarized Luminescence in CdSe Quantum Dots, *ACS Nano* **2013**, 7, 11094–11102.

39   J. K. Choi, B. E. Hayne, U. Tohgha, L. Pap, K. W. Elliott, B. M. Leonard, S. V. Dzyuba, K. Varga, J. Kubelka, M. Balaz, Chirality Inversion of CdSe and CdS Quantum Dots without Changing the Stereochemistry of the Capping Ligand. *ACS Nano* **2016**, 10, 3809−3815.

40   V. Kuznetsova, Y. Gromova, M. Martinez-Carmona, F. Purcell-Milton, E. Ushakova, S. Cherevkov, V. Maslov, Y. K. Gun'ko, Ligand-induced chirality and optical activity in semiconductor nanocrystals: theory and applications. *Nanophotonics* **2020**, 20200473.

41   A. Ben-Moshe, A. Teitelboim, D. Oron, G. Markovich, Probing the Interaction of Quantum Dots with Chiral Capping Molecules Using Circular Dichroism Spectroscopy, *Nano Lett.* **2016**, 16, 7467−7473.

42   X. Gao, X. Zhang, K. Deng, B. Han, L. Zhao, M. Wu, L. Shi, J. Lv, Z. Tang, Excitonic Circular Dichroism of Chiral Quantum Rods, *J. Am. Chem. Soc.* **2017**, 139, 25, 8734–8739.

43   J. Cheng, J. Hao, H. Liu, J. Li, X. Zhu, X. Liu, K. Wang, T. He, Optically Active CdSe-Dot/CdS-Rod Nanocrystals with Induced Chirality and Circularly Polarized Luminescence. *ACS Nano* **2018**, 12, 5341−5350.

44   J. Hao, Y. Li, J. Miao, R. Liu, J. Li, H. Liu, Q. Wang, H. Liu, M. Delville, T. He, K. Wang, X. Zhu, J. Cheng, Ligand-Induced Chirality in Asymmetric CdSe/CdS Nanostructures: A Close Look at Chiral Tadpoles, *ACS Nano* **2020**, 14, 10346–10358.

45   F. Purcell-Milton, A. K. Visheratine, V. A. Kuznetsova, A. Ryan, A. O. Orlova, Y. K. Gun'ko, Impact of Shell Thickness on Photoluminescence and Optical Activity in Chiral CdSe/CdS Core/Shell Quantum Dots, *ACS Nano* **2017**, 11, 9207–9214.

46   I. V. Martynenko, A. S. Baimuratov, V. A. Osipova, V. A. Kuznetsova, F. Purcell-Milton, I. D.

Rukhlenko, A. V. Fedorov, Y. K. Gun'ko, U. Resch-Genger, A. V. Baranov, Excitation Energy Dependence of the Photoluminescence Quantum Yield of Core/Shell CdSe/CdS Quantum Dots and Correlation with Circular Dichroism, *Chem. Mater.* **2018**, 30, 465−471.

47   K. Varga, S. Tannir, B. E. Hayne, B. M. Leonard, S. V. Dzyuba, J. Kubelka, M. Balaz, CdSe Quantum Dots Functionalized with Chiral, Thiol-Free Carboxylic Acids: Unraveling Structural Requirements for Ligand-Induced Chirality. *ACS Nano* **2017**, 11, 9846−9853.

48   V. A. Kuznetsova, E. Mates-Torres, N. Prochukhan, M. Marcastel, F. Purcell-Milton, J. O'Brien, A. K. Visheratina, M. Martinez-Carmona, Y. Gromova, M. Garcia-Melchor, Y. K. Gun'ko, The Effect of Chiral Ligand Concentration and Binding Mode on Chiroptical Activity of CdSe/CdS Quantum Dots. *ACS Nano* **2019**, 13, 13560−13572.

49   G. Li, X. Fei, H. Liu, J. Gao, J. Nie, Y. Wang, Z. Tian, C. He, J. Wang, C. Ji, D. Oron, G. Yang, Fluorescence and Optical Activity of Chiral CdTe Quantum Dots in Their Interaction with Amino Acids, *ACS Nano* **2020**, 14, 4196–4205.

50   X. Gao, B. Han, X. Yang, Z. Tang, Perspective of Chiral Colloidal Semiconductor Nanocrystals: Opportunity and Challenge. *J. Am. Chem. Soc.* **2019**, 141, 13700−13707.

51   A. Ben-Moshe, A. O. Govolov, G. Markovich, Enantioselective Synthesis of Intrinsically Chiral Mercury Sulfide Nanocrystals. *Angew. Chem., Int. Ed.* **2013**, 52, 1275−1279.

52   J. Kuno, T. Kawai, T. Nakashima, The Effect of Surface Ligands on the Optical Activity of Mercury Sulfide Nanoparticles. *Nanoscale* **2017**, 9, 11590−11595.

53   U. Hananel, A. Ben-Moshe, D. Tal, G. Markovich, Enantiomeric Control of Intrinsically Chiral Nanocrystals. *Adv. Mater.* **2019**, 1905594.

54   A. Ben-Moshe, S. G. Wolf, M. B. Sadan, L. Houben, Z. Fan, A. O. Govorov, G. Markovich Enantioselective control of lattice and shape chirality in inorganic nanostructures using chiral biomolecules, *Nat. Commun.* **2014**, 5, 4302.

55   U. Hananel, A. Ben-Moshe, H. Diamant, G. Markovich, Spontaneous and directed symmetry breaking in the formation of chiral nanocrystals, *PNAS* **2019**, 116, 11159−11164.

56   P. P. Wang, S. J. Yu, A. O. Govorov, M. Ouyang, Cooperative expression of atomic chirality in inorganic nanostructures, *Nat. Commun.* **2017**, 8, 14312.

57   P. P. Wang, S. Yu, M. Ouyang, Assembled Suprastructures of Inorganic Chiral Nanocrystals and Hierarchical Chirality. *J. Am. Chem. Soc.* **2017**,139, 6070−6073.

58   E. Vinegrad, D. Vestler, A. Ben-Moshe, A. R. Barnea, G. Markovich, O. Cheshnovsky, Circular Dichroism of Single Particles. *ACS Photonics* **2018**, 5, 2151−2159.

59   D. Vestler, A. Ben-Moshe, G. Markovich, Enhancement of Circular Dichroism of a Chiral Material by Dielectric Nanospheres. *J. Phys. Chem. C* **2019**,123, 5017−5022.

60   M. V. Mukhina, V. G. Maslov, A. V. Baranov, A. V. Fedorov, A. O. Orlova, F. Purcell-Milton, J. Govan, Y. K. Gun'ko, Intrinsic Chirality of CdSe/ZnS Quantum Dots and Quantum Rods, *Nano*

Lett. **2015**, 15, 2844–2851.

61 B. Pal, S. Ikeda, B. Ohtani, Photoinduced Chemical Reactions on Natural Single Crystals and Synthesized Crystallites of Mercury(II) Sulfide in Aqueous Solution Containing Naturally Occurring Amino Acids, *Inorg. Chem*. **2003**, 42, 1518–1524.

62 H. Shindo, Y. Shirota, K. Niki, T. Kawasaki, K. Suzuki, Y. Araki, A. Matsumoto, K. Soai, Asymmetric Autocatalysis Induced by Cinnabar: Observation of the Enantioselective Adsorption of a 5-Pyrimidyl Alkanol on the Crystal Surface, *Angew. Chem., Int. Ed*. **2013**, 52, 9135–9138.

63 I. Dolamic, B. Varnholt, T. Bürgi, Chirality transfer from gold nanocluster to adsorbate evidenced by vibrational circular dichroism, *Nat. Commun*. **2015**, 6, 7117.

64 J. Cheng, G. L. Saux, J. Gao, T. Buffeteau, Y. Battie, P. Barois, V. Ponsinet, M. Delville, O. Ersen, E. Pouget, R. Oda, GoldHelix: Gold Nanoparticles Forming 3D Helical Superstructures with Controlled Morphology and Strong Chiroptical Property, *ACS Nano* **2017**, 11, 3806–3818.

65 M. Suginome, X. Liu, S. Tsunega, E. Nakajima, S. Abe, T. Nakashima, T. Kawai, R. Jin, Circularly Polarized Luminescence from Inorganic Materials: Encapsulating Guest Lanthanide Oxides in Chiral Silica Hosts, *Chem. Eur. J.* **2018**, 24, 6519−6524.

66 X. Wei, J. Liu, G. -J. Xia, J. Deng, P. Sun, J. J. Chruma, W. Wu, C. Yang, Y. -G. Wang, Z. Huang, Enantioselective photoinduced cyclodimerization of a prochiral anthracene derivative adsorbed on helical metal nanostructures, *Nat. Chem*. **2020**, 12, 551−559

67 P. Liu, W. Chen, Y. Okazaki, Y. Battie, L. Brocard, M. Decossas, E. Pouget, P. Muller-Buschbaum, B. Kauffmann, S. Pathan, T. Sagawa, R. Oda, Optically Active Perovskite $CsPbBr_3$ Nanocrystals Helically Arranged on Inorganic Silica Nanohelices, *Nano Lett.* **2020**, 20, 8453−8460.

Chapter 2
The Effect of Surface Ligands on the Optical Activity of HgS Nanoparticles

2-1. Introduction.

Among all the chiral semiconductor NPs so far reported, cinnabar (α-HgS) NPs have exhibited the highest magnitude of circular dichroism (CD) signals.[1] Cinnabar is known as a chiral mineral, which has been used as a red pigment since antiquity. The surface of bulk cinnabar was used in an enantioselective synthesis as a heterogeneous chiral initiator in asymmetric catalysis.[2,3] Markovich and co-workers succeeded in the enantioselective synthesis of α-HgS NPs through the use of the enantiomeric ligand molecule, penicillamine (Pen).[1] The chiral ligand is considered to play a role in the preferential formation of one-handed cinnabar NPs, controlling the enantiomeric excess (*ee*) of NPs. There has been no report about the modification in the chemical structure of chiral ligands in the synthesis of α-HgS NPs, which can influence the optical activity and/or the NP *ee*. The chiral α-HgS NPs gave dissymmetry factor values in absorption, g_{abs} ($g_{abs} = \Delta\varepsilon/\varepsilon$), of 0.012 at the first band-edge peak position, which is exceptionally larger compared to the g_{abs} values of 10^{-4}–10^{-5} for those of semiconductor NPs such as CdSe, CdTe, and ZnSe with intrinsically achiral crystalline systems.[4–8] Given that this immense optical activity is directly related to the chiral crystal core, the chiroptical property should be preserved even after ligand-exchange to an achiral ligand, exhibiting the more prominent and obvious chiral memory effect than that demonstrated by the chiral CdTe NPs with surface-localized chirality.[4]

In this chapter, I demonstrate the chiral memory effect of α-HgS NPs with a chiral crystal core. The chiral α-HgS NPs are prepared in the presence of four different enantiomeric ligands in water, and the effects of the ligand structure on the CD profiles are examined. The surface ligands of these NPs are then replaced with achiral ligands to investigate the preservation of optical activity. The robustness of the chiral memory in the chiral HgS core is demonstrated by monitoring the time-course of CD amplitude at a high temperature.

2-2. The effect of chemical structure of chiral ligand on chiroptical properties of α-HgS NPs.

Four chiral ligands including (D, L)-Pen, (D, L)-cysteine (Cys), *N*-acetyl-L-cysteine (Ac-L-Cys), and *N*-isobutyryl-L-cysteine (Ib-L-Cys) were tested as a capping ligand of HgS NPs (Scheme 2-1). HgS NPs were prepared in the presence of these chiral ligands, in which the molar ratio between the Hg ion and ligand was set to 1:1. In addition to D- and L-Pen, which have already been reported to passivate α-HgS NPs,[1] the other three chiral ligand systems successfully led to the formation of HgS NPs with a cinnabar phase. After the addition of thioacetamide, the reaction mixture exhibited a dark-brown color corresponding to the formation of the metastable achiral phase (β-HgS) confirmed by the powder X-ray diffraction (XRD) measurement (Figure 2-1a).[9] Transmission electron microscopy

(TEM) observation revealed that the β-HgS NPs have a spherical or polyhedral shape with an average diameter of 3.6 nm (Figure 2-1b, c). The solution color gradually changed from black to orange in a few hours depending on the ligand structure. The gradual change of color indicates the transformation of semimetal metacinnabar NPs into cinnabar NPs with bulk bandgaps of zero and 2.2 eV, respectively.[10] The XRD patterns indicate that all the resulting NPs exhibit the cinnabar phase (Figure 2-2). Figure 2-3 shows typical TEM images of α-HgS NPs capped with the enantiomeric ligands. While the HgS NPs capped with Pen, Ac-L-Cys and Ib-L-Cys possessed similar prolate spherical shapes with relatively large size distributions having approximate lengths and widths of 10−20 nm and 5−8 nm, respectively, the Cys-capped NPs exhibited irregularly shaped morphologies. The shape and size of the NPs with (D, L)-Pen and (D, L)-Cys do not depend on the ligand chirality. The high-angle annular dark-field scanning TEM (HAADF-STEM) images of the Pen-capped NPs reveal that each NP is composed of a single-crystalline structure (Figure 2-3a inset).
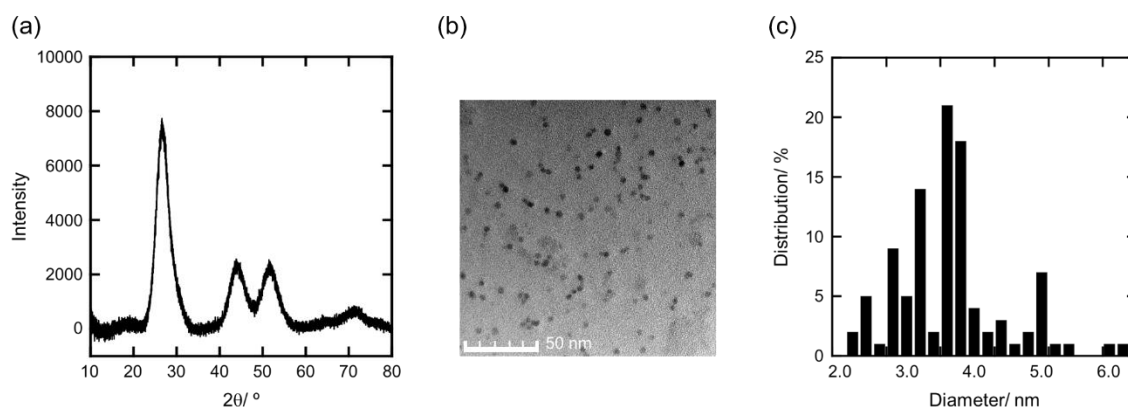

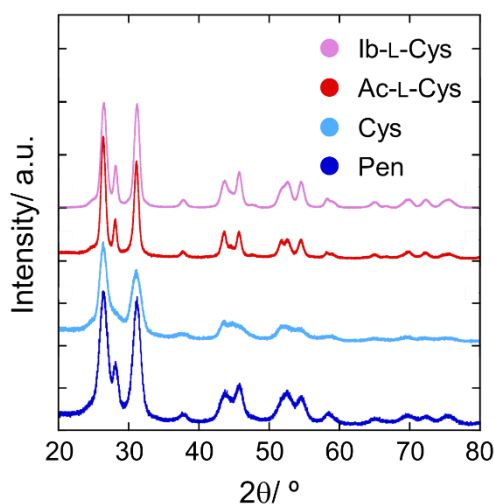**Figure 2-1**. (a) XRD profile, (b) TEM image and (c) size-distribution of β-HgS NPs capped D-Pen.

Figure 2-2. XRD profiles of HgS NPs capped with D-Pen (blue), D-Cys (cyan), Ac-L-Cys (red) and Ib-L-Cys (pink).
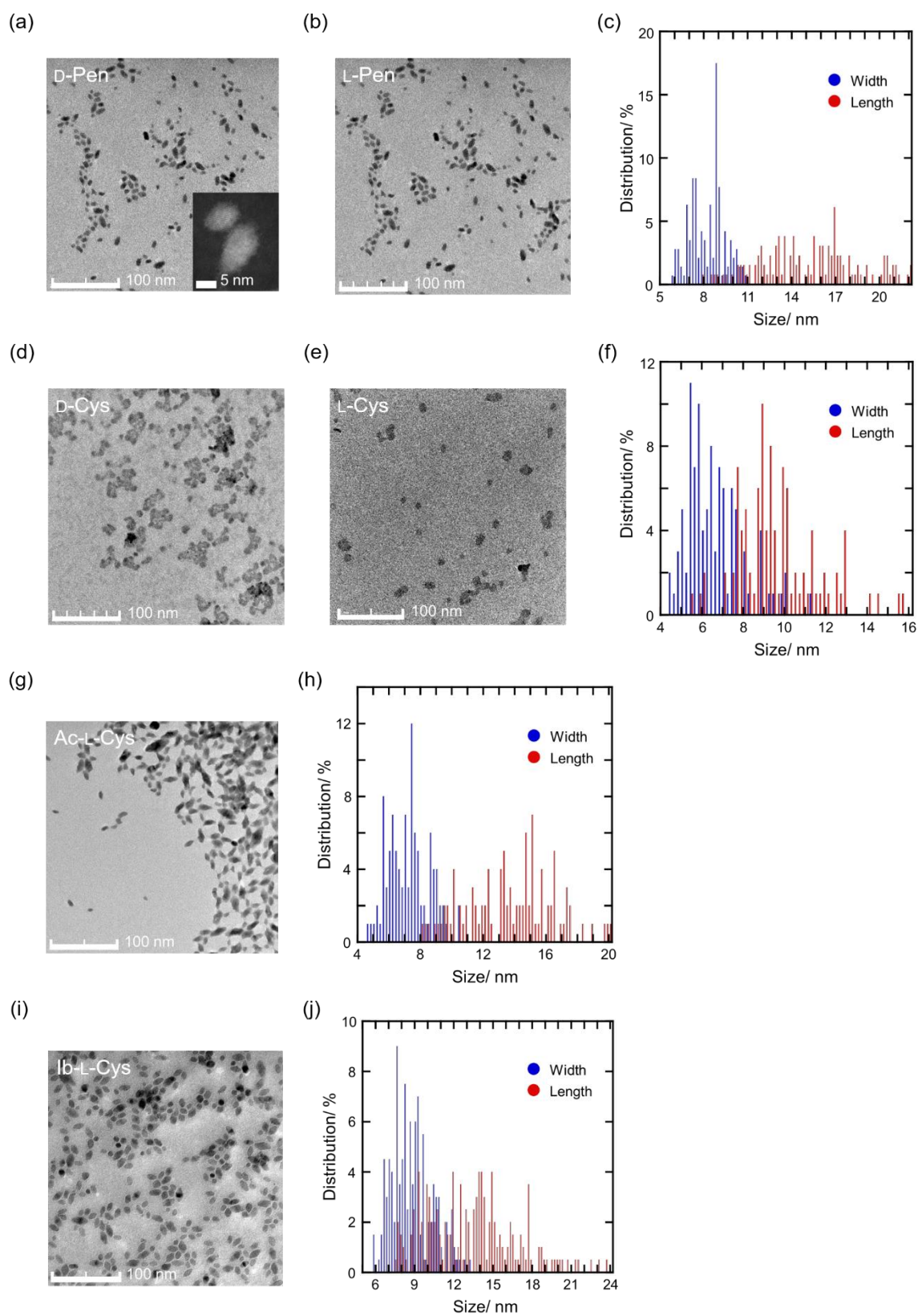
Figure 2-3. TEM images and size distributions of α-HgS NPs capped with chiral ligands: (a, c) D-Pen, (b) L-Pen, (d, f) D-Cys, (e) L-Cys, (g, h) Ac-L-Cys, (i, j) Ib-L-Cys. Inset in (a): Typical HAADF-STEM image of single α-HgS NP.

15

I have performed UV-vis absorption spectra measurements on α-HgS NPs with four ligand systems (Figure 2-4). The NPs prepared in the presence of Pen, Cys, and Ib-L-Cys gave broad UV-vis absorption profiles with an absorption edge around 570 nm, while the NPs capped with Ac-L-Cys exhibited an absorption spectrum with a tail extended to 700 nm, indicating the slight contamination with β-HgS NPs which could not be detected in the XRD spectrum (Figure 2-2). Compared with the bandgap of bulk single crystal (2.2 eV), the absorption edge of NPs gave almost no shift, indicating the negligible quantum confinement effect. A set of enantiomeric ligands exhibited almost identical absorption features of HgS NPs capped with (D, L)-Pen and (D, L)-Cys. The absorption profiles were accompanied by an absorption bump at 480, 525, 480 and 480 nm for α-HgS NPs capped with Pen, Cys, Ac-L-Cys, and Ib-L-Cys, respectively. This difference should be explained by difference in the NPs electronic structures which are modified in response to the chiral ligand structure.

The α-HgS NPs capped with chiral ligands displayed optical activities in the UV to visible range below 600 nm (Figure 2-4). Considering that the ligand does not have effective absorbance above 300 nm, the obtained CD features should stem from the optically active HgS NPs. A set of enantiomeric combination exhibited the mirror-image CD profiles for the Pen- and Cys-capped NPs. The CD spectral profiles differ from each other depending on the chemical structure of chiral ligands. Both L-Pen and L-Cys induced the HgS NPs showing a negative Cotton effect in the range of the exitonic absorption band, suggesting the preferential formation of the α-phase with the same handedness. The difference in the CD spectral shapes between L-Pen- and L-Cys-capped NPs could result from difference in the electronic structures in the HgS core with different morphologies (Figure 2-3). Ouyang and co-workers demonstrated that both the crystallographic and geometric (NP-shape) chirality of HgS NPs have a distinctive effect on the CD spectral shape.[11] The CD activity centering at 540 nm is attributed to the crystallographic chirality, whereas one below 500 nm is mainly determined by interplay between chiral morphology and chiral lattice. The difference between the Pen- and Cys-capped HgS NPs in NP-morphologies might be responsible for the difference in the CD profiles below 500 nm.[11] The α-HgS NPs with Pen- and Cys-ligands gave similar maximum $|g_{abs}|$ values of 0.012 and 0.010, respectively, at around 550 nm. The optical activity should be a result of unequal populations between right- and left-handed α-HgS cores. Since the $|g_{abs}|$ value is proportional to the ee value of the NPs, the similar $|g_{abs}|$ values indicate the similar ee values of Pen- and Cys-capped HgS NPs. The HgS NPs capped by Ib-L-Cys gave a CD signal with a negative first Cotton effect similar to that obtained for L-Pen capped NPs with higher amplitude ($|g_{abs}| = 0.016$). The Ib-L-Cys can induce the formation of a larger enantiomeric ee of α-HgS NPs. This result suggests that chemical structures of chiral ligands give an effect on enantiopurity of the resulting NPs.

Interestingly, the use of Ac-L-Cys reversed the CD response with respect to that of L-Pen-capped HgS NPs despite an identical stereochemistry of these chiral ligands (Figure 2-4). Both ligands gave α-HgS NPs with similar prolate spherical shapes and similar UV-vis absorption profiles, whereas they

exhibit CD spectra in mirror images to each other with varying degrees of amplitude. This result suggests that each ligand led to the preferential formation of an enantiomorphic α-phase with a handedness opposite to each other. The maximum g_{abs} value was estimated to be 0.005 at 550 nm for the Ac-L-Cys capped HgS NPs, which is small considering the chirality of the crystallographic systems. The HgS NPs with Ac-L-Cys are therefore most likely composed of both handed enantiomorphic NPs with a smaller *ee* than that for L-Pen-capped NPs. The inversion of chirality by surface ligands with an identical stereochemistry has already been reported for the CdS and CdSe NPs utilizing the same ligands as in this study (L-Pen and Ac-L-Cys).[12] These ligands are supposed to bind to the semiconductor in a bidentate manner using thiolate and either of carboxylate, amine or acetyl-carbonyl groups.[12−15] Theoretical study has demonstrated that the difference in the preferred bidentate binding modes on the CdSe NPs could give quasi-mirror image CD spectra.[12] The arrangement of chiral ligands on the HgS core surface through bidentate binding modes most likely facilitated the phase transition from the achiral β-phase to chiral α-phase, and the delicate equilibrium between several binding modes should determine the preferred handedness in the chiral α-phase. In this stage, there is no information on the bidentate binding modes of chiral ligands on the HgS surface. However, I could predict that Ac-L-Cys molecules adopt a different binding arrangement compared to L-Pen, L-Cys and Ib-L-Cys, which is discussed in the following chapter.
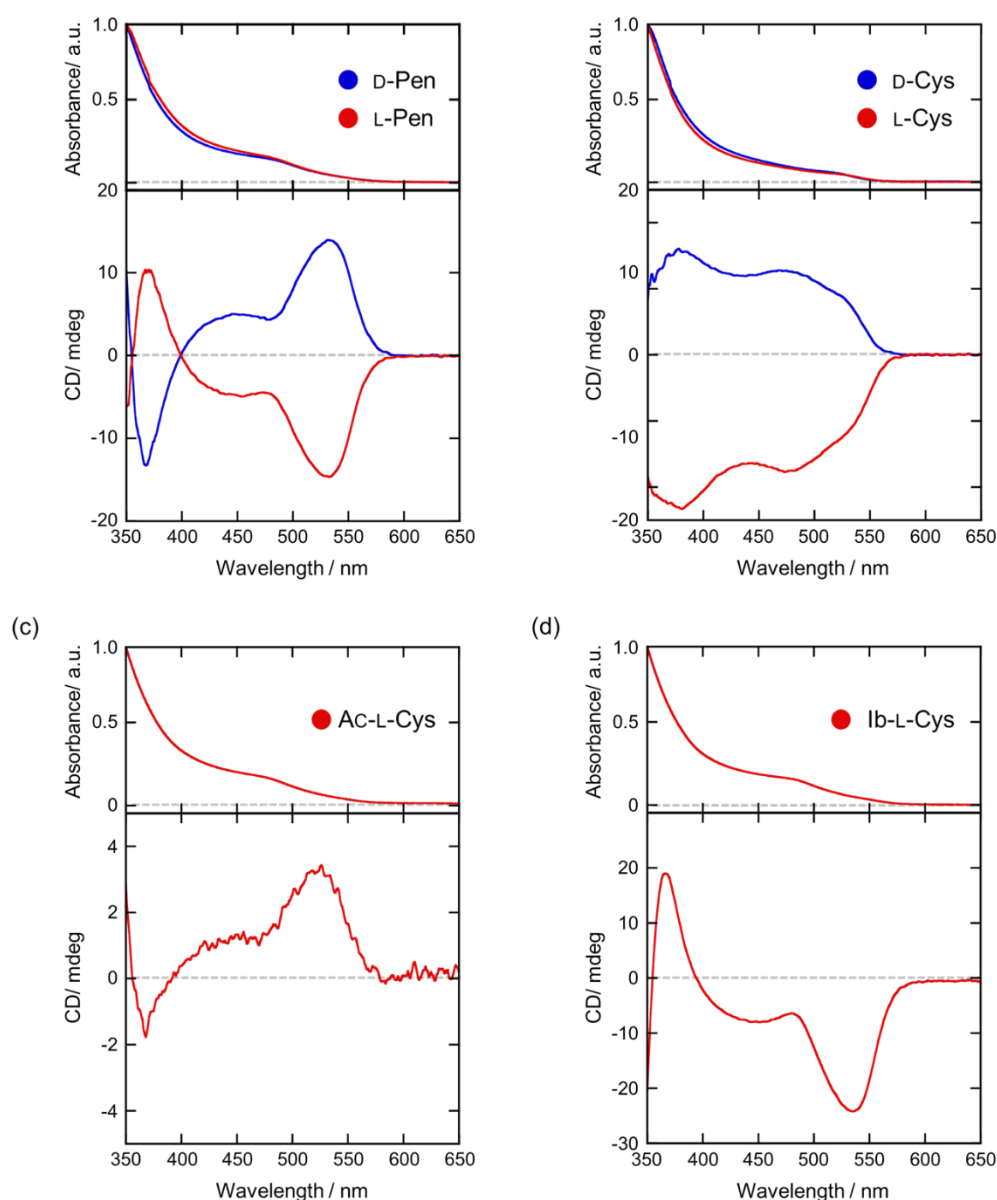
Figure 2-4. Absorption and CD spectra of HgS NPs capped with (a) D- and L-Pen, (b) D- and L-Cys, (c) Ac-L-Cys and (d) Ib-L-Cys.

The use of achiral ligands such as 3-mercaptopropionic acid (MPA) and 2-aminoethanethiol (AET) could not lead to the α-phase but preserved the β-phase with an absorption profile extended over 750 nm (Figure 2-5). Even heating these solutions at 80 ºC could not induce the α-phase but gave irregular aggregates as the participate. These ligands could not attain the bidentate coordination while ensuring water-dispersibility. Several considerations thus led to the conclusion that bidentate binding modes of chiral ligands play an important role in the chirality induction of HgS NPs.
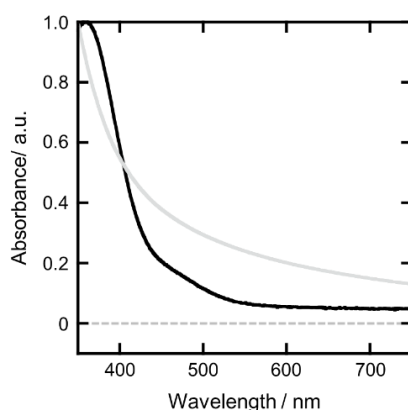
Figure 2-5. Absorption spectra of HgS NPs capped with MPA (grey) and AET (black).

2-3. Chiral memory effect of α-HgS NPs

To explore α-HgS NPs ability to preserve chirality, original hydrophilic chiral ligands of the NPs were displaced by an achiral ligand, 1-dodecanethiol (DT), using an established phase transfer procedure.[4] The solution of DT was added to aqueous solutions of α-HgS NPs capped with (D, L)-Pen and (D, L)-Cys, and then shaken vigorously over 12 hours to allow DT to replace the hydrophilic ligands. The DT-capped HgS NPs were stably soluble in chloroform. I confirmed the ligand exchange with ^{1}H NMR measurement. The DT-capped HgS NP ligand exchanged from D-Cys gave broad signals similar to those observed for DT-capped Au NPs[16] and no signal corresponding to D-Cys[15] was found (Figure 2-6). I have found that α-HgS NPs before and after the ligand-exchange possess the identical UV-vis absorption profiles (Figure 2-7a,d), indicating that the NPs maintained the cinnabar crystalline phase. Figure 2-8 show typical TEM images of the ligand-exchanged HgS NPs. The size of NPs apparently decreased after ligand-exchange. In particular, the average long-axis length decreased from 15.1 to 6.6 nm, resulting in the round shape of the ligand-exchanged NPs. This result indicated that the absorption spectral profiles were almost independent of the NP size and also confirmed that the negligible quantum confinement effect was operative on these HgS NPs. The decrease in the NP size may be due to chemical etching of HgS core with the excess amount of thiol molecule (DT).[17]
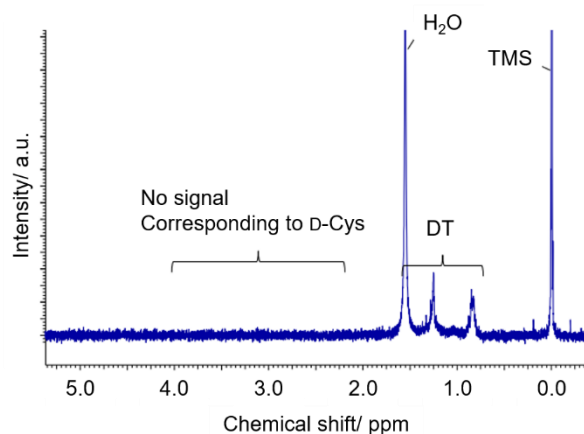
Figure 2-6. ^{1}H-NMR spectrum after the ligand exchange from D-Cys to DT (in CDCl$_3$/TMS)
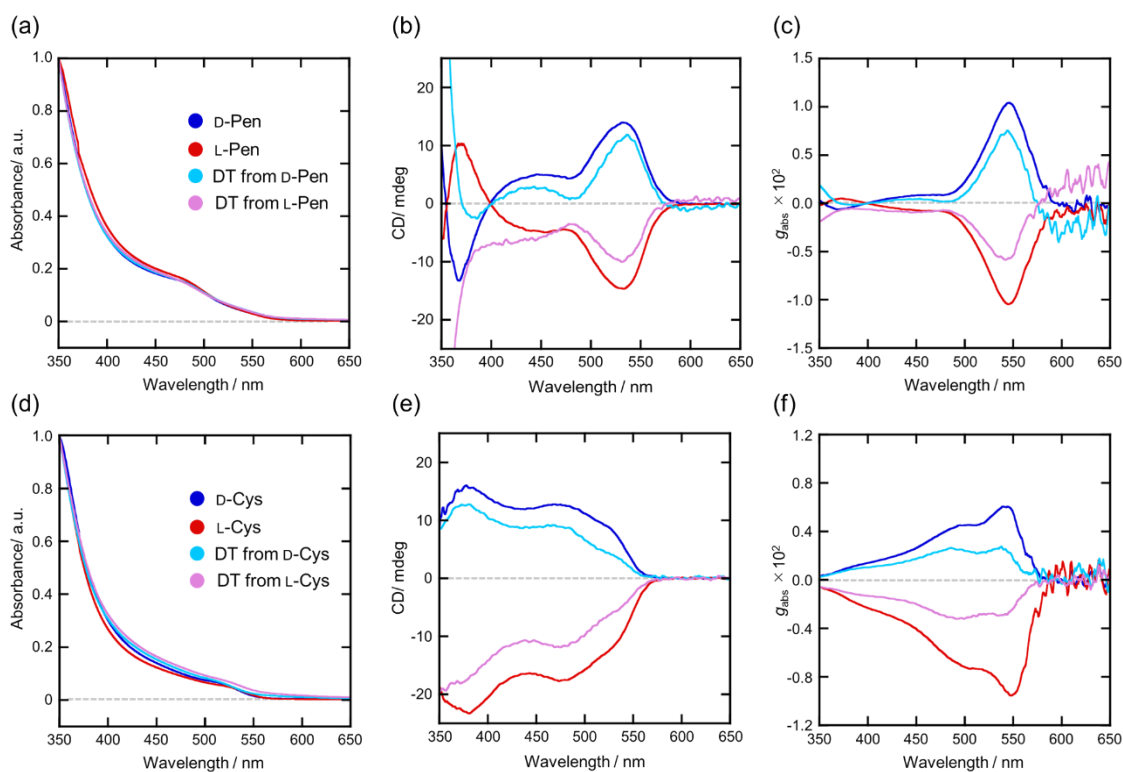

Figure 2-7. UV-vis (a, d), CD (b, e) and g_{abs} (c, f) spectra of HgS NPs before and after ligand exchange from (D, L)-Pen (a, b, c) and (D, L)-Cys (d, e, f), respectively. The NPs before ligand-exchange from D-isomer and L-isomer are represented blue and red, respectively. The NPs after ligand-exchange from D-isomer and L-isomer are represented cyan and purple, respectively.
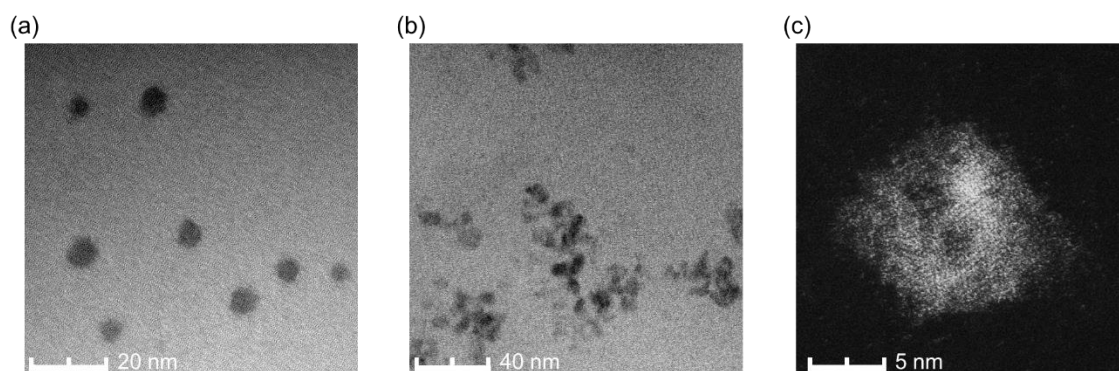
Figure 2-8. (a, b) TEM and (c) STEM images of HgS NPs after ligand exchange from (a, c) Pen and (b) Cys, respectively.

Both NPs ligand exchanged form D- and L-isomers should have the identical ligand composition on the NP surface and possess chiral α-HgS cores covered with achiral DT molecules. The DT-capped HgS NPs preserved the optical activity with an identical sign of Cotton effect at around 550 nm to those of NPs before the ligand-exchange (Figure 2-7b,e), thus demonstrating the preservation of the chiral crystalline system in the NP core. The XRD patterns of the ligand exchanged NPs can be assigned to the chiral cinnabar phase (Figure 2-9). Hence, I concluded that the NPs preserved the chiral cinnabar crystalline structure even with the achiral ligand.
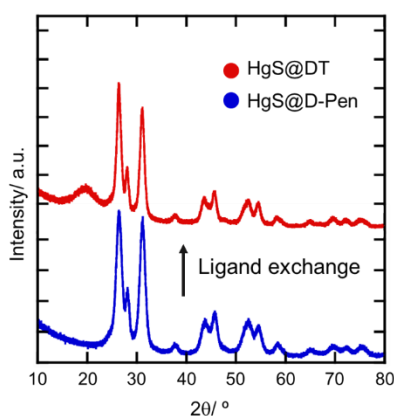

Figure 2-9. XRD profiles of HgS NPs before (blue) and after (red) ligand-exchange from D-Pen.

The shape of CD spectral profiles over 400 nm is mostly preserved for DT-capped NPs ligand-exchanged from (D, L)-Pen, while the those below 400 nm are quite different from each other (Figure 2-7b), suggesting the contribution of chiral geometry and/or the chiral surface states in this CD spectral region.[11] Because the TEM characterization revealed an achiral sphere shape of ligand-exchanged NPs (Figure 2-8a,b), geometrical contribution to optical activity should be negligible. The HAADF-STEM image of a DT-capped HgS NP clearly indicated the less crystallinity and more crystalline defects

compared to that of Pen-capped ones (Figure 2-8c). This result can explain the difference in the CD features below 400 nm after the ligand-exchange. It should be noted that free cysteine derivative ligands displayed CD signals only below 300 nm. The CD signals originated from an interaction between the chiral ligand and semiconductor QDs can be observed over 400 nm, which were several orders of magnitude lower than the CD response of chiral α-HgS NPs.[17] Thus, the difference in the ligand arrangement after the ligand-exchange was almost negligible in the g_{abs} spectra (Figure 2-7c,f).

To gain more quantitative understanding of their chiroptical properties, I evaluated the dissymmetric factor g_{abs} of ligand-exchanged HgS NPs. In Figure 2-7, the $|g_{abs}|$ values of DT-capped HgS NPs were about 0.006 and 0.004 after the ligand exchange from (D, L)-Pen and (D, L)-Cys, respectively. Although the dissymmetry factors decreased from the original values, those values are still high compared to those of chiral ligand-coated semiconductor NPs with intrinsically achiral crystalline. The electronic hybridization between chiral ligands and semiconductor cores can be taken into no account as a reason for the decrease of g_{abs} values because of induced optical activity with the g_{abs} values in the range of 10^{-4} to 10^{-5}.[12,18,19] It is worth noting that the NP size decreased due to ligand exchange accompanied by chemical etching. Some investigations of the size-dependent optical activity of semiconductor NPs with chiral ligands have been previously reported which show that the smaller NPs exhibited the larger g_{abs} values, suggesting surface-dominant chirality.[20] On the other hand, the dissymmetry factor g_{abs} of the intrinsically chiral α-HgS NPs represents the chiroptical response per one α-HgS crystalline unit. Obviously, the g_{abs} value is independent on the NP size.[11] The chemical etching can reduce the NP size and disturb the chiral crystalline atomic arrangement at the HgS core surface, which is observed as the emergence of a broad peak at 20° in the XRD spectrum corresponding to the amorphous phase (Figure 2-9). The HAADF-STEM image showed the amorphous phase along the perimeter of the DT-capped HgS NPs (Figure 2-8c), suggesting less crystallinity compared to the NPs before ligand-exchange. Due to the high surface-to-volume ratio in the NPs, the loss of chiral cinnabar crystalline layer should give rise to the decrease in the magnitude of g_{abs} values. Even the amorphous phase should have distinct absorption properties, contributing to the term of extinction coefficient (ε) but not to the CD activity ($\Delta\varepsilon$) in the g_{abs} value.

To study the influence of the chemical etching on the decrease of the optical activity, I employed oleylamine (OAm) as an achiral ligand molecule. The amine group in OAm has a relatively lower binding constant to a semiconductor core surface compared to thiol group, leading to the suppression of chemical etching even in the presence of an excess of OAm. By ligand exchange from Pen to OAm under the same conditions as above, OAm-capped HgS NPs dispersed solutions were obtained. The XRD measurement indicated the maintained cinnabar phase of the ligand-exchanged HgS NPs and the almost absence of amorphous phase due to the negligible peak around 20° (Figure 2-10a). The TEM images of the OAm-capped NPs demonstrated no obvious change in the size and shape after ligand exchange (Figure 2-10b,c). All these results confirmed that negligible chemical etching

occurred after ligand exchange from (D. L)-Pen to OAm. As shown in Figure 2-11, no meaningful change was observed in absorption and CD spectra after the ligand exchange. The OAm-capped HgS NPs gave the similar $|g_{abs}|$ values (0.016) around 550 nm with those of the original enantiomeric Pen-capped HgS NPs, owing to the absence of the amorphous phase.
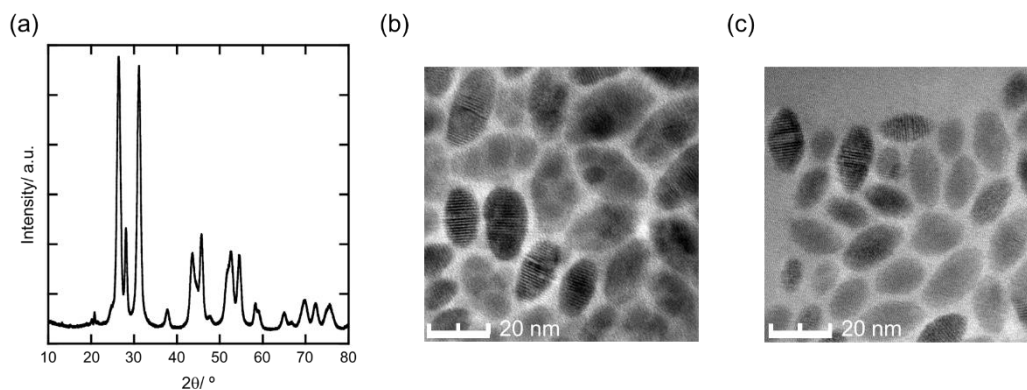

Figure 2-10. (a) XRD profiles of OAm-capped HgS NPs. TEM images of HgS NPs after ligand exchange from (b) D-Pen and (c) L-Pen.
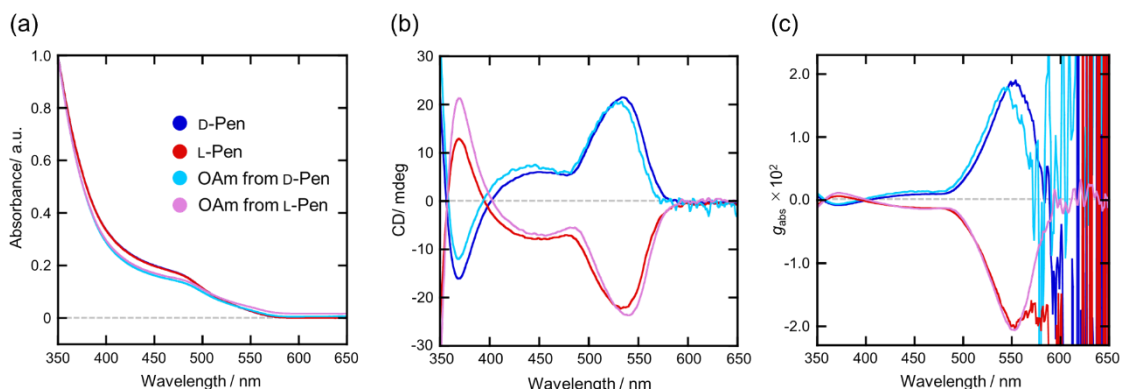

Figure 2-11. (a) UV-vis, (b) CD and (c) g_{abs} spectra of HgS NPs before and after ligand exchange from (D, L)-Pen. The NPs before ligand-exchange from D-isomer and L-isomer are represented blue and red, respectively. The NPs after ligand-exchange from D-isomer and L-isomer are represented cyan and purple, respectively.

To obtain further insight into the robustness of the intrinsically chiral structure of α-HgS NPs, I investigated the thermal stability of the CD intensity for the NPs with chiral L-Cys and achiral DT. The DT-capped HgS NPs were prepared through the ligand-exchange from L-Cys, and then the reaction product was dispersed in 1,1,2,2-tetrachloroethane (TCE). The time course of relative CD amplitude at 540 nm was monitored for the aqueous solution of L-Cys-capped HgS NPs kept at 80 ºC

and the DT-capped HgS NPs in the solution of TCE at 100 ºC (Figure 2-12b). The annealing treatment has no influence on the UV-vis spectral shape of the NPs (Figure 2-12a), indicating the stability of cinnabar phase in the NP cores. The heat treatment led to a gradual decrease of the CD response for L-Cys-capped HgS NPs, while that for DT-capped HgS NPs maintained almost 90% of the initial intensity over 12 h. The finding indicated that the chiral ligand-capped HgS NP undergo a racemization reaction, which involves the inversion of the handedness of the chiral crystalline structures. Surprisingly, the chirality of DT-capped NPs was preserved even in the absence of chiral ligands and at a higher temperature. Considering that achiral ligand-capped Au$_{38}$ nanoclusters with an intrinsic chiral arrangement of a small number of gold atoms showed thermal racemization at moderate temperatures (40−70 ºC),[21-23] the activation energy to the racemization of the HgS NPs should be reasonably high. This result also could exclude the racemization of NPs as a reason for the decrease in the g_{abs} values after the ligand exchange to DT. In this stage of study, I expect that the higher dispersion stability of the DT-capped NPs may be related to the enhancement compared to that for the Cys-capped NPs. Short-chained water-soluble thiols were reported to possess weak passivation capability to nanocrystal cores,[24] resulting in the irreversible formation of precipitates after thermal treatment.
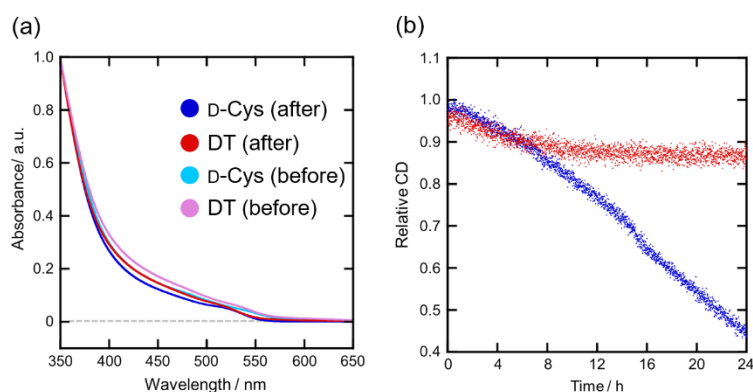

Figure 2-12. (a) Absorption spectral change of HgS NPs capped with L-Cys and DT before and after the heat treatment. (b) Time course of CD intensity at 540 nm for Cys- (blue) and DT-capped HgS NPs (red).

2-4. Conclusions.

Mercury sulfide NPs were prepared in the presence of water-soluble thiols as capping ligands. Chiral thiol ligands, cysteine-based derivatives, successfully afforded the formation of chiral cinnabar phase from the achiral metacinnabar phase, leading to optically active NPs. A slight modification in the chemical structures of chiral ligands with an identical stereochemistry (L-form) resulted in the reversal of chirality in the α-HgS core. This finding suggests that the preferential handedness of chiral

α-HgS core can be determined by ligand binding geometry (coordination mode) on the NP surface. Considering the use of achiral thiols preserved the β-phase of the HgS NPs, I proposed that bidentate binding modes of chiral ligands play an important role in the induction of chirtality in HgS NPs.

I demonstrated that the chiral crystalline structure of the HgS cores was preserved after the ligand-exchange by achiral ligands, DT and OAm. The dissymmetry factor of the DT-capped NPs decreased by almost half, which could be attributed to the amorphous phase formed by the chemical etching. Meanwhile, the ligand exchange performed with OAm successfully suppressed this etching even in the presence of an excess of OAm, resulting in almost complete preservation of optical activity in α-HgS NPs. The chiral crystalline phase was robust enough to be preserved even at high temperature in the absence of the chiral ligand. The chiral memory effect has important implications for future applications of the α-HgS NPs, e.g., for chiral sensing and symmetric catalyst. In Chapter 5, I actually employed chiral α-HgS NPs as a chiral template to generate CPL property of an achiral fluorescent surface ligand.
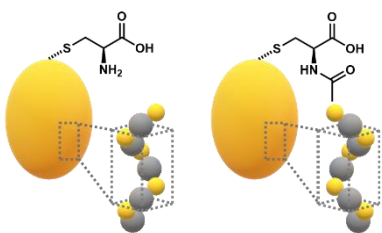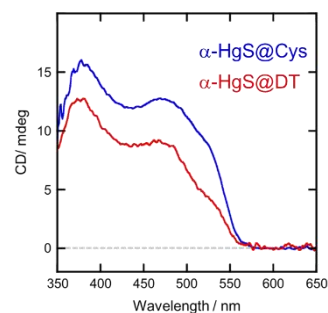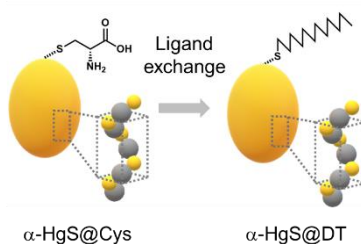
2-5. Experimental; Synthesis of α-HgS NPs and ligand-exchange from chiral ligands to 1-dodecanthiol (DT) and oleylamine (OAm).

HgS NPs were prepared and purified according to the method reported by Markovich and co-workers. An aqueous solution of $Hg(NO_3)_2$ (100 mM, 0.9 mL) was diluted with water (3.0 mL), and then an aqueous solution of a chiral ligand (100 mM, 0.9 mL) was added. The resulting mixture was stirred at room temperature for a few minutes, and its pH value was increased slowly to approximately 11.5 by the dropwise addition of aqueous NaOH (1 M, 0.4 mL). The addition of an aqueous thioacetamide solution (100 mM, 0.9 mL) led to the immediate appearance of a dark brown color corresponding to the formation of HgS NPs with the metastable β-phase. The reaction mixture was stirred in the dark for 24 h at room temperature for the synthesis of Pen-capped HgS NPs. The synthesis of Cys-, Ac-L-Cys- and Ib-L-Cys-capped HgS NPs needed further stirring at 50 ºC for over 3 h. Acetone was then added to precipitate the HgS NPs from the reaction solution. The NPs were collected by centrifugation for 5 min at 5 000 rpm and then redissolved in water. HgS NPs were purified by repetitive dispersion-reprecipitation cycles using water and acetone.

Original hydrophilic chiral ligands of α-HgS NPs were displaced by 1-dodecanethiol (DT) and oleylamine (OAm) using an established phase transfer procedure. An aqueous solution of the NPs (1 mL) was mixed with 1 mL of DT and OAm followed by the addition of 1 mL of acetone. The reaction mixture was stirred vigorously at 50 ºC for over 2 h. The transfer of NPs to the organic phase was easily detected by its color change. After phase transfer, the organic phase was carefully collected and mixed with methanol, followed by centrifugation at 5 000 rpm for 5 min. The NPs were washed two times with methanol after redispersed in a drop of chloroform. As a result, the α-HgS NPs can be dispersed well in chloroform and optical properties were measured.

2-6. Experimental; Characterization.

UV-vis absorption spectra were collected at room temperature using a Jasco V660 specraphotometer. CD spectra were recorded at 25 ºC using Jasco J-725 spectropolarimeter equipped with a single position Peltier temperature control system. Conditions were as follow: scanning speed 200 nm/min, data pitch 1.0 nm and bandwidth 4 nm. A quartz cuvette with a 1 cm path length was used for all UV-vis and CD experiments. Samples for TEM and STEM were prepared by drop-cast of a solution of HgS NPs onto carbon-coated copper grids and dried in vacuum. TEM and HAADF-STEM imaging was performed on a JEOL JEM-2200FS electron microscope and Hitachi HD-2700, respectively. X-ray diffraction data was collected using a Rigaku RINT-TTR III/NM X-ray diffractometer.

2-7. References.

1   A. Ben-Moshe, A. O. Govorov, G. Markovich, Enantioselective Synthesis of Intrinsically Chiral Mercury Sulfide Nanocrystals, *Angew. Chem., Int. Ed*. **2013**, 52, 1275–1279.

2   B. Pal, S. Ikeda, B. Ohtani, Photoinduced Chemical Reactions on Natural Single Crystals and Synthesized Crystallites of Mercury(II) Sulfide in Aqueous Solution Containing Naturally Occurring Amino Acids, *Inorg. Chem*. **2003**, 42, 1518–1524.

3   H. Shindo, Y. Shirota, K. Niki, T. Kawasaki, K. Suzuki, Y. Araki, A. Matsumoto, K. Soai, Asymmetric Autocatalysis Induced by Cinnabar: Observation of the Enantioselective Adsorption of a 5-Pyrimidyl Alkanol on the Crystal Surface, *Angew. Chem., Int. Ed*. **2013**, 52, 9135–9138.

4   T. Nakashima, Y. Kobayashi, T. Kawai, Optical Activity and Chiral Memory of Thiol-Capped CdTe Nanocrystals, *J. Am. Chem. Soc.* **2009**, 131, 10342–10343.

5   S. A. Gallagher, M. P. Moloney, M. Wojdyla, S. J. Quinn, J. M. Kelly, Y. K. Gun'ko, Synthesis and spectroscopic studies of chiral CdSe quantum dots, *J. Mater. Chem*. **2010**, 20, 8350–8355.

6   M. Wojdyla, S. A. Gallagher, M. P. Moloney, Y. K. Gun'ko, J. M. Kelly, L. M. Magno, S. J. Quinn, I. P. Clark, G. M. Greetham, M. Towrie, Picosecond to Millisecond Transient Absorption Spectroscopy of Broad-Band Emitting Chiral CdSe Quantum Dots, *J. Phys. Chem.* C **2012**, 116, 16226–16236.

7   V. A. Gérard, M. Freeley, E. Defrancq, A. V. Fedorov, Y. K. Gun'ko, Optical Properties and In Vitro Biological Studies of Oligonucleotide-Modified Quantum Dots, *J. Nanomater.* 2013, 463951.

8   J. E. Govan, E. Jan, A. Querejeta, N. A. Kotov, Y. K. Gun'ko, Chiral luminescent CdS nano-tetrapods, *Chem. Commun.* **2010**, 46, 6072–6074.

9   R. W. G. Wckoff, Crystal Structures 1, Interscience Publishers: New York, 1963.

10 H. Wang, J. J. Zhu, A sonochemical method for the selective synthesis of alpha-HgS and beta-HgS nanoparticles, *Ultrason. Sonochem.* **2004**, 11, 293–300.

11 P.-P. Wang, S.-J. Yu, A. O. Govorov, M. Ouyang, Cooperative expression of atomic chirality in inorganic nanostructures, *Nat. Commun.* **2017**, 8, 14312.

12 J. K. Choi, B. E. Haynie, U. Tohgha, L. Pap, K. W. Elliott, B. M. Leonard, S. V. Dzyuba, K. Varga, J. Kubelka, M. Balaz, Chirality Inversion of CdSe and CdS Quantum Dots without Changing the Stereochemistry of the Capping Ligand, *ACS Nano* **2016**, 10, 3809–3815.

13 Y. -S. Park, A. Dmytruk, I. Dmitruk, A. Katsuya, M. Takeda, N. Ohuchi, Y. Okamoto, N. Kaji, M. Tokeshi, Y. Baba, Size-Selective Growth and Stabilization of Small CdSe Nanoparticles in Aqueous Solution, *ACS Nano* **2010**, 1, 121–128.

14 S. D. Elliott, M. P. Moloney, Y. K. Gun'ko, Chiral Shells and Achiral Cores in CdS Quantum Dots, *Nano Lett*. **2008**, 8, 2452–2457.

15 V. A. Kuznetsova, E. Mates-Torres, N. Prochukhan, M. Marcastel, F. Purcell-Milton, J. O'Brien,

A. K. Visheratina, M. Martinez-Carmona, Y. Gromova, M. Garcia-Melchor, Y. K. Gun'ko, The Effect of Chiral Ligand Concentration and Binding Mode on Chiroptical Activity of CdSe/CdS Quantum Dots, *ACS Nano* **2019**, 13, 13560–13572.

16 G. Canzi, A. A. Mrse, C. P. Kubiak, Diffusion-Ordered NMR Spectroscopy as a Reliable Alternative to TEM for Determining the Size of Gold Nanoparticles in Organic Solutions, *J. Phys. Chem. C* **2011**,115, 7972–7978.

17 F. Hidalgo, C. Noguez, How to control optical activity in organic–silver hybrid nanoparticles, *Nanoscale* **2016**, 8, 14457–14466.

18 U. Tohgha, K. K. Deol, A. G. Porter, S. G. Bartko, J. K. Choi, B. M. Leonard, K. Varga, J. Kubelka, G. Muller, M. Balaz, Ligand Induced Circular Dichroism and Circularly Polarized Luminescence in CdSe Quantum Dots, *ACS Nano* **2013**, 7, 11094–11102.

19 U. Tohgha, K. Varga, M. Balaz, Achiral CdSe quantum dots exhibit optical activity in the visible region upon post-synthetic ligand exchange with D- or L-cysteine, *Chem. Commun.* **2013**, 49, 1844–1846.

20 A. Ben-Moshe, D. Szwarcman, G. Markovich, Size Dependence of Chiroptical Activity in Colloidal Quantum Dots, *ACS Nano* **2011**, 5, 9034–9043.

21 I. Dolamic, S. Knoppe, A. Dass, T. Bürgi, First enantioseparation and circular dichroism spectra of Au38 clusters protected by achiral ligands, *Nat. Commun.* **2012**, 3, 798.

22 S. Knoppe, I. Dolamic, T. Bürgi, Racemization of a Chiral Nanoparticle Evidences the Flexibility of the Gold−Thiolate Interface, *J. Am. Chem. Soc.* **2012**, 134, 13114–13120.

23 S. Malola, H. Häkkinen, Chiral Inversion of Thiolate-Protected Gold Nanoclusters via Core Reconstruction without Breaking a Au–S Bond, *J. Am. Chem. Soc.* **2019**, 141, 6006–6012.

24 Y. Taniguchi, T. Takishita, T. Kawai, T. Nakashima, End-to-End Self-Assembly of Semiconductor Nanorods in Water by Using an Amphiphilic Surface Design, *Angew. Chem., Int. Ed.* **2016**, 55, 2083–2086.

Chapter 3
Optical Activity Inversion of Chiral Mercury Sulfide Nanoparticles Induced by Chiral Ligand Coordination Alternation

3-1. Introduction.

Chirality is one of the most fascinating characteristics in nature and is also an important research subject in a variety of fields ranging from astronomy to chemical science. Extensive research has been conducted on chirality-related phenomena such as chiral transfer, transcription, amplification, recognition, memory, and inversion in organic molecular systems. Typically, a variety of the systems including helical polymers and supramolecular assemblies[1-3] exhibited the inversion of optical activity without reconstructing covalent bonds. Slight perturbation such as heat, solvents and chemicals can induce the helix inversion in such non-covalently stabilized chiral systems. Chiral inversion was also induced in the gold nanoclusters through ligand exchange with the opposite enantiomer[4] or rearrangement in a surface staple structure.[5,6] Meanwhile, ligand coordination on the NP-surface plays a more decisive role in the chirality induction in the semiconductor NPs systems.[7-11] Even the use of ligands with the same stereochemistry but different chemical structures gives opposite responses in CD spectra, in which enantiomeric binding arrangements on the NP-surface were considered responsible for the reversal of optical activity.[7,9,11] These results motivate me to explore in situ chirality inversion in NPs with an identical ligand system by triggering a change in the coordination structure on the NP-surface. As elucidated in Chapter 2, chiral thiol ligands successfully afforded the formation of the chiral cinnabar phase (α-HgS), leading to optically active NPs. Moreover, a slight modification in the chemical structures of chiral ligands with an identical stereochemistry (L-form) resulted in the reversal of chirality in the α-HgS core. In this Chapter, I describe the observation of optical activity inversion in the synthesis of α-HgS NPs using an identical chiral thiolate ligand. The aqueous solution of HgS NPs synthesized in the presence of N-acetyl-L-cysteine (Ac-L-Cys) gave the first positive Cotton effect, which progressively decreased to eventually become a negative one with heating at 80 ºC. The mechanism of optical activity inversion is discussed through experimental study and calculations.

3-2. Optical activity inversion of chiral HgS NPs with N-acetyl-L-cysteine.

I prepared HgS NPs by a colloidal precipitation method in the presence of Ac-L-Cys according to the procedure as described in Chapter 2-6.[11-13] The addition of thioacetamide to an aqueous solution of mercury ions and Ac-L-Cys molecules was accompanied by the immediate appearance of dark brown color corresponding to achiral β-HgS NPs with a cubic zincblende structure. The solution color gradually changed to orange in 2 hours through heat treatment at 80 ºC. The NPs gave broad UV-vis absorption profiles with an absorbance band at 470 nm (Figure 3-1a), suggesting the transformation

to the thermodynamically favorable α phase. The α-HgS NPs capped with Ac-L-Cys exhibit a CD spectrum showing a positive first Cotton effect (Figure 3-1b). The dissymmetry factor g_{abs} value was estimated to be 1.7×10^{-3} at 550 nm, which is smaller compared to those for Cys- and Pen-capped HgS NPs ($|g_{abs}|=1.0\times10^{-2}$ and 1.2×10^{-2}, respectively).[11,13] In Chapter 2, I concluded that the small g_{abs} value for the HgS NPs with Ac-L-Cys is attributed to the formation of both handed enantiomorphic NPs with a smaller enantiomeric excess (*ee*) than that for L-Pen-capped NPs. As described in Chapter 4, the enantiopure α-HgS NPs afford the $|g_{abs}|$ value as high as 0.021, the $|g_{abs}|$ value of 1.7×10^{-3} for the NPs capped with Ac-L-Cys corresponds to *ee* value of 0.08. The uneven population between the HgS NPs exhibiting positive- and negative-CD signals around 550 nm, hereafter referred to $\alpha^{(+)}$-HgS and $\alpha^{(-)}$-HgS NPs, respectively, is thus responsible for the observed CD activity in the HgS NP system. The extended heating treatment at 80 ºC led to the gradual decrease in the CD intensity followed by the reversal of the CD profile, giving the negative first Cotton effect after 10 h heating (Figure 3-1b). The saturation of the change in absorption and CD spectra appeared after 36 h heating and the minimum g_{abs} value reached to -1.6×10^{-3} (Figure 3-1c), corresponding to the *ee* value of -0.08. The major component NPs before and after the optical activity inversion have opposite chirality in the HgS cores capped with an identical chiral ligand, showing a diastereomeric relationship. The fact is reflected in the non-mirrored CD characteristics of the NPs before and after the CD inversion.[11] Temperature treatment has no significant influence on the UV-vis spectral shape of the NPs, indicating that the NPs maintained the cinnabar crystalline phase (Figure 3-1a). In association with this CD spectral change, an increase in the absorbance was observed, suggesting an increase in the number and/or size of NPs. This increase is accompanied by the inversion of relative population between $\alpha^{(+)}$-HgS and $\alpha^{(-)}$-HgS NPs.
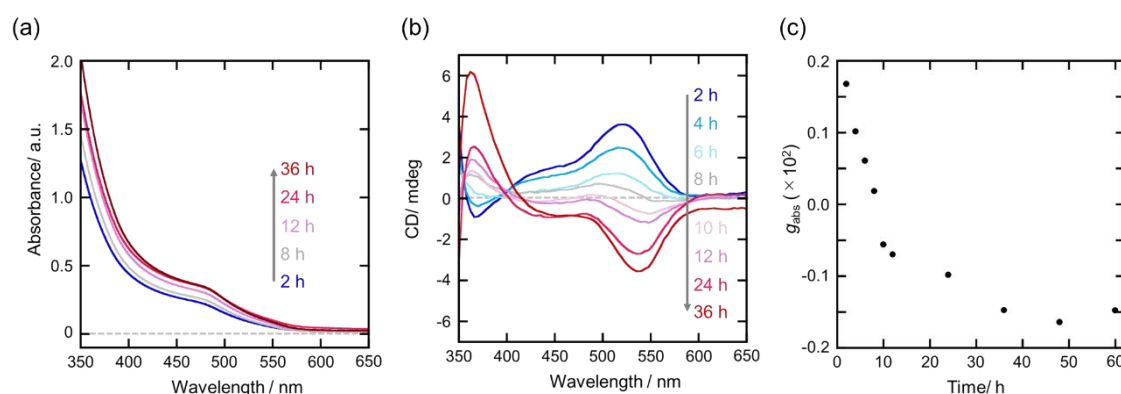

Figure 3-1. Time-dependent (a) UV-vis and (b) CD spectra of HgS NPs upon heating at 80 ºC. (c) Evolution of g_{abs} values at the CD peak position upon heating.

Powder X-ray diffraction (XRD) verified the chiral cinnabar phase of the Ac-L-Cys capped HgS NPs before and after the CD inversion (Figure 3-2). We confirmed the maintenance of the cinnabar phase, which is consistent with the UV-vis spectra in Figure 3-1a. Figure 3-3a,c show typical TEM images of NPs after 2 h and 60 h heating. The both NPs possessed the same prolate spheroidal shape, whereas the average NP size showed a slight increase in the width from 7.2 to 9.5 nm and the length from 13.8 to 18.8 nm. This result also supported the continuous growth of the NPs upon heating at 80 ºC. The size distribution of the NPs changed from 21.5 to 24.2 % after the heating treatment for 60 h (Figure 3-3b, d). The broadening in the size distribution along with the growth of NPs is characteristic of the Ostwald ripening process.[14] The HAADF-STEM images clearly illustrated that the HgS NPs before and after the CD inversion are composed of a single-crystalline structure.
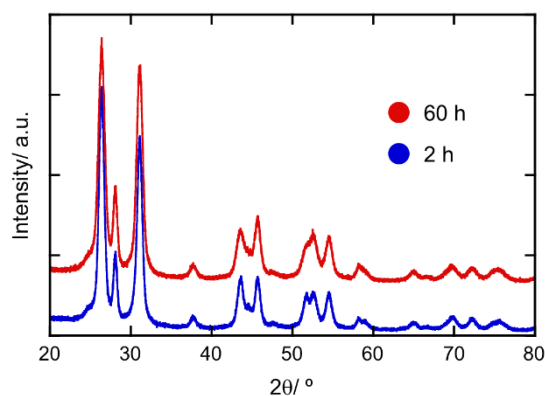

Figure 3-2. XRD profiles of Ac-L-Cys capped HgS NPs before (2 h heating) and after (60 h heating) the CD inversion.
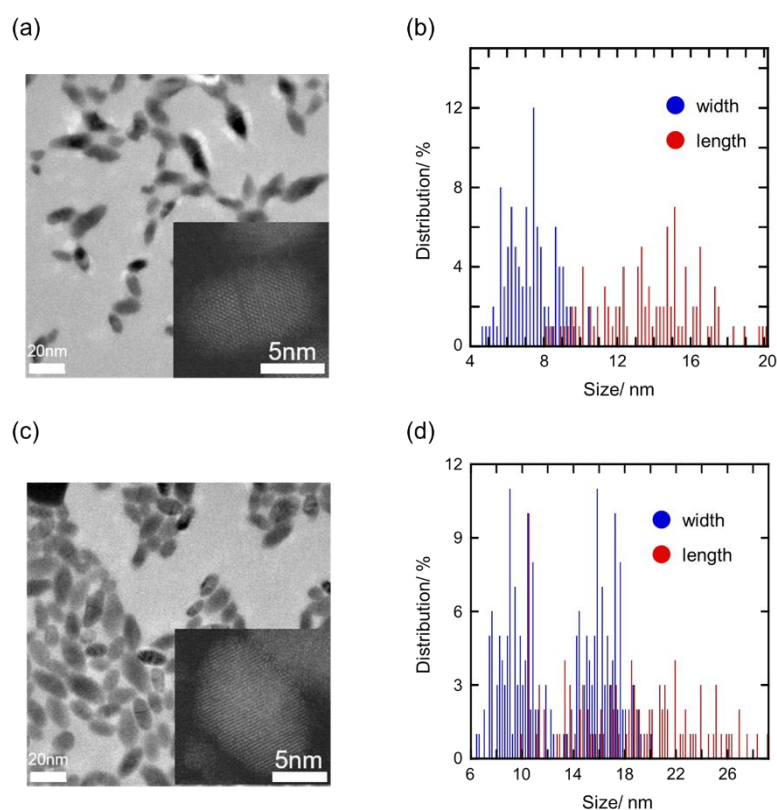
Figure 3-3. (a, c) TEM and STEM (inset) images and (b, d) size distribution of HgS NPs after (a, b) 2 h and (c, d) 60 h heating.

In this chapter, I hypothesize three mechanisms for the inversion of relative population between $\alpha^{(+)}$-HgS and $\alpha^{(-)}$-HgS NPs (Figure 3-4). The first one is that the formation of the $\alpha^{(-)}$-HgS NP is followed by that of the kinetically favored $\alpha^{(+)}$-HgS NP (Figure 3-4(1)). The second mechanism involves the ripening process, in which the $\alpha^{(+)}$-HgS NPs are consumed to dissolve into monomers for the growth and/or formation of $\alpha^{(-)}$-HgS NPs (Figure 3-4(2)). The third one is the inversion of the handedness of the chiral crystalline structure in a single NP (Figure 3-4(3)). To elucidate the underlying mechanism of the optical activity inversion of α-HgS NPs, a few control experiments have been performed. The prepared $\alpha^{(+)}$-HgS NPs were purified to remove the unbonded Ac-L-Cys ligand molecules and unreacted ionic species (Hg^{2+} and S^{2-}). The heating treatment at 80 ℃ on the purified NPs solution could not induce the CD inversion (Figure 3-5a). However, the free Ac-L-Cys molecules were added to the purified solution, and the similar inversion of optical activity was observed (Figure 3-5b). These experiments suggest that the CD inversion is not predominantly attributed to the first mechanism (Figure 3-4(1)). It is known that excess ligand molecules facilitate the ripening reaction of inorganic nanoparticles,[14] and more plausible explanation for the inversion is the second mechanism (Figure 3-4(2)). As mentioned, the broadened size distribution of the NPs after 60 h heating also supported the occurrence of the ripening reaction accompanied by the CD inversion. The different

stability between the $\alpha^{(+)}$- and $\alpha^{(-)}$-HgS NPs can allow the ripening process and be associated with the different mode of surface passivation by the ligand molecules. The third mechanism should involve the change or inversion in the chiral atomic arrangement in a single HgS NP. Unfortunately, there is no direct information on this mechanism and observable intermediate state. Bürgi and co-workers demonstrated the thermal racemization of achiral ligand-capped Au_{38} nanoclusters with an intrinsic chiral arrangement of a small number of gold atoms.[5] Since this racemization corresponded to an intramolecular atomic rearrangement of the nanocluster, no acceleration of the reaction was found in the presence of an excess amount of ligand molecules. However, in the current system, when Ac-L-Cys was added to the purified $\alpha^{(+)}$-HgS NPs solution, the optical activity inversion was observed (Figure 3-5). It is reasonable to assume no or small contribution of the third mechanism to the CD inversion of HgS NPs.
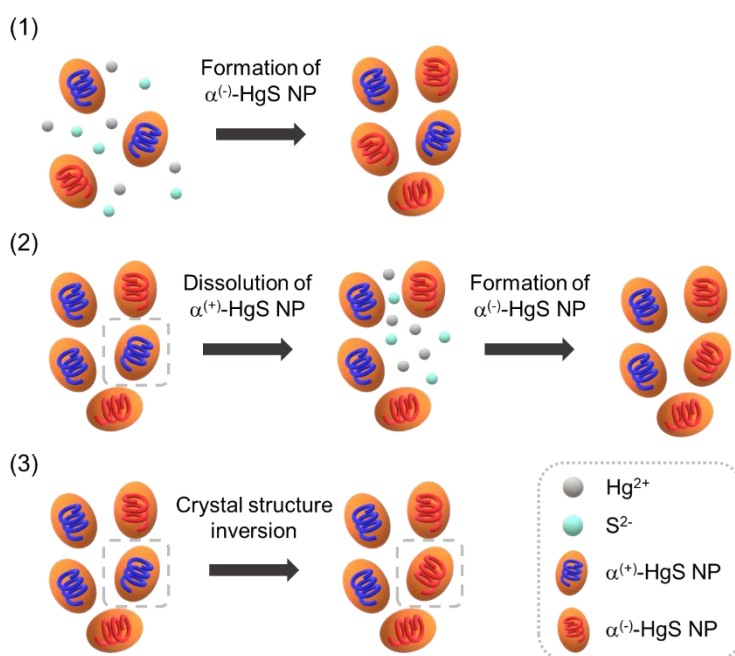

Figure 3-4. Illustration of three possible mechanisms for the inversion of relative population between $\alpha^{(+)}$-HgS and $\alpha^{(-)}$-HgS NPs.
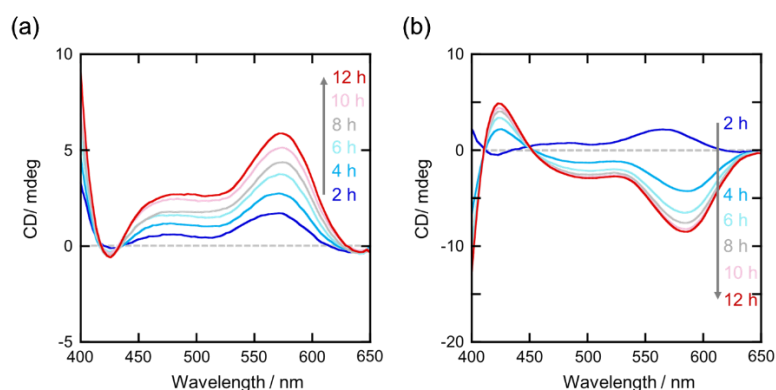
Figure 3-5. CD spectral changes of the purified HgS NPs solution upon heating at 80 °C in (a) the absence of and (b) presence of the free Ac-L-Cys molecules, respectively.

3-3. Investigation of ligand configuration on the HgS NP surface.

One explanation for the different relative stability between $\alpha^{(+)}$- and $\alpha^{(-)}$-HgS NPs might be a difference in the Ac-L-Cys binding mode with Hg^{2+} ions on the NP surface. The Ac-L-Cys ligand at experimental pH over 11.0 has three moieties as thiolate, carboxylate and acetylcarbonyl functional groups. Potentially all of them can be coordinated to Hg^{2+} ions on the NP surface, while thiolate has the strongest affinity to the ions. Thus, Ac-L-Cys can bind to the NP surface via all three groups (tridentate), or via a combination of thiolate and either of carboxylate (S−COO bidentate) or acetylcarbonyl (S−Ac bidentate) groups. The tridentate binding would impair the electrostatic stabilization of the colloidal semiconductor NPs by decreasing the net negative charge on the topmost surface of NPs, potentially causing their aggregation.[7] The presence of neighbor ligand molecules should restrict the number of available surface interaction sites. For these reasons, the possibility of the tridentate binding mode of Ac-L-Cys was ruled out in this study.[15,16] Two possible combinations of bidentate binding modes[7,15,17] are depicted in Figure 3-6. Importantly, the bidentate coordination with S−COO and S−Ac are able to give nearly mirror-imaged coordination configurations on the NP surface. Considering opposite enantiomers of cysteine derivatives, which should show coordination configuration with mirror image relationship, preferentially induce α-phase with opposite chirality, as elucidated in Chapter 2, these S−COO and S−Ac bidentate coordination structures could be assumed to stabilize opposite-handed α-HgS NPs to each other. I hypothesized that the conversion between the preferential coordination configurations would take place during the CD inversion.
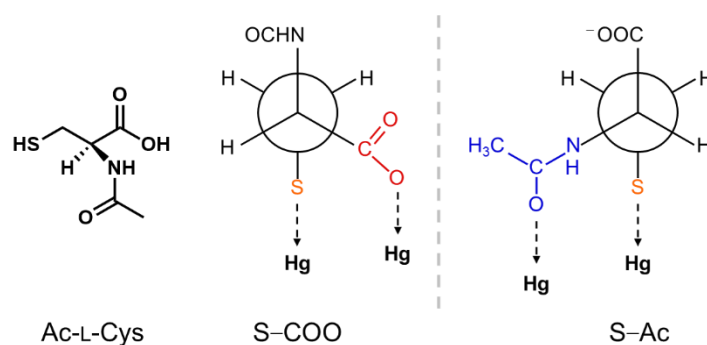
Figure 3-6. (left) Chemical structure of Ac-L-Cys and (right) possible bidentate coordination of Ac-L-Cys on the HgS NP surface.

To discuss the role of coordination structure, I also employed *N*-isobutyryl-L-cysteine (Ib-L-Cys) as a surface ligand molecule. The bulky isopropyl group in Ib-L-Cys should hamper the coordination of the amide-carbonyl group to the surface of NPs, which was confirmed by following simulations. I performed molecular mechanical (MM) simulations on an Ib-L-Cys molecule adsorbed on the (001) surface of α-HgS via S−Ac and S−COO bidentate coordinations. The former coordination gave a contact of the isobutyryl group with surface Hg atoms (Figure 3-7a), while the latter coordination afforded to minimize the steric hindrance between Ib-L-Cys and the HgS surface (Figure 3-7b). Thus Ib-L-Cys was considered to bind selectively in the S−COO bidentate coordination. The HgS NPs capped by Ib-L-Cys gave a CD signal with a negative first Cotton effect similar to that of Ac-L-Cys capped NPs after 36 h heating with a higher amplitude (shown in Chapter 2, $g_{abs} = −0.016$). This result suggests that the bidentate S−COO coordination of L-enantiomer is responsible for the stabilization of $α^{(−)}$-HgS NPs.
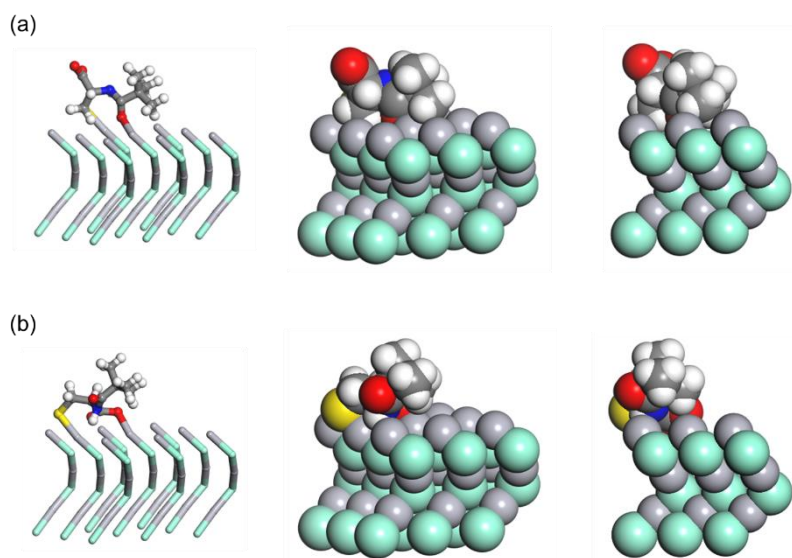

Figure 3-7. Calculated model of Ib-L-Cys binding to (001) surface of α-HgS via bidentate (a) S-Ac and (b) S-COO coordination. Middle: CPK model; Right: side view of the CPK model.

I performed Fourier transform infrared (FTIR) studies to investigate coordination structures of Ac-L-Cys on the HgS NP surface. FTIR measurements were carried out at all stages of the CD inversion. To prepare the samples for the FTIR measurements, the excess ligand molecules were removed by washing of the NPs aqueous solution with acetone/deionized water several times. In this chapter, I focus on the peak patterns around 1600 cm^{-1} associated with amide carbonyl stretching vibration (ν(C=O), amide I) and carboxylate asymmetric one (ν_{as}(COO$^-$)) at the higher and the lower wavenumber, respectively (the full FTIR spectra in Figure 3-8b, d).[18,19] The IR spectrum of HgS NPs capped with Ib-L-Cys can be a good reference to demonstrate the patterns on the bidentate S−COO coordination. The free ligand has shown the ν(C=O) at 1618 cm^{-1} and the ν_{as}(COO$^-$) at 1584 cm^{-1} (Figure 3-8a). A reversal of relative absorbance of these peaks was observed in the spectra of Ib-L-Cys-capped β- and α-HgS NPs. The peak intensity of ν_{as}(COO$^-$) decreased relative to that of ν(C=O) upon the formation of HgS NPs capped with Ib-L-Cys via the S−COO coordination. As shown in Figure 3-8c, free Ac-L-Cys has a similar peak pattern to that of free Ib-L-Cys corresponding to the identical molecular framework except for alkyl group. The IR spectrum of Ac-L-Cys-capped β-HgS NPs was dissimilar to that for Ib-L-Cys-capped β-HgS NPs, indicating the difference in the coordination structures. Heating treatment for 2 h caused the β-to-α phase transformation, resulting in the formation of $\alpha^{(+)}$-HgS NPs. This gave rise to the negligible change in the peak pattern for Ac-L-Cys-capped NPs. The IR spectrum of $\alpha^{(-)}$-HgS NPs, which was after the CD inversion, displayed a reversal of relative peak intensity between ν(C=O) and ν_{as}(COO$^-$), leading to the similar peak pattern to that of Ib-L-Cys-capped NPs. This result suggested the preferential bidentate S−COO coordination of Ac-L-Cys capping structure on the $\alpha^{(-)}$-HgS NP surface. Taking into the difference in the peak pattern before and after the CD inversion into account, it seems plausible that the predominant coordination structure is the bidentate S−Ac coordination for Ac-L-Cys adsorbed on β- and $\alpha^{(+)}$-HgS NPs. Thus, the IR study clearly demonstrates the change in the preferential coordination of Ac-L-Cys on the surface of the NPs.
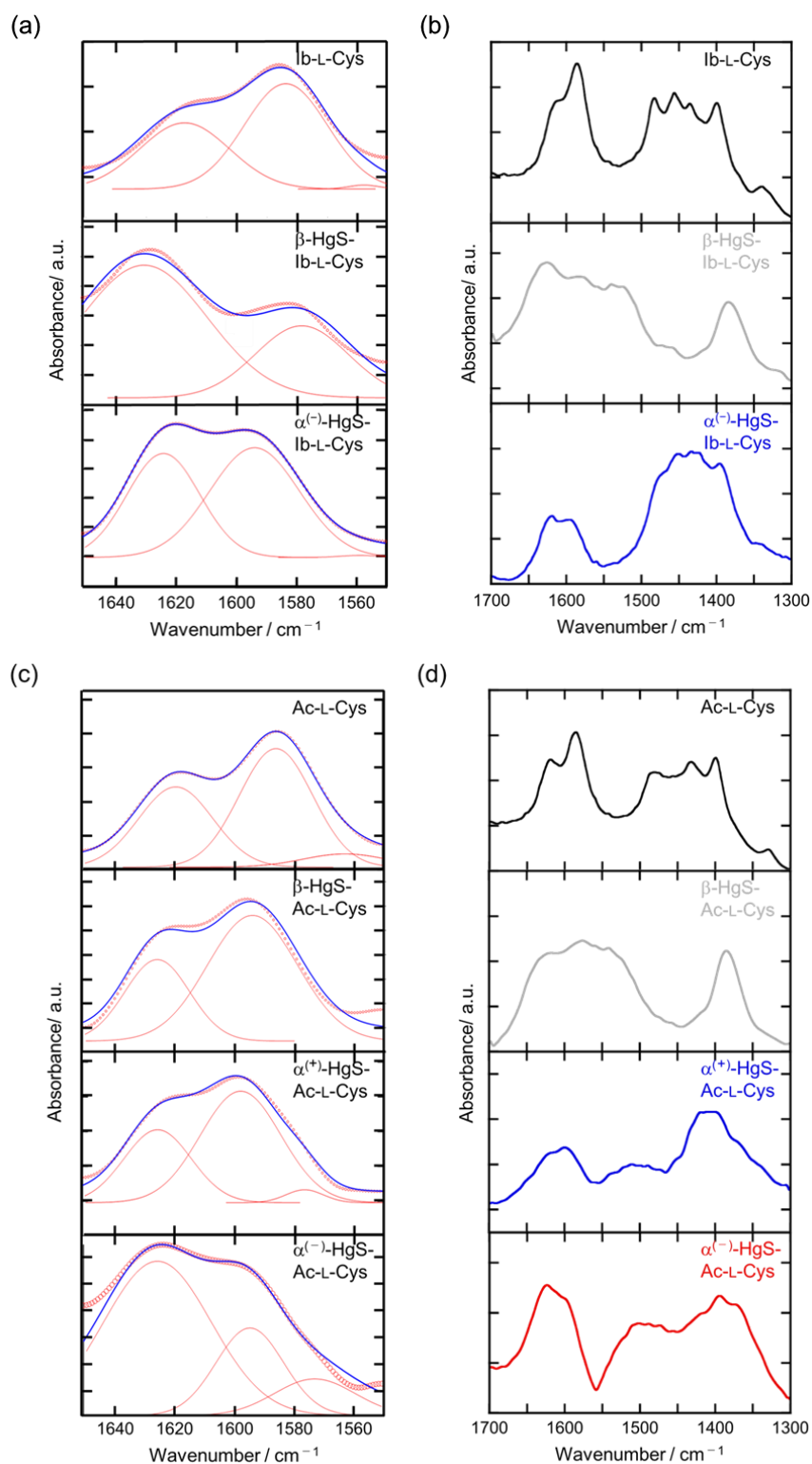
Figure 3-8. FTIR spectra of Ib-L-Cys and Ib-L-Cys-capped HgS NPs (a, b), and Ac-L-Cys and Ac-L-Cys-capped HgS NPs (c, d). In (a, c), blue line: experimental data, red circle: fitted line, red line: devised peak.

First-principle calculations furthermore support the discussion on the chirality inversion behavior observed for the synthesis of Ac-L-Cys-capped HgS NPs. For the calculation, the bidentate coordination structures were constructed on the surface of α-HgS with both handedness. Infinite (001) surface of both enantiomeric α-HgS crystals ($P3_121$ and $P3_221$) were employed to compare the relative stability between possible coordination structures. Four combinations of coordination configurations and enantiomeric α-phases are possible as shown in Figure 3-9. First-principle calculations estimated the relative energy differences with respect to these four patterns. The structural optimization clearly suggested that the S−COO coordination on the α-HgS with the left- and right-handed atomic arrangement (S−COO-α_{left} and S−COO-α_{right}) are more stable than the S−Ac coordination structures by more than 40 kcal mol^{-1}. This result is attributed to the fact that the distance of COO$^-$ and Hg is about 2.15 Å, which is shorter than that of Ac and Hg (ca. 2.24 Å). Therefore, the COO$^-$ group seems to form a strong binding to Hg due to its negative charge. From the above calculation together with the FTIR study, the following explanations are conceivable. The β-HgS NPs with the S−Ac coordination (S−Ac-β NPs) are preferentially formed at the initial stage of synthesis as suggested by the FTIR study. The S−Ac-β NPs are then transformed into S−Ac-α_{left} NPs, which is more stable than S−Ac-α_{right} NPs and should be a kinetically favored process. The S−COO-α_{right} combination is then considered more stable than S−COO-α_{left} by 12.2 kcal mol^{-1}. The energy difference associated with the difference in the coordination structure should drive the shift in the relative populations between the α_{left} and α_{right} NPs with the aid of the ripening process at 80 ℃. The kinetics of the thermal chirality inversion is not simply expressed by the first order one. The evolution of g_{abs} value along with heating time (Figure 3-1c) cannot be simply fitted by a simple monoexponential function. I do not exclude the contributions of multiple reaction pathways involving unexplored intermediate states such as those associated with any other (001) surfaces. In this stage of study, however, the change in the coordination structure in combination with the $\beta-\alpha$ and $\alpha_{\text{left}}-\alpha_{\text{right}}$ phase transformations are possible to explain the chiral inversion behavior, and the participation of two different S−Ac and S−COO coordination configurations most likely plays a key role in this inversion.
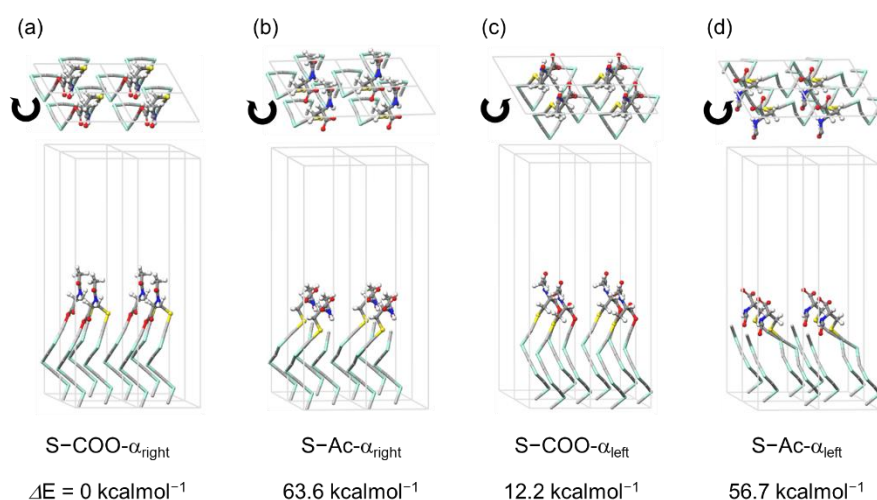
Figure 3-9. Optimized model structures and their relative energies of (a)S−COO-α_{right} HgS, (b) S−Ac-α_{right} HgS, (c) S−COO-α_{left} HgS, and (d) S−Ac-α_{left} HgS. Top: top views; bottom: side views. Four basic unit cells are shown.

3-4. Conclusions.

In this Chapter, I demonstrated the inversion of optical activity in the synthesis of HgS NPs with an identical capping ligand. The HgS NPs with Ac-L-Cys underwent a continuous decrease in CD intensity followed by a reversal in CD pattern upon heating at 80 ºC. The modulation in the bidentate ligand coordination configurations of Ac-L-Cys with thiolate and either carboxylate or acetylcarbonyl groups is most likely responsible for this CD inversion, consistent with the FTIR study. The relative stability with respect to the coordination configurations on the enantiomeric HgS surface was proposed with the aid of first-principles calculations, leading a shift in the distributions of NPs formation to change the relative population of NPs with opposite handedness through the ripening processes. The present chiral inversion system casts an important insight for the understanding in the roles of chiral ligands in chirality induction in NPs. I further expect a future expansion of the present study with a ligand system capable of switching coordination modes in response to external stimuli such as light.
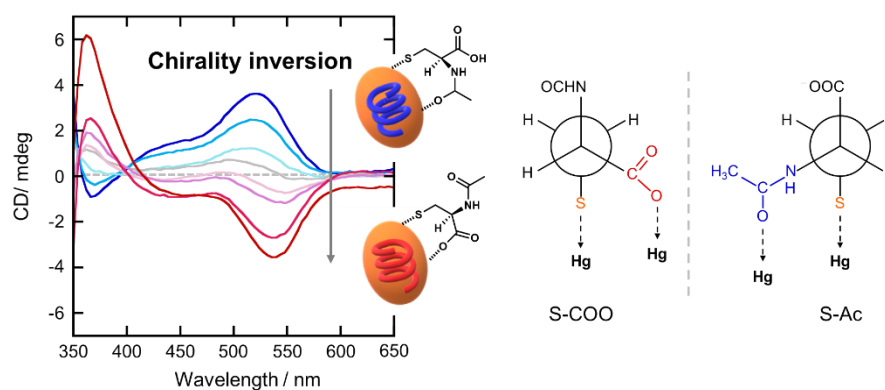
3-5. Experimental; Synthesis and characterization.

The α-HgS NPs were synthesized according to the procedure as noted in section 2-6, using Hg(NO$_3$)$_2$, thioacetamide, and Ac-L-Cys in deionized water. The heat treatment of aqueous solution HgS NPs was performed in the synthetic conditions without purification.

UV-vis spectra were measured at room temperature on a Jasco V670 spectrophotometer. CD spectra were recorded with a Jasco J-725 spectropolarimeter. TEM and HAADF-STEM imaging was performed on a JEOL JEM-2200FS electron microscope and a Hitachi HD-2700, respectively. Samples for TEM and STEM were prepared by drop-cast of a solution of HgS NPs onto carbon-coated copper grids and dried in vacuum. X-ray diffraction data was collected using a Rigaku RINT-TTR III/NM X-ray diffractometer. FTIR spectra were recorded on a Jasco FT/IR-4000. HgS NPs were purified by repetitive dispersion-reprecipitaion cycles using deionized water and acetone, respectively, prior to the FTIR measurement. All solutions of HgS NPs were prepared in D$_2$O. All spectra were recorded at room temperature with a resolution of 4 cm^{-1} in a cell equipped with CeF$_2$ windows with a 0.15 nm-thick Teflon spacer. Peak positions were determined by the negative peak positions in the secondary differentiation spectrum after smoothing processes with the Savitzky-Golay method. Deconvolution and fitting of IR spectra between 1650 and 1550 cm^{-1} using Lorentz functions.

3-6. Experimental; Simulation method.

Herein, I supposed HgS NPs to be large enough to be modeled as a surface and constructed (001) surface of α-HgS including seven atomic layers. The lattice parameters of a, b, and c were fixed at 4.15 and 8.29, which were based on the X-ray crystal structure data of bulk cinnabar. Initial geometries, where the Ac-L-Cys molecule was located inside the basic unit cell of the HgS surface, were first established by molecular force field of Universal and then were optimized by density functional theory calculation at the PBE level using the Vienna an initio simulation package (VASP) code. The PAW was employed for Hg, S, C, N, O and H atoms.

3-7. Reference.

1   E. Yashima, K. Maeda, H. Iida, Y. Furusho, K. Nagai, Helical Polymers: Synthesis, Structures, and Functions, *Chem. Rev.* **2009**, 109, 6102–6211.

2   L. Yang, X. Tam, Z. Wang, X. Zhang, Supramolecular Polymers: Historical Development, Preparation, Characterization, and Functions, *Chem. Rev.* **2015**, 115, 7196–7239.

3   M. Liu, L. Zhang, T. Wang, Supramolecular Chirality in Self-Assembled Systems, *Chem. Rev.* **2015**, 115, 7304–7394.

4   C. Gautier, T. Bürgi, Chiral Inversion of Gold Nanoparticles, *J. Am. Chem. Soc.* **2008**, 130, 7077–7084.

5   S. Knoppe, R. Azoulay, A. Dass, T. Bürgi, Racemization of a Chiral Nanoparticle Evidences the Flexibility of the Gold−Thiolate Interface, *J. Am. Chem. Soc.* **2012**, 134, 20302–20305.

6   Y. Wang, B. Nieto-Ortega, T. Bürgi, Amplification of enantiomeric excess by dynamic inversion of enantiomers in deracemization of Au_{38} clusters, *Nat. Commun.* **2020**, 11, 4562.

7   J. K. Choi, B. E. Haynie, U. Tohgha, L. Pap, K. W. Elliott, B. M. Leonard, S. V. Dzyuba, K. Varga, J. Kubelka, M. Balaz, Chirality Inversion of CdSe and CdS Quantum Dots without Changing the Stereochemistry of the Capping Ligand, *ACS Nano* **2016**, 10, 3809–3815.

8   K. Varga, S. Tannir, B. E. Haynie, B. M. Leonard, S. V. Dzyuba, J. Kubelka, M. Balaz, CdSe Quantum Dots Functionalized with Chiral, Thiol-Free Carboxylic Acids: Unraveling Structural Requirements for Ligand Induced Chirality, *ACS Nano* **2017**, 11, 9846–9853.

9   V. A. Kuznetsova, E. Mates-Torres, N. Prochukhan, M. Marcastel, F. Purcell-Milton, J. O'Brien, A. K. Visheratina, M. Martinez-Carmona, Y. Gromova, M. Garcia-Melchor, Y. K. Gun'ko, The Effect of Chiral Ligand Concentration and Binding Mode on Chiroptical Activity of CdSe/CdS Quantum Dots, *ACS Nano* **2019**, 13, 13560–13572.

10   U. Tohgha, K. K. Deol, A. G. Porter, S. G. Bartko, J. K. Choi, B. M. Leonard, K. Varga, J. Kubelka, G. Muller, M. Balaz, Ligand Induced Circular Dichroism and Circularly Polarized Luminescence in CdSe Quantum Dots, *ACS Nano* **2013**, 7, 11094–11102.

11   J. Kuno, T. Kawai, T. Nakashima, The effect of surface ligands on the optical activity of mercury sulfide nanoparticles, *Nanoscale* **2017**, 9, 11590–11595.

12   A. Ben-Moshe, A. O. Govorov, G. Markovich, Enantioselective Synthesis of Intrinsically Chiral Mercury Sulfide Nanocrystals, *Angew. Chem., Int. Ed.* **2013**, 52, 1275–1279.

13   P.-P. Wang, S.-J. Yu, A. O. Govorov, M. Ouyang, Cooperative expression of atomic chirality in inorganic nanostructures, *Nat. Commun.* **2017**, 8, 14312.

14   F. Wang, V. N. Richards, S. P. Shields, W. E. Buhro, Kinetics and Mechanisms of Aggregative Nanocrystal Growth, *Chem. Mater.* **2014**, 26, 1, 5–21.

15   Y. S. Park, A. Dmytruk, I. Dmitruk, A. Kasuya, M. Takada, N. Ohuchi, Y. Okamoto, N. Kaji, M. Tokeshi, Y. Baba, Size-Selective Growth and Stabilization of Small CdSe Nanoparticles in

Aqueous Solution, *ACS Nano* **2010**, 4, 121–128.

16   T. Delgado-Pérez, L. M. Bouchet, M. D. L. Gaurdia, R. E. Galian, J. Pérez-Pierto, Sensing Chiral Drugs by Using CdSe/ZnS Nanoparticles Capped with N-Acetyl-L-Cysteine Methyl Ester, *Chem. Eur. J.* **2013**, 19, 11068–11076.

17   S. D. Elliott, M. P. Moloney, Y. K. Gun'ko, Chiral Shells and Achiral Cores in CdS Quantum Dots, *Nano Lett.* **2008**, 8, 2452–2457.

18   C. Gautier, T. Bürgi, Vibrational circular dichroism of *N*-acetyl-L-cysteine protected gold nanoparticles, *Chem. Commun.* **2005**, 43, 5393–5395.

19   C. Gautier, T. Bürgi, Chiral *N*-Isobutyryl-cysteine Protected Gold Nanoparticles: Preparation, Size Selection, and Optical Activity in the UV−vis and Infrared, *J. Am. Chem. Soc.* **2006**, 128, 11079–11087.

Chapter 4

Amplification of Enantiomeric Excess by Ostwald Ripening Growth in the Synthesis of Mercury Sulfide Nanoparticles

4-1. Introduction

Surface ligands on colloidal nanoparticles (NPs) play multiple roles in NP chemistry including surface passivation, solubility control, and surface functionalization through the formation of self-assembled monolayers (SAMs) on them. Furthermore, the ligands regulate the growth of inorganic cores through continuous interactions with the topmost surface atoms, controlling the growth rate, size, shape, and crystal structure of NPs.[1-3] As a representative example, the controlled synthesis of cadmium chalcogenide NPs with different crystalline forms of zincblende and wurtzite was achieved through varying the type of ligand and controlling reaction temperatures.[4-7] The surface ligand is generally considered to interact with the crystalline surface of the core through its polar groups.[8-10] More specifically, the use of chiral ligands could form chiral SAMs on the surface of NPs, inducing a chiral distortion, defect, and atomic arrangement on the surface of the core. Surface-based chirality serves as one of the origins of optical activity in chiral semiconductor NPs.[11-15]

The chiral α-HgS NPs, first synthesized by Markovich and co-workers, gave a dissymmetry factor value in absorption, $|g_{abs}|$ ($g_{abs} = \Delta\varepsilon/\varepsilon$), of 0.012, which was larger than those of CdSe and CdTe by 2 orders of magnitude.[16] The synthesis of HgS NPs proceeded through the initial formation of metacinnabar (β-HgS) NPs with an achiral cubic phase which was consequently converted to the chiral cinnabar α-HgS phase in the presence of chiral thiols (Chapter 2-2).[16,17] Since the achiral thiols could not afford this phase transition (Chapter 2-2),[17] the chiral thiol ligands served as a chiral inducer in the synthesis of HgS NPs. The enantiomeric binding arrangement of chiral ligands on the NP surface has been reported to determine the optical activity of CdSe and CdTe NPs with an achiral core.[18-22] While the chiral binding structure of chiral ligands could stabilize the one-handed crystal structure of α-HgS selectively, an identical chiral ligand could even form different coordination patterns.[17,23] An enantiopure ligand system could stabilize both the right- and left-handed cinnabar structures through different coordination patterns, which led to an inversion of optical activity in a solution of α-HgS NP ensembles (Chapter 3).[23] The heating treatment of the solution resulted in the shift of NP population from the initial kinetically stable ones to the thermodynamically stable diastereomeric ones with opposite handedness.[23] Given this experimental result, the use of enantiopure ligands could not necessarily provide enantiopure HgS NPs with identical handedness. Although the giant optical activity of HgS NPs may offer promising performance, the control of enantioselectivity or enantiopurity in the synthesis of chiral NPs still remains an important issue toward applications such as chiral catalysts.[24-26]

In Chapter 4, I therefore unveil the effect of preparation condition of α-HgS NPs on their optical

activity. A detailed investigation on the chiral induction suggests the presence of critical size of NPs for the phase transformation from an achiral cubic to a chiral cinnabar phase. The elevation of preparation temperature results in the enhancement of optical activity, leading to the maximum $|g_{abs}|$ value of up to 0.02, which is higher than the reported value for HgS NPs[16] using (D, L)-penicillamine (Pen) by 75%, and the highest value for semiconductor-based chiral NPs reported so far. The effect of temperature on the evolution of optical activity is discussed based on the Ostwald ripening growth mechanism, which amplified the enantioselectivity induced by the chiral Pen ligand.

4-2. Size-dependent chiral induction in NPs.

HgS NPs were prepared in an aqueous solution of mercury nitrate and D-Pen ligand upon addition of thioacetamide at various temperatures in the range of 5−80 ºC. The reaction mixture became dark-brown immediately after the addition of thioacetamide, corresponding to the formation of achiral β-HgS NPs (Chapter 2-2). These transiently formed β-HgS NPs were reported to exhibit negligible optical activity in the visible region.[16] The color of the solution turned orange owing to the transformation into the thermodynamically favored cinnabar phase.[16,17] The rate of this phase transition event varied depending on the preparation temperature. The formation of α-HgS NPs was completed within 1 h at 80 ºC, whereas it took more than 4 days at 5 ºC, which was monitored by a temporal evolution of absorption spectra (Figure 4-1). The completion of β-to-α phase transition was confirmed by the disappearance of light absorption above 570 nm, since the bulk band gap of α-HgS is 2.2 eV, corresponding to the absorption edge at 564 nm.[17] It was noted that even after the absorption spectral change was almost complete, the CD activity continued to increase. For example, the disappearance of β-HgS NPs took 3 hours, whereas the increase of the g_{abs} value continued until 24 hours after the initiation of NP formation at 25 ºC (Figure 4-1a-c). Therefore, I identified the completion of the synthesis of α-HgS NPs by the saturation of the CD spectral change, reaching a thermodynamically equilibrated state at the given temperature. The powder X-ray diffraction (XRD) measurements confirmed the formation of the cinnabar phase for NPs prepared in the temperature range of 5−80 ºC (Figure 4-2).

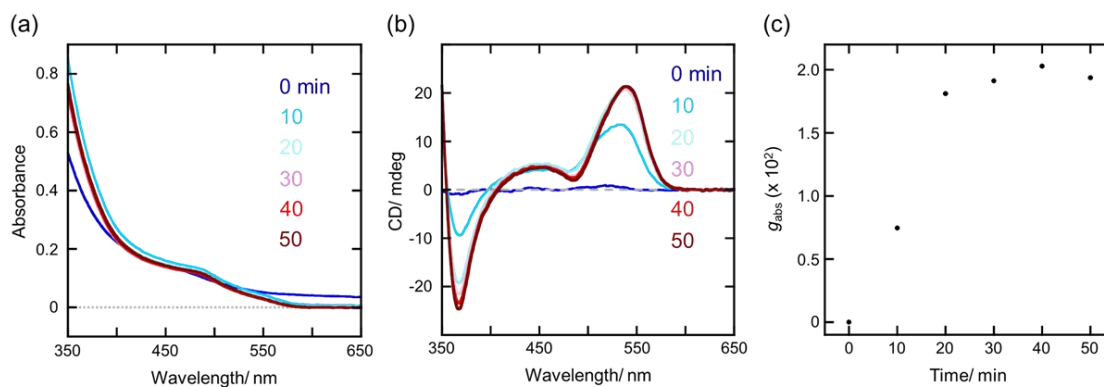prepared at 5 °C
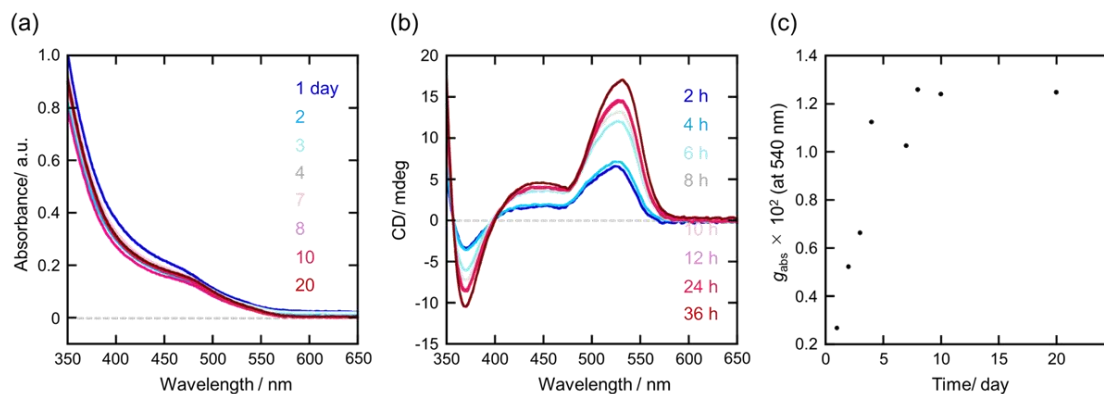
prepared at 25 °C
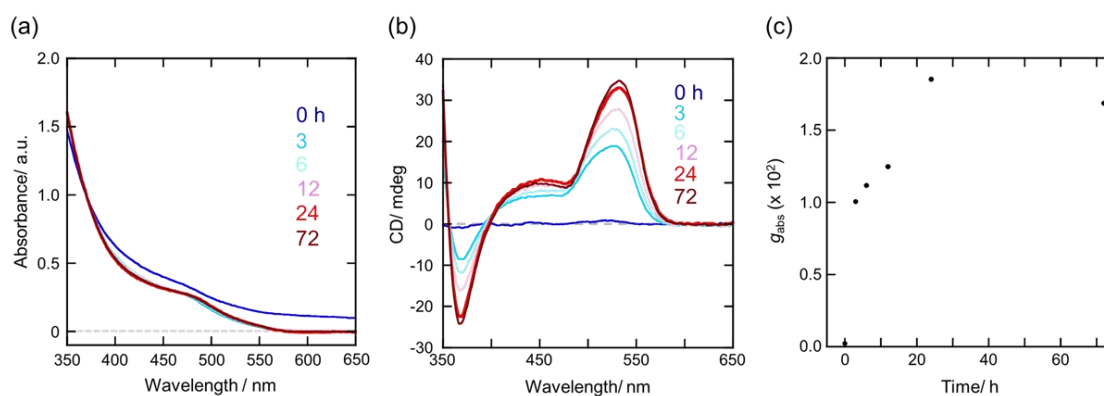
prepared at 80 °C

Figure 4-1. Time evolution of (a) absorption and (b) CD spectra of HgS NPs prepared at various temperatures. (c) Plots of g_{abs}-value of HgS NPs as a function of reaction time.
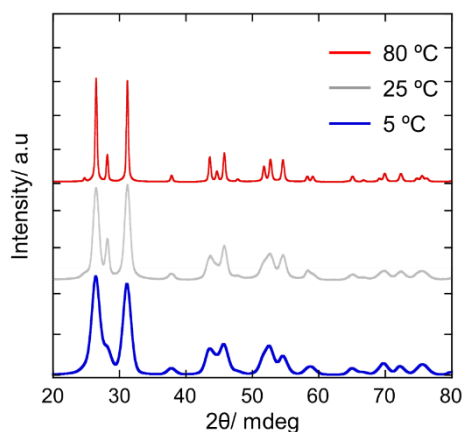
Figure 4-2. XRD profiles of D-Pen-capped HgS NPs prepared at 5 ºC (blue), 25 ºC (grey) and 80 ºC (red).

The β-to-α phase transformation in HgS NPs was promoted only in the presence of chiral ligands (Chapter 2-2).[17] This chiral induction process in the preparation of NPs was investigated at 25 ºC using the absorption spectral change and transmission electron microscopy (TEM) measurements. The dissipation of β-HgS NPs was monitored by the decrease of absorbance at 600 nm (Figure 4-3), which led to a rough estimation of metacinnabar content between 100 and 0%. The absorbance at 600 nm increased for 20 min after the addition of thioacetamide and then decreased continuously. The NPs purified at 20 min after the addition of thioacetamide possessed the cubic metacinnabar phase (Figure 4-4), corresponding to 100% content of β-HgS NPs. TEM observation revealed that the β-HgS NPs have a spherical or polyhedral shape with an average diameter of 3.6 nm (Figure 4-5a,b). The content of β-HgS NPs gradually decreased, which was accompanied by an increase of the average NP size (Figure 4-5). Consequently, the shape of NPs shifted to a prolate spheroidal shape with the elongation along the *c*-axis.[27] A careful analysis of the average NP size clearly suggested the critical size for the β-to-α transformation. The NPs with 100% β-HgS content negligibly included NPs of size larger than 5.5 nm (Figure 4-5b), whereas the NPs after the 100% β-to-α transformation did not possess NPs of size less than 5.5 nm (average length: 9.8 nm, Figure 4-5j). Between 0 and 100% α-HgS content, the abundance of NPs larger than 5.5 nm roughly accorded with that of α-HgS NPs estimated by the absorption spectral change (Figures 4-3 and 4-5). This experimental result indicated that NPs should grow over 5.5 nm to trigger the β-to-α transformation. In other words, the most stable phase is shifted from the cubic (metacinnabar) to the trigonal (cinnabar) phase across the NP size of 5.5 nm. Such size-dependent stabilization of specific crystal structures has been reported for some inorganic compounds including zirconia and polar metal oxides.[28-30] Smaller NPs are considered to prefer an isotropic (cubic) to anisotropic (trigonal) morphology to reduce the effect of increased surface energy with decreasing NP size.[29,30]
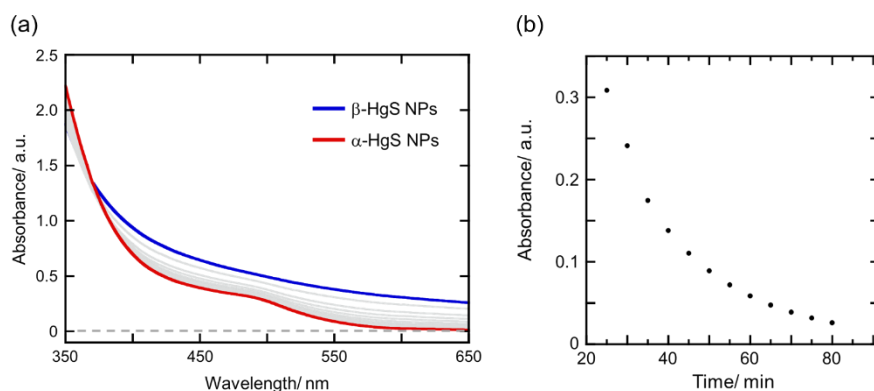
Figure 4-3. (a) Absorption spectral change and (b) temporal change of Abs. at 600 nm in the synthesis of HgS NPs at 25 ºC after the addition of thioacetamide.
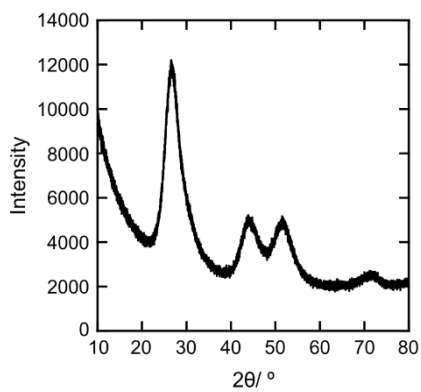

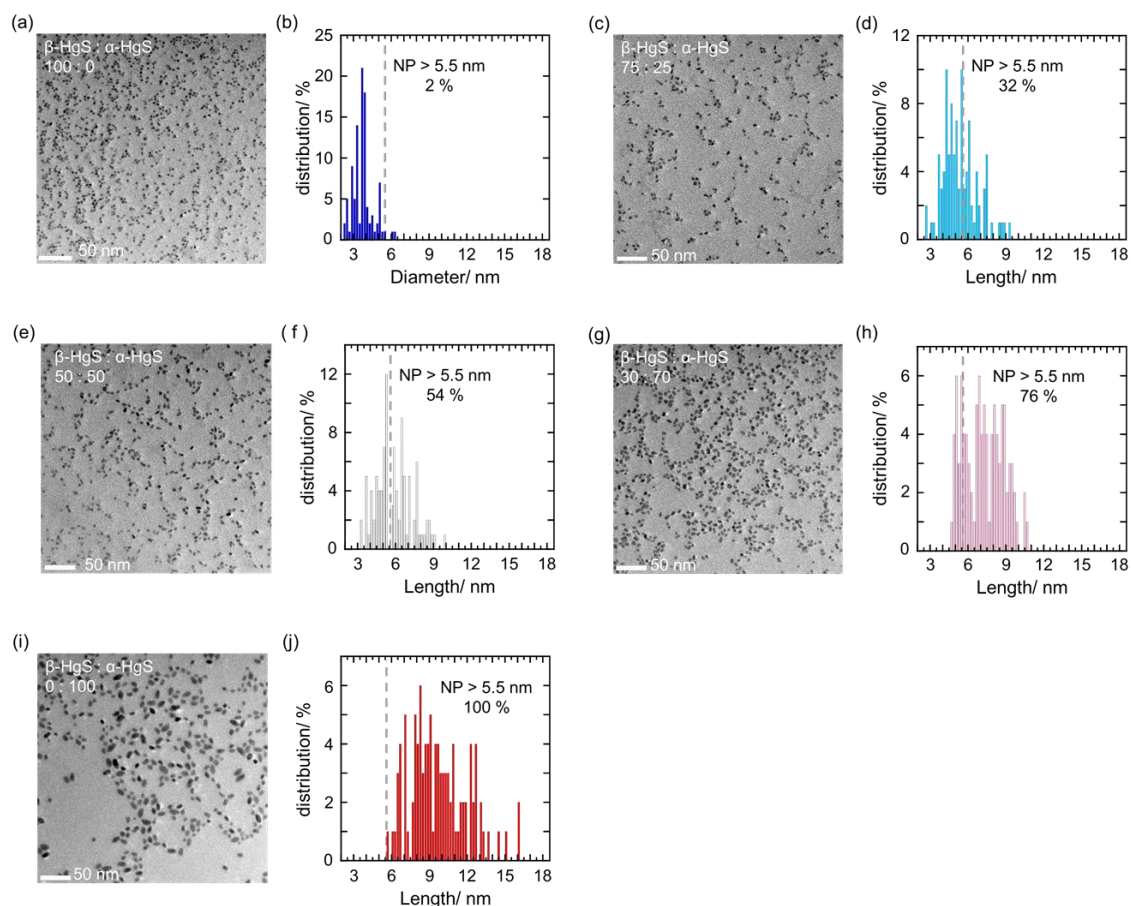**Figure 4-4**. XRD profile of D-Pen-capped β-HgS NPs prepared at 20 min after the addition of thioacetamide.

Figure 4-5. TEM images and size-distributions of HgS NPs prepared at 25 ºC monitored during β-to-α transition.

4-3. Relationship between NP size and optical activity.

TEM and scanning TEM (STEM) images revealed that the prolate spherical-shaped α-HgS NPs were composed of a single crystalline structure as reported in the previous studies (Figure 4-6).[16,17,27] The NPs prepared at 5 ºC possessed an average width and length of 3.9 and 6.0 nm, respectively. The average size was unchanged after being stored for 20 days at the same temperature (Figure 4-7), indicating that the growth of NPs reached thermodynamic equilibrium at the given temperature when the CD activity became saturated. The average size of NPs showed a clear dependence on the preparation temperature (Figure 4-8). A higher preparation temperature led to a larger average size of NPs. Figure 4-9 exhibits absorption and CD spectra of D-Pen-capped α-HgS NPs prepared at different temperatures. The absence of light absorption above 570 nm clearly demonstrated no contamination with β-HgS NPs for all NP samples.[17] The absorption profiles possessed a broad shoulder at around 480 nm, which slightly shifted to a longer wavelength on increasing the preparation temperature. However, the absorption onset was almost identical for all NPs, indicating a negligible effect of quantum confinement.[35] Interestingly, the CD spectra gave more prominent dependence on the

preparation temperature compared to the absorption spectra. The elevation of preparation temperature resulted in the enhancement of CD activity. For more critical comparison, CD activity was translated to the dissymmetry factor (g_{abs}), which was plotted as a function of preparation temperature (Figure 4-10). The g_{abs} value of 1.1×10^{-2} at 543 nm was obtained for the NPs prepared at 5 °C, whereas it increased with increasing preparation temperature until it reached the maximum value of 2.1×10^{-2} at 551 nm for the NPs synthesized at 50 °C. A further increase in the preparation temperature to 80 °C had a negligible effect on the g_{abs} value (Figure 4-10). A similar temperature-dependent and CD response was observed for the NPs prepared with the L-Pen ligand (Figures 4-11, 4-12).
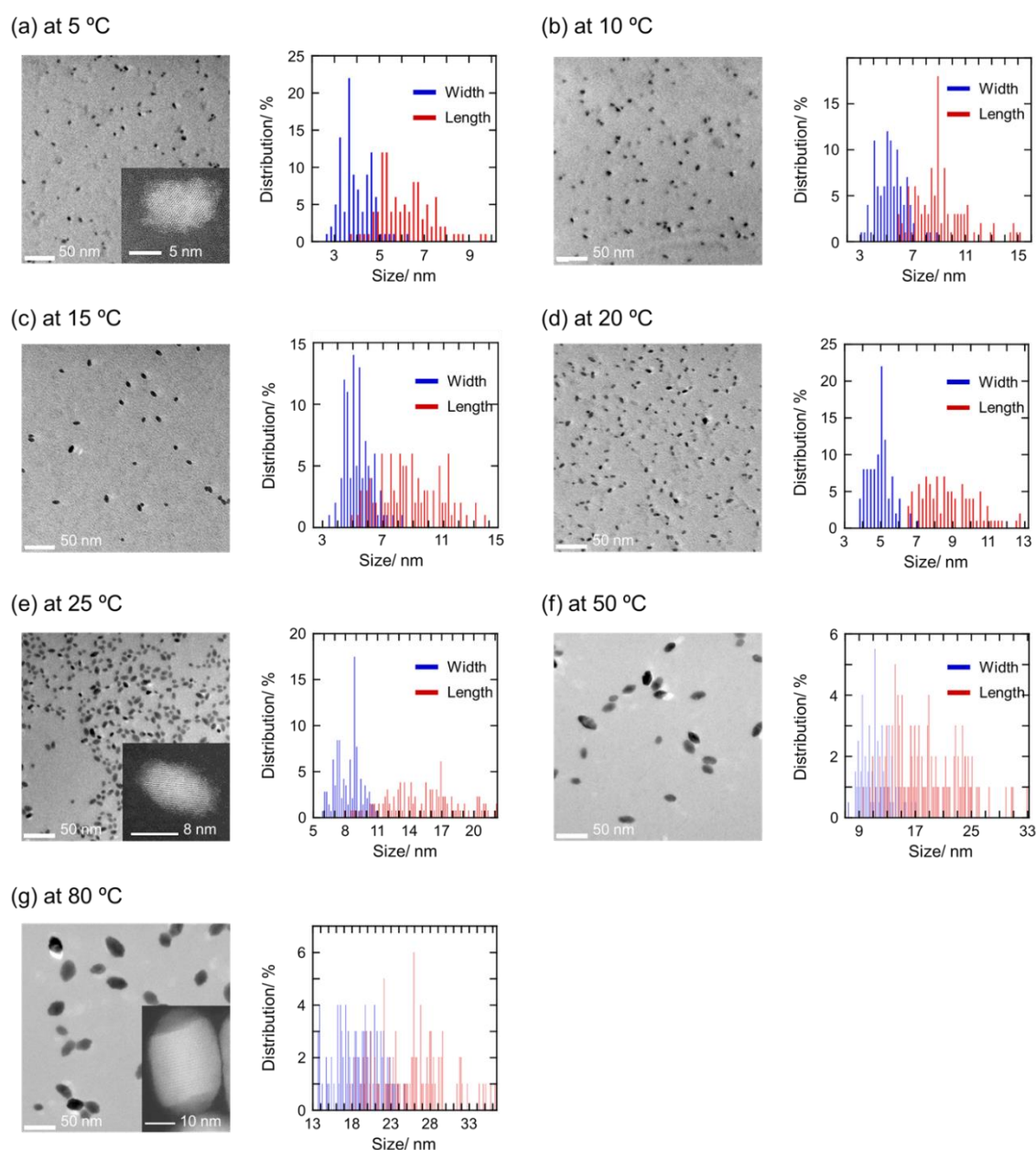
Figure 4-6. TEM images of D-Pen-capped α-HgS NPs prepared at 5−80 °C, together with size distribution. Inset in 5, 25 and 80 °C: STEM images of α-HgS NP
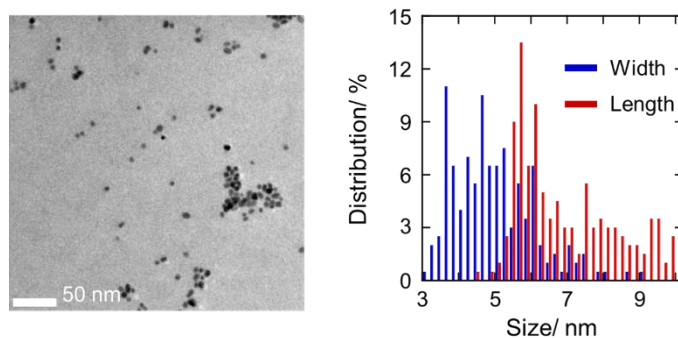
Figure 4-7. TEM images of D-Pen-capped α-HgS NPs stored at 5 ºC for 20 days, together with size distribution.
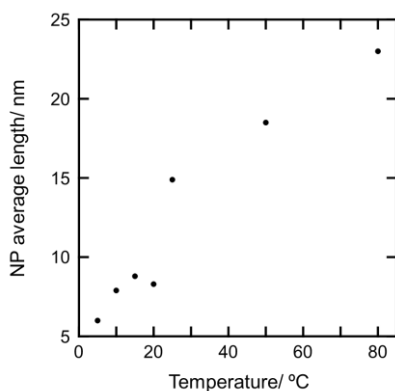

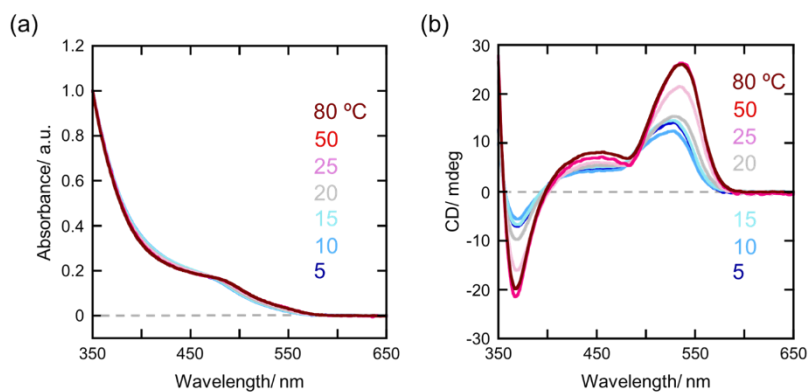**Figure 4-8**. Plots of average length of α-HgS NPs as a function of preparation temperatures.

Figure 4-9. (a) Absorption and (b) CD spectra of D-Pen-capped HgS NPs prepared at different temperatures.
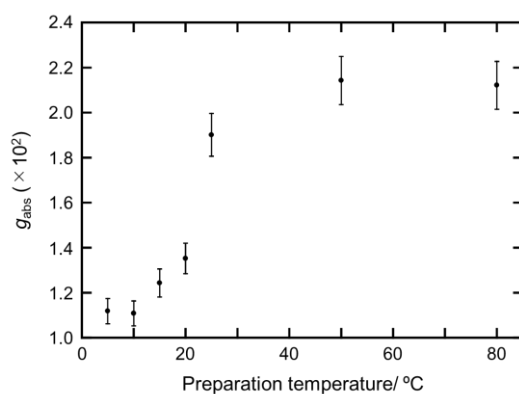
Figure 4-10. Plots of maximum g_{abs} values of D-Pen-capped HgS NPs as a function of preparation temperatures.
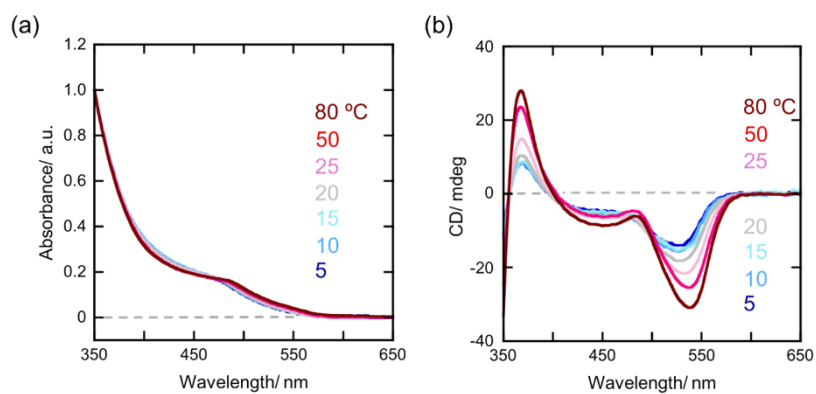

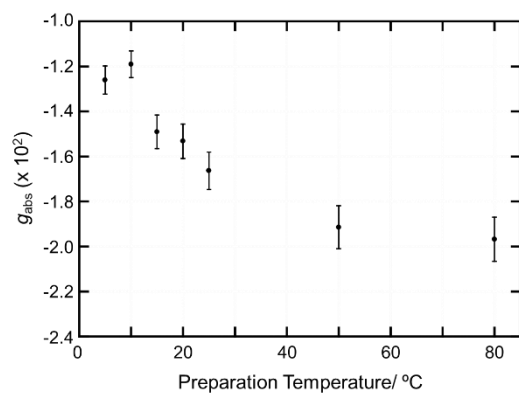**Figure 4-11**. (a) Absorption and (b) CD spectra of L-Pen-capped HgS NPs prepared at different temperatures.

Figure 4-12. Plots of maximum g_{abs} values of L-Pen-capped HgS NPs as a function of preparation temperatures.

.

Thus, the preparation temperature had effects on the size and optical activity of NPs. The higher preparation temperature led to the formation of NPs with larger average sizes and higher g_{abs} values. The plots of maximum g_{abs} value as a function of average size of NPs clearly demonstrated a positive correlation between the average size and optical activity of NPs (Figure 4-13). This experimental fact suggests that the larger size NPs exhibited larger optical activity than the smaller size NPs. However, Markovich[16] and Ouyang[27] reported that the optical activity of α-HgS NPs in the visible range was derived predominantly from the bulk crystallographic chirality of an NP, where all of the helically arranged atoms in a core contributed, being independent of the NP size. In fact, the NPs with the average length of 18.5 and 23.0 nm prepared at 50 and 80 ºC, respectively, exhibited similar g_{abs} values. This result also disagreed with the direct correlation between the size of NPs and optical activity. I also succeeded in the preparation of NPs with larger size at 10 ºC by simply increasing the concentration of precursors by 20% compared to the standard conditions. The obtained NPs possessed the average length of 11 nm (Figure 4-14), which is in the range of NPs prepared between 20 and 25 ºC (10−15 nm) with the standard preparation conditions. Interestingly, even those NPs have similar average sizes; the former NPs prepared at the lower temperature resulted in smaller optical activity (Figure 4-15). The g_{abs} of 1.1×10^{-2} at 547 nm was similar to that of NPs prepared at the same temperature with the standard conditions ($g_{abs} = 1.1 \times 10^{-2}$ at 543 nm), which was apparently smaller than that of NPs with similar average sizes ($g_{abs} = 1.35 - 1.9 \times 10^{-2}$, Figure 4-10). This result also supported the independent relationship between the average size and optical activity of NPs.
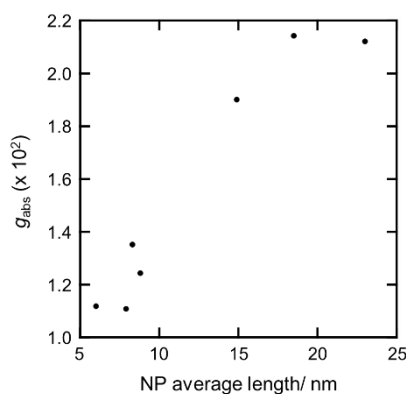

Figure 4-13. Plots of maximum g_{abs} values of D-Pen-capped HgS NPs as a function of their average length.
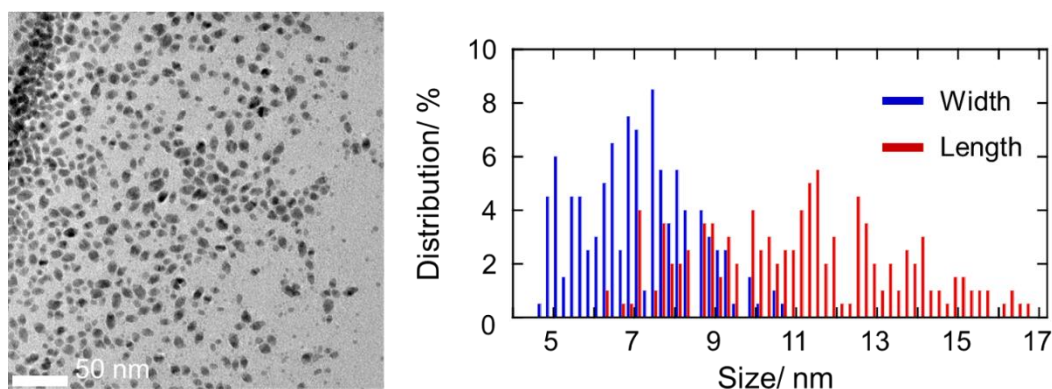
Figure 4-14. TEM image of D-Pen-capped HgS NPs prepared at 10 ºC in the higher concentration of precursors, together with size distribution.
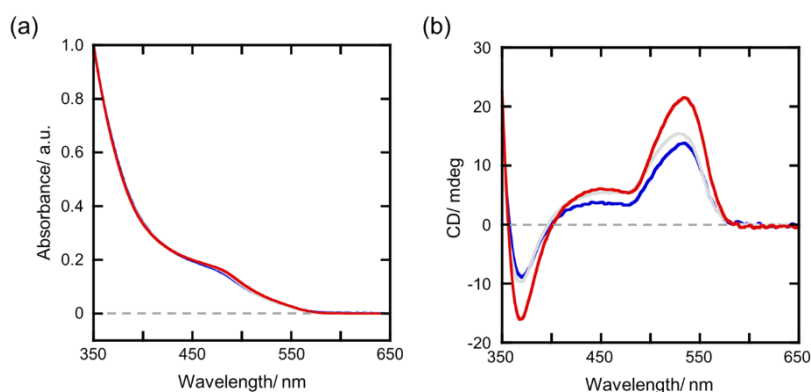

Figure 4-15. (a) Absorption and (b) CD spectra of α-HgS NPs prepared at 10 ºC in the higher concentrations of precursors (blue), and the NPs prepared at 20 ºC (grey) and 25 ºC (red) with the standard condition.

One may consider that the preparation temperature could affect the crystallinity of NPs, which could have an effect on the optical activity of NPs. The average size−crystallinity correlation was compared for the NPs prepared at 5, 25, and 80 ºC with different g_{abs} values. The single-crystal grain sizes were derived from the (003) peak in the XRD profiles using Scherrer's equation. The correlation between the NP size obtained by TEM and the crystal grain size estimated by XRD was found to be independent of the preparation temperature (Figure 4-16). The preparation temperature had little effect on the crystallinity of HgS NPs. Therefore, the difference in the CD activity should be attributed to the enantiopurity of α-HgS NPs. That is, the ratio of NPs between the right- and left-handed cinnabar structures with the space groups of $P3_221$ and $P3_121$, respectively, is dependent on the preparation temperature. The g_{abs} value should be proportional to the enantiomeric excess (*ee*) of NPs or the ratio of NPs with right- and left-handed crystal structures. Synthesis at higher temperatures afforded more enantiopure NPs. This result also suggested that even the enantiopure D-Pen ligand can give α-HgS

NPs with both handedness showing positive and negative CD signals for the first Cotton effect; hereafter referred to as $\alpha^{(+)}$-HgS and $\alpha^{(-)}$-HgS NPs, respectively. The relative population of minor NPs, $\alpha^{(-)}$-HgS NPs, increased by decreasing the preparation temperature. Given that the observed maximum g_{abs}-value of 2.1×10^{-2} corresponded to the *ee* value of 1, the average *ee* of NPs varied from 0.52 to 0.99 with an increase in the preparation temperature from 5 to 50 ºC (Figure 4-10). The synthesis of NPs at room temperature afforded a g_{abs} value of 1.2×10^{-2},[16] resulting in an enantioselectivity of 56% (78:22 for $\alpha^{(+)}$- and $\alpha^{(-)}$-HgS NPs, respectively).
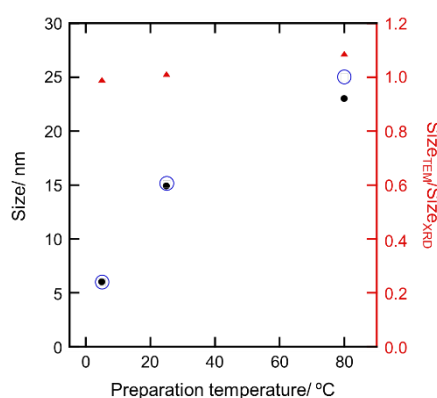

Figure 4-16. Average NP size measured by TEM (black circle) and crystalline domain size estimated by XRD (blue circle) as a function of preparation temperature for D-Pen-capped α-HgS NPs. Red triangle: plots of relative average NP size estimated by TEM and XRD (Size$_{TEM}$/Size$_{XRD}$).

I further investigated the size-dependent optical property of NPs by their size-dependent separation. A solution of HgS NPs prepared at 25 ºC with the g_{abs} value of 1.77×10^{-2} was subjected to centrifugation at 15 000 rpm (18 400 g) for 10 min. This process successfully deposited a sediment at the bottom of the centrifuge tube. The precipitate was redispersed in deionized water, and absorption and CD spectra and average size were compared with those of NPs in the supernatant. The TEM images clearly differentiated between the average sizes (lengths) of NPs in the supernatant and precipitate, which were 9.2 and 12.6 nm, respectively (Figure 4-17). Both NPs separated by the size-dependent precipitation procedure gave almost identical absorption profiles (Figure 4-18a), whereas the NPs in the precipitate afforded larger CD activity (Figure 4-18b). The g_{abs} values were estimated to be 1.63 and 1.98×10^{-2} for the NPs in the supernatant and precipitate, respectively (Figure 4-18c). Thus, this experiment clearly demonstrated that the CD activity of the NPs ensemble is a consequence of the sum of positive and negative contributions of individual NPs with opposite enantiomeric crystal structures.
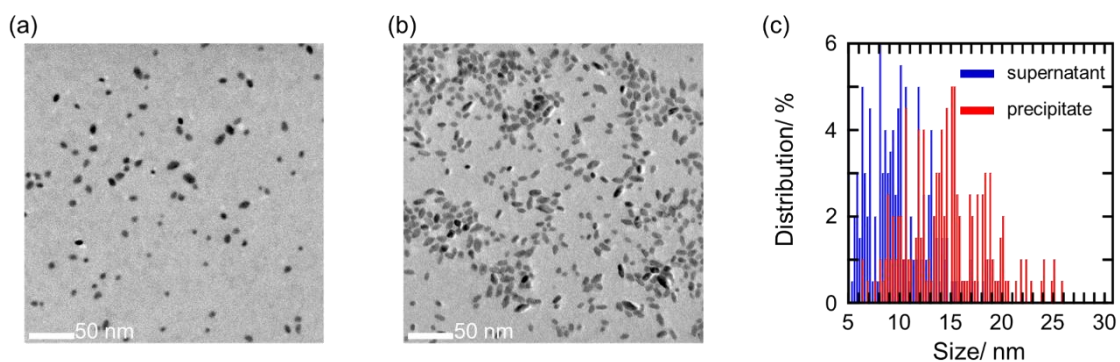
Figure 4-17. (a, b) TEM images and (c) size distribution of HgS NPs in the supernatant (a) and precipitate (b) after the centrifugation procedure.
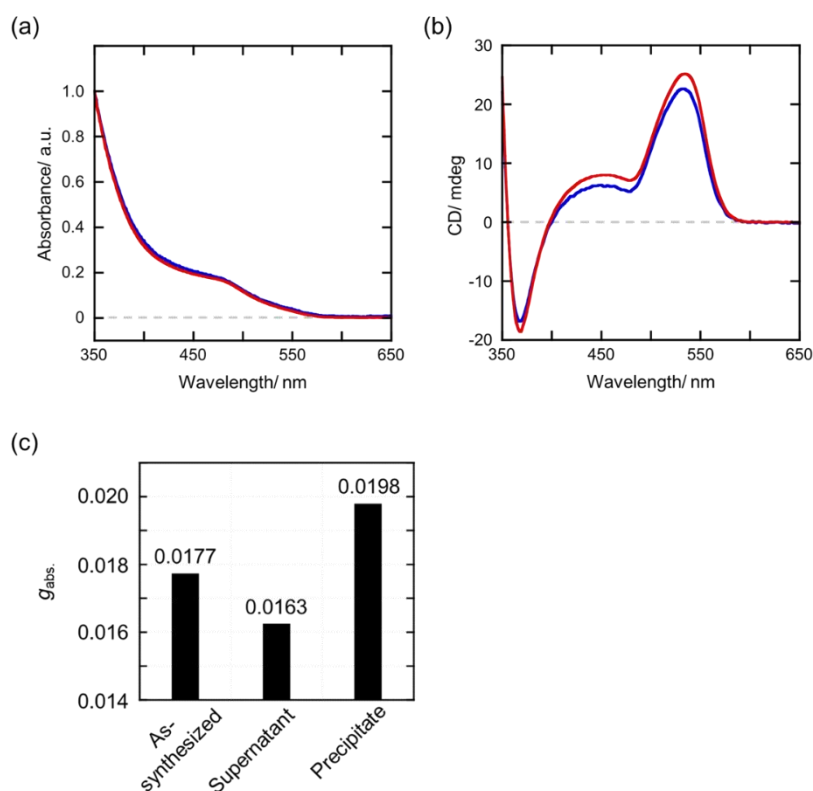

Figure 4-18. (a) Absorption and (b) CD spectra of α-HgS NPs in the supernatant (blue) and the precipitate (red) after the centrifugation procedure. (c) Change in the g_{abs} values before and after the size separation.

4-4. Evolution of enantiopurity of NPs via Ostwald ripening.

Taking the size-dependent optical activity of NPs into account, it is considered that the synthesis of α-HgS NPs involves the growth of NPs and the concomitant evolution of enantiopurity. The growth of NPs of size over 5.5 nm triggers the β-to-α phase transformation. Considering that the size

distribution of α-HgS NPs is apparently larger than that of β-NPs (Figure 4-5), the growth of α-HgS NPs seems to proceed mainly via the Ostwald ripening process, in which smaller NPs are consumed to dissolve into monomers for the growth of larger NPs.[31-33] The depletion of monomers in the stage of β-HgS NP formation could set off this mechanism in the subsequent stage of α-HgS NP growth. While smaller β-HgS NPs were also consumed for the growth of larger α-HgS NPs, the Ostwald ripening process among the α-HgS NPs should have a more prominent impact on the evolution of enantiopurity or *ee* of NPs.

To gain an insight into this assumption, I performed the following experiment. The NPs just after the β-to-α transformation at 5 ºC were purified by repetitive precipitation−redispersion processes (three times) to remove the unreacted ionic species and free ligands. The precipitate composed of the smallest α-HgS NPs was redispersed in deionized water and subjected to heating at 80 ºC to monitor the growth of NPs. The growth of NPs was identified by TEM measurements (Figure 4-19). After the heating treatment for 120 min, the HgS NPs possessed a nanorod shape, which was different from that obtained by the direct synthesis at 80 ºC with a prolate spherical shape (Figure 4-6). The reduced concentration of the free Pen ligand after the purification process may trigger the directional growth along the *c*-axis,[27] which is clearly recognized by a high-resolution STEM image (Figure 4-19c). The average length of NPs and its distribution changed from 7.4 nm and 21% to 15.0 nm and 66 %, respectively, after the heating treatment for 120 min (Figure 4-19). The significant broadening in the size distribution along with the growth of NPs is a characteristic of the Ostwald ripening process.[31,33] Moreover, the heating treatment of the redispersed solution led to the enhancement of optical activity, whereas only a slight red shift was noted in the absorption spectral change (Figures 4-20). The maximum g_{abs} value increased from 1.1×10^{-2} to 1.8×10^{-2} by the heating treatment at 80 ºC for 120 min (Figure 4-21). Further extension of heating treatment time resulted in the aggregation of NPs. Thus, the increase in the enantiopurity of NPs is coincided with the Ostwald ripening-aided growth of NPs. It was noted that morphology of NPs changed to the nanorod shape. Ouyang and co-workers investigated experimentally and theoretically the effect of shape of NPs on the chiroptical property of cinnabar NPs.[27] While the chirally twisted morphology of NPs gave prominent CD signals in the UV−vis range, the effect of nonchiral shapes such as ellipsoid, cube, nanorod, and nanowire on the CD profile was limited. Therefore, it was reasonably considered that the α$^{(-)}$-HgS NPs were consumed and the growth of α$^{(+)}$-HgS NPs was facilitated in the Ostwald ripening stage, which resulted in the increase of optical activity.
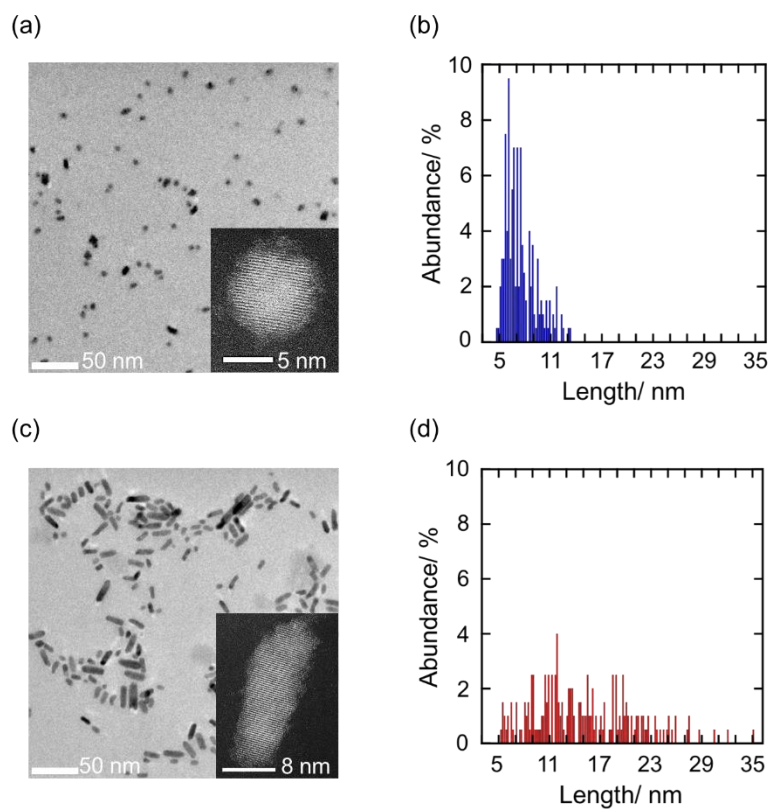
Figure 4-19. (a, c) TEM and STEM (inset) images, and (b, d) size distributions of HgS NPs (a, b) before and (c, d) after the heating treatment at 80 ºC for 120 min.
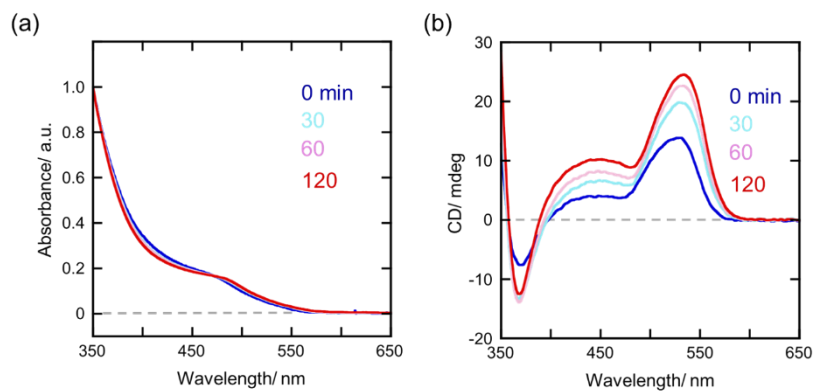

Figure 4-20. (a) Absorption and (b) CD spectral change for the HgS NPs prepared at 5 ºC followed by heating treatment at 80 ºC.
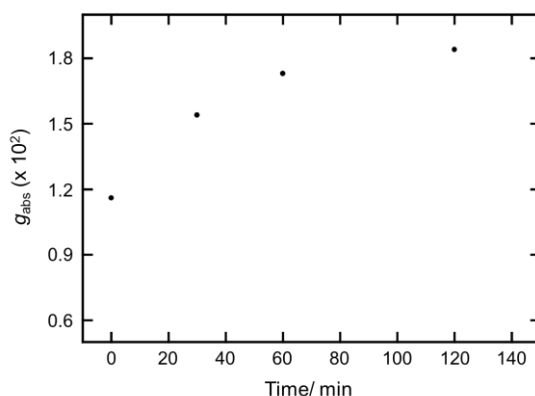
Figure 4-21. Temporal evolution of g_{abs} value at the CD peak position for the HgS NPs prepared at 5 °C followed by heating treatment at 80 °C.

I have described that even an identical enantiomeric ligand, *N*-acetyl-L-cysteine (Ac-L-Cys), could induce the formation of both $\alpha^{(+)}$- and $\alpha^{(-)}$-HgS NPs through different bidentate coordination configurations on the surface of NPs (Chapter 3-3).[17,23] The bidentate coordination with thiolate and amide-carbonyl preferentially stabilized the left-handed $\alpha^{(+)}$-HgS, whereas the one with thiolate and carboxylate stabilized the opposite one ($\alpha^{(-)}$-HgS).[23] The response of optical activity to the change of surface coordination structure has also been reported for the Cys-capped CdSe/CdS core/shell NPs.[22] A similar mechanism may explain the formation of both $\alpha^{(+)}$- and $\alpha^{(-)}$-HgS NPs with the enantiomeric D-Pen. The Pen ligand is possible to coordinate to the surface of NPs with multidentate coordination structures using thiolate, carboxylate, and amine. In a similar manner to Ac-L-Cys, the bidentate coordination of D-Pen using thiolate and carboxylate (S−COO) could preferentially stabilize the $\alpha^{(+)}$-HgS NPs (Figure 4-22).[23] The coordination with thiolate and amine (S−NH$_2$) may stabilize contrarily the opposite $\alpha^{(-)}$-HgS NPs. The HgS NPs prepared at different temperatures were investigated with FTIR spectroscopy. To prepare the samples for FTIR analysis, Pen-stabilized HgS NPs were purified to remove free ligands as much as possible, giving dry powder samples. FTIR spectra in the range of 1250−1750 cm^{-1} were investigated in detail, in which carboxylate and amine groups afforded characteristic peaks (Figure 4-23). The free Pen ligand gave a number of peaks in this region.[34] The symmetric and asymmetric stretching vibration modes of carboxylate, $\nu_s(COO^-)$ and $\nu_{as}(COO^-)$, respectively, were more sensitive to coordination with metal atoms on the NP surface.[35] For example, the coordination of carboxylate on the surface of CdSe NP resulted in a red shift of the $\nu_{as}(COO^-)$ mode and a blue shift of the $\nu_s(COO^-)$ mode.[20] The stretching vibration modes were found at 1587 and 1394 cm^{-1} corresponding to $\nu_{as}(COO^-)$ and $\nu_s(COO^-)$, respectively, in the FTIR spectrum of the deprotonated D-Pen ligand (Figure 4-23a).[34] While both the peaks broadened, the former and latter peaks exhibited red and blue shifts to 1430 and 1560 cm^{-1}, respectively, on the HgS NPs prepared at 5 °C (Figure 4-23b). Each broad peak could be divided into two individual components including free

carboxylate and metal-bound (COO-Hg) one. The relative absorption of free carboxylate components $\nu(COO^-)$ decreased in the HgS NPs prepared at 80 ºC compared to the NPs prepared at 5 ºC (peak no. 1 vs 2 and 4 vs 3, Figure 4-23b,c). Meanwhile, the ν_s(COO-Hg) peak exhibited a further blue shift, whereas the ν_{as}(COO-Hg) shifted to a higher wavenumber. As a result, the peak splitting between ν_s(COO-Hg) and ν_{as}(COO-Hg) increased from 95 to 120 cm^{-1}. This change may include a shift of the coordination mode of carboxylate from chelating to bridging modes.[20,35] Thus, the FTIR study suggested stronger binding of carboxylate to the surface of NPs prepared at 80 ºC than those prepared at 5 ºC.

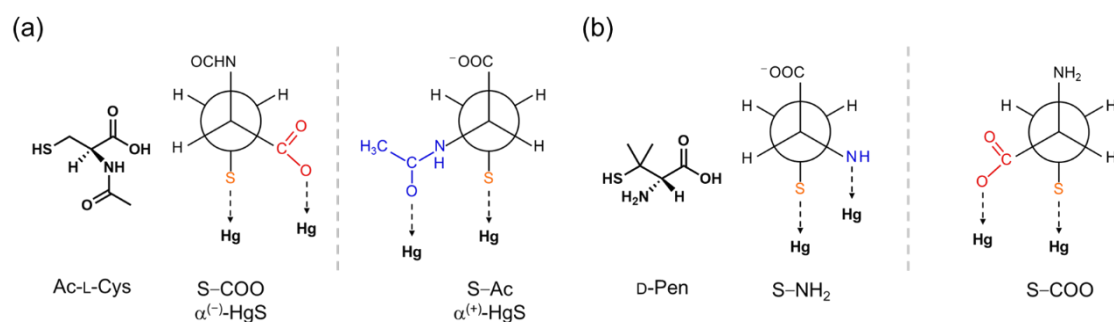

Figure 4-22. Illustrations of coordination configurations of (a) Ac-L-Cys and (b) D-Pen on the surface of a HgS NP.
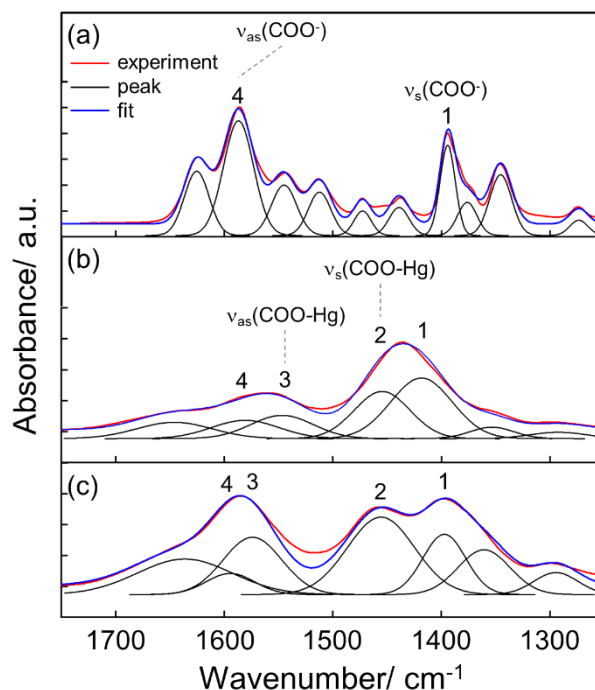

Figure 4-23. ATR-IR spectra of (a) free D-Pen and D-Pen-capped α-HgS NPs prepared at (b) 5 ºC and (c) 80 ºC.

Based on the experimental results described above, in this chapter I proposed a mechanism for the evolution of enantiopurity along with the growth of NPs in the synthesis of α-HgS NPs (Figure 4-24). The addition of thioacetamide to the solution of Hg^{2+} with D-Pen resulted in the rapid formation of β-HgS NPs (stage A in Figure 4-24). The growth of HgS NPs of size over 5.5 nm induced the β-to-α phase transformation (chirality induction). On the basis of the bidentate coordination mode, the D-Pen ligand could give both handedness of $\alpha^{(+)}$- and $\alpha^{(-)}$-HgS NPs with different stability (stage B). While the smaller NPs dissociated into the monomeric species in the Ostwald ripening process, NPs with lower stability and higher surface energy markedly contributed in this stage (stage C). Hence, the minor $\alpha^{(-)}$-HgS NPs dissolved more rapidly providing monomeric species to the growing major $\alpha^{(+)}$-HgS NPs (stage D). The dissolution of smaller NPs required excess thermal energy, which was facilitated at a higher temperature, resulting in preparation-temperature being dependent optical activity. The effect of the Ostwald ripening on the enhancement of optical activity might reach saturation at 50 ºC since further heating at 80 ºC led to a negligible improvement in the g_{abs} value (Figure 4-10). A similar mechanism for the enhancement of enantiopurity has already been demonstrated in the crystallization of small organic molecules that undergo racemization in the solution phase.[36-38] The Ostwald ripening or Viedma ripening processes facilitate the deracemization of intrinsically chiral molecules in the crystalline phase. In the present case, the intrinsically chiral HgS formed both $\alpha^{(+)}$- and $\alpha^{(-)}$-HgS NPs, whereas the presence of the chiral inducer, D-Pen, led to the selective formation of $\alpha^{(+)}$-NPs. Moreover, the Ostwald ripening-aided growth process amplified the enantioselectivity in the synthesis of HgS NPs.
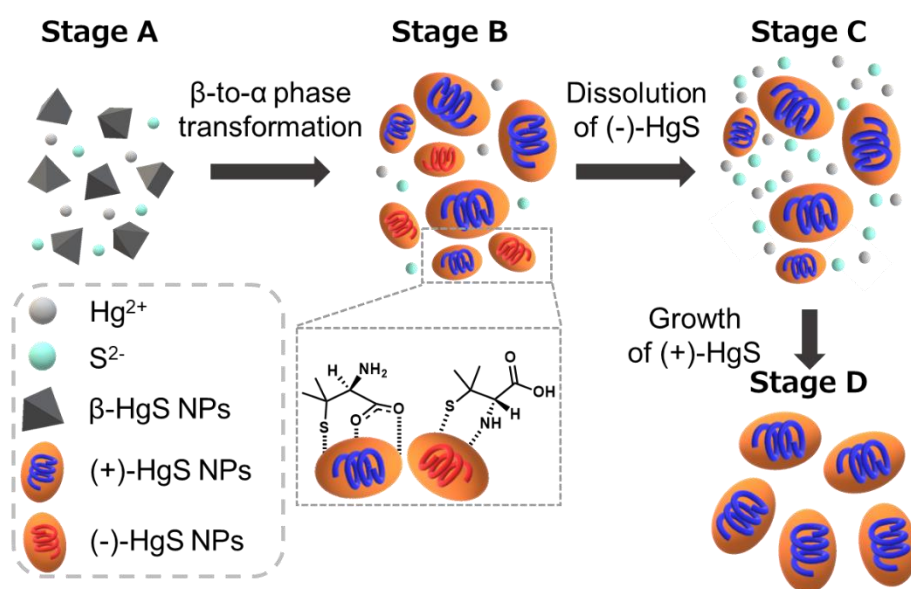

Figure 4-24. Schematic mechanism for the evolution of enantiopurity in D-Pen-capped α-HgS NPs with the aid of the Ostwald ripening process.

4-5. Conclusions.

In summary, a detailed study on the formation and growth of α-HgS NPs led to two significant findings. First, a critical size of 5.5 nm seemed to exist for the transformation from the achiral β-phase to the chiral α-phase in the chiral induction stage. Second, the optical activity of HgS NPs was dependent on the preparation temperature and consequently on the average size of NPs. NPs with larger average size possessed higher enantiopurity in the handedness of the NP core structure, which was achieved by the growth of NPs aided by the Ostwald ripening process. The present work not only gives an important insight into the enantioselective synthesis of nanomaterials but may also provide implications for the development of homochirality in nature, in which intrinsically chiral minerals are believed to play an important role.[39]
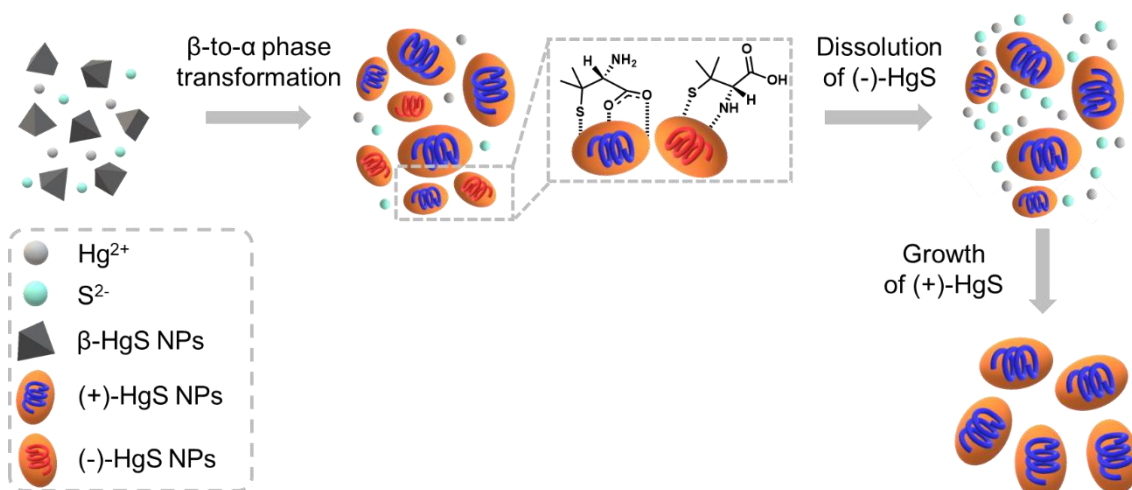
4-6. Experimental; Synthesis and characterization.

HgS NPs were prepared and purified according to the method reported by Markovich and co-workers. As a standard condition, an aqueous solution (4.8 mL) of a mixture of $Hg(NO_3)_2$ (19 mM) and D (or L)-Pen ligand (19 mM) was prepared, in which the pH value was adjusted to ca. 11.5 by the addition of 1 M NaOH aqueous solution. To the solution, 0.9 mL of aqueous thioacetamide solution (100 mM) was added and the mixture was vigorously stirred for a certain period of time at various temperatures. Five samples were prepared at the same temperature to obtain an average anisotropy factor g_{abs}-value. For the purification procedure, repetitive precipitation−redispersion processes (three times) using acetone and water, successively were performed to remove unreacted species.

UV−vis absorption spectra were recorded at room temperature using a JASCO V-670 spectrophotometer. Circular dichroism (CD) spectra were measured by a JASCO J-725 spectropolarimeter. The g_{abs}-value was derived from the equation $g_{abs} = \theta$ [mdeg]/(32 980·Abs.) using CD (θ: ellipticity) and absorbance (Abs.) data at the wavelength of CD peak position. Fourier transform infrared (FTIR) study was performed using a JASCO FT/IR-4200 equipped with an attenuated total reflection (ATR) unit (ATR-PRO ONE, JASCO). The samples for the FTIR study were purified to remove the excess free Pen ligand. Transmission electron microscopy (TEM) observation was conducted with a JEOL JEM-2200FS electron microscope. High-resolution high-angle annular dark-field scanning TEM (HAADF-STEM) measurement was performed using a Hitachi HD-2700. Specimens for TEM and STEM measurements were prepared by drop-casting of solutions of NPs onto a carbon-coated copper grid. Powder X-ray diffraction (XRD) profiles were recorded using a Rigaku SmartLab X-ray diffractometer with Cu Kα radiation (λ = 0.154 nm). The crystal grainsize was calculated by Scherrer's equation ($L = \lambda K (bcos\theta)^{-1}$), where L, K, b, and θ are the crystal size, shape factor (K = 0.9), full width at half-maximum of the deconvoluted (003) peak, and diffraction angle (2θ = 28.1°), respectively.

4-7. References.

1   Y. Yin, A. P. Alivisato, Colloidal Nanocrystal Synthesis and the Organic-Inorganic Interface. *Nature* **2005**, 437, 664−670.

2   Y. Xia, Y. Xiong, B. Lim, S. E. Skrabalak, Shape-Controlled Synthesis of Metal Nanocrystals: Simple Chemistry Meets Complex Physics? *Angew. Chem., Int. Ed*. **2009**, 48, 60−103.

3   M. J. Enright, B. M. Cossairt, Synthesis of tailor-made colloidal semiconductor heterostructures, *Chem. Commun.* **2018**, 54, 7109−7122.

4   B. Mahler, N. Lequeux, B. Dubertret, Ligand-Controlled Polytypism of Thick-Shell CdSe/CdS Nanocrystals. *J. Am. Chem. Soc*. **2010**, 132, 953−959.

5   W. Nan, Y. Niu, H. Qin, F. Cui, Y. Yang, R. Lai, W. Lin, X. Peng, Crystal Structure Control of Zinc-Blende CdSe/CdS Core/Shell Nanocrystals: Synthesis and Structure-Dependent Optical

Properties. *J. Am. Chem. Soc*. **2012**, 134, 19685−19693.

6   K. B. Subila, G. K. Kumar, S. M. Shivaprasad, K. G. Thomas, Luminescence Properties of CdSe Quantum Dots: Role of Crystal Structure and Surface Composition. *J. Phys. Chem. Lett*. **2013**, 4, 2774−2779.

7   X. Gao, X. Zhang, L. Zhao, P. Haung, B. Han, J. Lv, X. Qiu, S. H. Wei, Z. Tang, Distinct Excitonic Circular Dichroism between Wurtzite and Zincblende CdSe Nanoplatelets. *Nano Lett*. **2018**, 18, 6665−6671.

8   A. Puzder, A. J. Williamoson, N. Zaitseva, G. Galli, L. Manna, A. P. Alivisayos, The Effect of Organic Ligand Binding on the Growth of CdSe Nanoparticles Probed by Ab Initio Calculations. *Nano Lett*. **2004**, 4, 2361−2365.

9   O. Chen, Y. Yang, T. Wang, H. Wu, C. Niu, J. Yang, Y. C. Cao, Surface-Functionalization-Dependent Optical Properties of II−VI Semiconductor Nanocrystals, *J. Am. Chem. Soc*. **2011**, 133, 17504−17512.

10 T. Kurihara, Y. Noda, K. Takegoshi, Capping Structure of Ligand−Cysteine on CdSe Magic-Sized Clusters, ACS Omega **2019**, 4, 3476−3483.

11 M. P. Moloney, Y. K. Gun'ko, J. M. Kelly, Chiral highly luminescent CdS quantum dots, *Chem. Commun*. **2007**, 3900–3902.

12 S. D. Elliott, M. P. Moloney, Y. K. Gun'ko, Chiral Shells and Achiral Cores in CdS Quantum Dots, *Nano Lett*., **2008**, 8, 2452–2457.

13 T. Nakashima, Y. Kobayashi, T. Kawai, Optical Activity and Chiral Memory of Thiol-Capped CdTe Nanocrystals, *J. Am. Chem. Soc*., **2009**, 131, 10342–10343.

14 Y. Zhou, M. Yang, K. Sun, Z. Tang, N. A. Kotov, Similar Topological Origin of Chiral Centers in Organic and Nanoscale Inorganic Structures: Effect of Stabilizer Chirality on Optical Isomerism and Growth of CdTe Nanocrystals, *J. Am. Chem. Soc*. **2010**, 132, 6006–6013.

15 J. E. Govan, E. Jan, A. Querejeta, N. A. Kotov, Y. K. Gun'ko, Chiral luminescent CdS nano-tetrapods, *Chem. Commun*. **2010**, 46, 6072–6074.

16 A. Ben-Moshe, A. O. Govolov, G. Markovich, Enantioselective Synthesis of Intrinsically Chiral Mercury Sulfide Nanocrystals. *Angew. Chem., Int. Ed*. **2013**, 52, 1275−1279.

17 J. Kuno, T. Kawai, T. Nakashima, The Effect of Surface Ligands on the Optical Activity of Mercury Sulfide Nanoparticles. *Nanoscale* **2017**, 9, 11590−11595.

18 U. Tohgha, K. K. Deol, A. G. Porter, S. G. Bartko, J. K. Choi, B. M. Leonard, K. Varga, J. Kubelka, G. Muller, M. Balaz, Ligand Induced Circular Dichroism and Circularly Polarized Luminescence in CdSe Quantum Dots, *ACS Nano* **2013**, 7, 11094–11102.

19 J. K. Choi, B. E. Hayne, U. Tohgha, L. Pap, K. W. Elliott, B. M. Leonard, S. V. Dzyuba, K. Varga, J. Kubelka, M. Balaz, Chirality Inversion of CdSe and CdS Quantum Dots without Changing the Stereochemistry of the Capping Ligand. *ACS Nano* **2016**, 10, 3809−3815.

20 K. Varga, S. Tannir, B. E. Hayne, B. M. Leonard, S. V. Dzyuba, J. Kubelka, M. Balaz, CdSe Quantum Dots Functionalized with Chiral, Thiol-Free Carboxylic Acids: Unraveling Structural Requirements for Ligand-Induced Chirality. *ACS Nano* **2017**, 11, 9846−9853.

21 M. Puri, V. E. Ferry, Circular Dichroism of CdSe Nanocrystals Bound by Chiral Carboxylic Acids. *ACS Nano* **2017**, 11, 12240−12246.

22 V. A. Kuznetsova, E. Mates-Torres, N. Prochukhan, M. Marcastel, F. Purcell-Milton, J. O'Brien, A. K. Visheratina, M. Martinez-Carmona, Y. Gromova, M. Garcia-Melchor, Y. K. Gun'ko, The Effect of Chiral Ligand Concentration and Binding Mode on Chiroptical Activity of CdSe/CdS Quantum Dots. *ACS Nano* **2019**, 13, 13560−13572.

23 J. Kuno, Y. Imamura, M. Katouda, M. Tashiro, T. Kawai, T. Nakashima, Inversion of Optical Activity in the Synthesis of Mercury Sulfide Nanoparticles: Role of Ligand Coordination. *Angew. Chem., Int. Ed.* **2018**, 57, 12022−12026.

24 X. Gao, B. Han, X. Yang, Z. Tang, Perspective of Chiral Colloidal Semiconductor Nanocrystals: Opportunity and Challenge. *J. Am. Chem. Soc*. **2019**, 141, 13700−13707.

25 B. Pal, S. Ikeda, B. Ohtani, Photoinduced Chemical Reactions on Natural Single Crystals and Synthesized Crystallites of Mercury(II) Sulfide in Aqueous Solution Containing Naturally Occurring Amino Acids. *Inorg. Chem.* **2003**, 42, 1518−1524.

26 H. Shindo, Y. Shirota, K. Niki, T. Kawasaki, K. Suzuki, Y. Araki, A. Matsumoto, K. Soai, Asymmetric Autocatalysis Induced by Cinnabar: Observation of the Enantioselective Adsorption of a 5-Pyrimidyl Alkanol on the Crystal Surface. *Angew. Chem., Int. Ed*. **2013**, 52, 9135−9138.

27 P. P. Wang, S. Yu, A. O. Govolov, M. Ouyang, Cooperative Expression of Atomic Chirality in Inorganic Nanostructures. *Nat. Commun*. **2017**, 8, 14312.

28 T. Yamamoto, H. Niori, H. Morikawa, Particle-Size Dependence of Crystal Structure of $BaTiO_3$ Powder. *Jpn. J. Appl. Phys.* **2000**, 39, 5683−5686.

29 S. Tsunegawa, S. Ito, Y. Kawazoe, J. T. Wang, Critical Size of the Phase Transition from Cubic to Tetragonal in Pure Zirconia Nanoparticles. *Nano Lett.* **2003**, 3, 871−875.

30 P. Chen, X. Xu, C. Koenigsmann, A. C. Santulli, S. S. Wong, J. L. Musfeldt, Size-Dependent Infrared Phonon Modes and Ferroelectric Phase Transition in $BiFeO_3$ Nanoparticles. *Nano Lett*. **2010**, 10, 4526−4532.

31 X. G. Peng, J. Wickham, A. P. Alivisatos, Kinetics of II-VI and III-V Colloidal Semiconductor Nanocrystal Growth: ″Focusing″ of Size Distributions. *J. Am. Chem. Soc*.**1998**, 120, 5343−5344.

32 F. Wang, V. N. Richards, S. P. Shields, E. Buhro, Kinetics and Mechanisms of Aggregative Nanocrystal Growth, *Chem. Mater*. **2014**, 26, 5−21.

33 X. Huang, L. Jing, S. V. Kershaw, X. Wei, H. Ning, X. Sun, A. L. Rogach, M. Gao, Narrowing the Photoluminescence of Aqueous CdTe Quantum Dots Via Ostwald Ripening Suppression Realized by Programmed Dropwise Precursor Addition. *J. Phys. Chem. C* **2018**, 122,

11109−11118.

34 H. Yao, N. Nishida, K. Kimura, Conformational Study of Chiral Penicillamine Ligand on Optically Active Silver Nanoclusters with IR and VCD Spectroscopy. *Chem. Phys*. **2010**, 368, 28−37.

35 A. Y. Koposov, T. Cardolaccia, V. Albert, E. Badaeva, S. Kilina, T. j. Meyer, S. Tretiak, M. Skyora, Formation of Assemblies Comprising Ru-Polypyridine Complexes and CdSe Nanocrystals Studied by ATR-FTIR Spectroscopy and DFT Modeling. *Langmuir* **2011**, 27, 8377−8383.

36 W. L. Noordium, T. Izumi, A. Millemaggi, M. Leeman, H. Meekes, W. J. P. Van Enckevort, R. M. Keellogg, B. Kaptein, E. Vileg, D. G. Blackmond, Emergence of a Single Solid Chiral State from a Nearly Racemic Amino Acid Derivative. *J. Am. Chem. Soc*. **2008**, 130, 1158−1159.

37 W. L. Noordium, E. Vileg, R. M. Keellogg, B. Kaptein, From Ostwald Ripening to Single Chirality. *Angew. Chem., Int. Ed*. **2009**, 48, 9600−9606.

38 L. -C. Sögütoglu, R. R. E. Steedam, H. Meekes, E. Vileg, F. P. J. T. Rutjes, Viedma Ripening: A Reliable Crystallization Method to Reach Single Chirality. *Chem. Soc. Rev*. **2015**, 44, 6723−6732.

39 D. S. Sholl, A. J. Gellman, Developing Chiral Surfaces for Enantioselective Chemical Processing. *AIChE J*. **2009**, 55, 2484−2490.

Chapter 5
Transfer of Chiral Information from Chiral Mercury Sulfide Nanoparticles to Surface Achiral Ligands; Generation of Circularly Polarized Luminescent

5-1. Introduction.

Circularly polarized luminescent (CPL) materials have received broad attention due to their potential applications in 3D displays,[1-4] chiroptical materials,[5] and optoelectronic devices.[6,7] Extensive research studies have been conducted on the development of CPL-active materials based on chiral organic dyes,[8–10] polymers,[11–13] metal complexes,[14,15] and supramolecular assemblies.[16–18] The most common approach to obtain CPL-active dyes is a combination of a chiral moiety with a luminophore linked by a covalent bond.[19] While such chiral organic dyes sometimes require tediously long synthesis procedures, their CPL performance is not always impressive. An alternative approach includes the co-assembly of achiral fluorescence materials with chiral molecules and supramolecular assemblies.[5] The optical activity of chiral molecular systems is successfully transferred into non-chiral luminophores through noncovalent interactions inducing chiral molecular arrangement and/or chiral electronic hybridization. For example, cyclodextrins can incorporate achiral guest dyes in their hydrophobic cavities to achieve CPL generation.[20,21] Helical chiral supramolecular assemblies were also employed to co-assemble with achiral emitting substrates such as dyes,[23,24,26] quantum dots[27,28] and perovskite nanocrystals,[29] successfully providing CPL with various colors. Although chiral organic systems such as chiral receptors and self-assemblies have been well demonstrated as a chiral inducer to obtain CPL activity partnered with achiral organic and inorganic luminophores, the potential of inorganic materials as a chiral template has rarely been explored.[30–32]

Recently, chirality transfer experiments from metal cluster cores with an intrinsically chiral atomic arrangement to the organic ligands attached to the surface of the core have been demonstrated.[33-36] Achiral thiolate ligands coordinated to the surface of the cluster core with a chiral structure adopt a chiral arrangement on its surface, inducing chiral interligand chiral interactions.[33] Very recently, Huang and co-workers demonstrated that the crystallographic chirality on the surface of a chiral silver nanohelix generated by a glancing angle deposition technique was transferred to the stereoselective adsorption of an achiral anthracene derivative.[37] The chirally arranged anthracene molecules exhibited an enantioselective photodimerization on the surface of the nanohelix.[37] Cinnabar (α-HgS) is also a potential candidate for a chiral inorganic template, which crystallizes in the chiral trigonal space group of $P3_121$ (or its enantiomorph $P3_221$). Previous works reported the enantioselective synthesis of colloidal α-HgS nanoparticles (NPs) that possess the chiral crystalline lattice but an achiral

ellipsoidal morphology.[38,39] Furthermore, Ouyang and co-workers succeeded in the preparation of α-HgS nanostructures with independently controlled chiral crystalline lattice and chiral twisted morphology.[40] While the chiral ligand in the initial synthesis of seed NPs defines the crystallographic handedness, the one in the latter growth stage determines the handedness in the twist of morphology with a larger length scale.[40] In Chapter 5, I demonstrate a new CPL-generating system composed of an achiral luminescent molecule **1** (Figure 5-1) and α-HgS NPs with intrinsic chirality. Both the crystallographic and morphological chiralities of HgS NPs were considered as a platform for the chiral arrangement of **1** molecules. The effect of two types of chirality with different scales was examined. The α-HgS nanoellipisoids (NEs) with the achiral shape could not induce CPL of **1**, whereas CPL signals could be observed upon partnered with the nanotwists (NTs) with the chiral morphology (Figure 5-1). The sign of CPL was dependent on the handedness of NT morphology regardless of the crystallographic chirality of NTs.
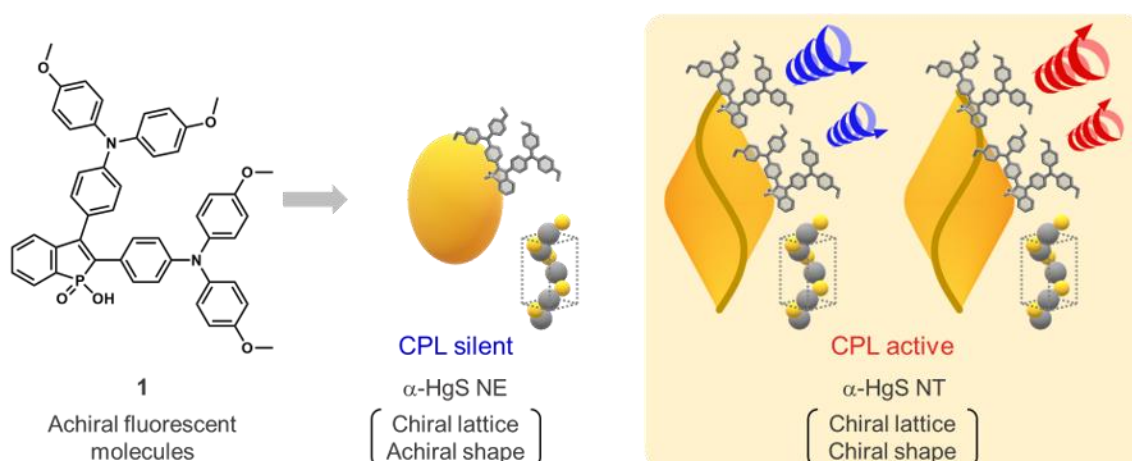

Figure 5-1. Chemical structure of achiral fluorescence molecule **1** (left). Schematic illustration to generate CPL emission of **1** on the surface of α-HgS nanoparticles.

5-2. Design and photophysical properties of the achiral fluorescent molecule.

Benzophosphole *P*-oxide derivatives bearing an triphenylamine group have been extensively investigated to exhibit excellent fluorescent properties based on their donor-acceptor conjugated systems.[41–43] I introduced a phosphonic acid group in a benzo phosphole scaffold, giving a 1-hydroxy-1H-phosphindole 1-oxide moiety, with the aim of anchoring the molecule on the surface of α-HgS NPs.[44–46] I also introduced two triarylamine donor units to form compound **1** with anticipating to induce intramolecular chiral twists over the two single bonds bridging the donor and acceptor units upon interacting with the chiral inorganic surface. Compound **1** was synthesized from 4,4'-(ethyne-1,2-diyl)bis(*N*,*N*-bis(4-methoxyphenyl)aniline) by cyclization with ethyl phenylphosphinate followed

by the hydrolysis of ethyl group (Chapter 5-8). Photophysical study of **1** was performed in DMF (Figure 5-2). The absorption spectrum showed an onset of absorption band at 450 nm with a maximum at 375 nm. The solution exhibit bright yellow-green emission (λ_{max} = 511 nm) with a noticeable fluorescence quantum yield (Φ_F) of 0.17.
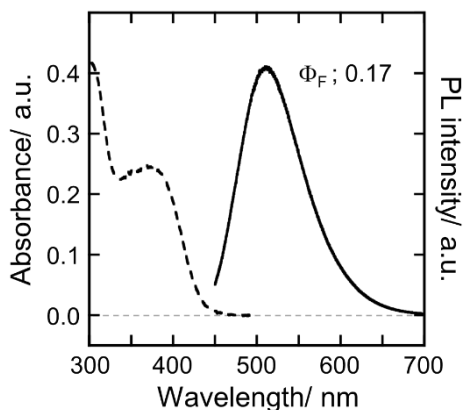

Figure 5-2. UV-vis absorption (dashed line) and emission (solid line) spectra of compound **1** in DMF (1.0×10^{-5} M). Excitation wavelength; 370 nm.

5-3. Preparation of chiral α-HgS NTs modified with compound 1.

HgS NEs were synthesized by a colloidal precipitation method using D- and L-penicillamine (Pen). The absorption spectra gave an absorbance band at 470 nm (Figure 5-3a), attributable to the formation of the cinnabar phase.[38,39] The α-HgS NEs capped with D- and L-Pen showed positive and negative CD signals for the first Cotton effect (hereafter referred to as (+)-NEs and (–)-NEs), respectively, at 540 nm, suggesting the successful induction of crystallographic handedness depending on the chirality of Pen ligand (Figure 5-3b). Transmission electron microscopy (TEM) images of the both NEs exhibited an achiral shape with the same size distributions having the average width and length of 7.4 and 11.3 nm, respectively (Figure 5-4).[38,39]
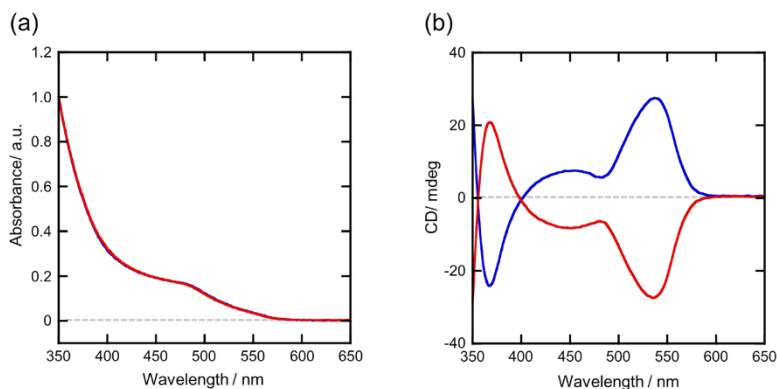

Figure 5-3. (a) UV-vis absorption and (b) CD spectra of α-HgS NEs capped with (blue) D- and (red) L-Pen.
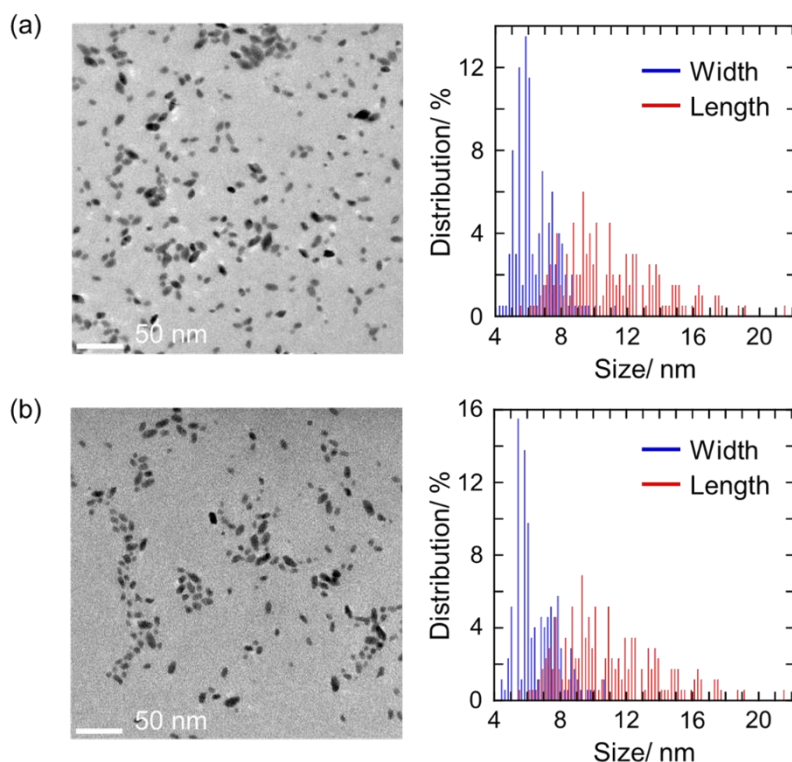
Figure 5-4. Typical TEM images of (+)-NEs (a) and (−)-NEs (b), respectively, together with their size distribution.

I then prepared α-HgS NTs with a twisted triangular bipyramid morphology according to a reported procedure utilizing homo-epitaxial growth of the (+)- and (−)-NEs in the presence of D- and L-Pen, respectively, controlling the handedness of twisting in morphology.[40,47] Figure 5-5 shows typical TEM images of the epitaxially grown NTs from (+)- and (−)-NEs, possessing right-(P) and left-(M) handedness, respectively, in their twisted morphology ((+)P-NTs and (−)M-NTs). The average length and aspect ratio of NTs are in the ranges of 90-100 nm and 1.75-1.90, respectively, similar to the previous report,[40] which demonstrated the twisting angle of about 60º in the twisted morphology of the NTs. Since the size of NPs increased to almost 100 nm, the non-negligible effect of scattering appeared in the absorption spectra (Figure 5-6a). While no apparent difference was found in the extinction profile between (+)P- and (−)M-NTs, the NTs displayed mirror-image CD spectra in the visible region, supporting the preservation of crystallographic chirality (Figure 5-6b). The chirally twisted morphology modified the CD profile over 500 nm in a certain degree.
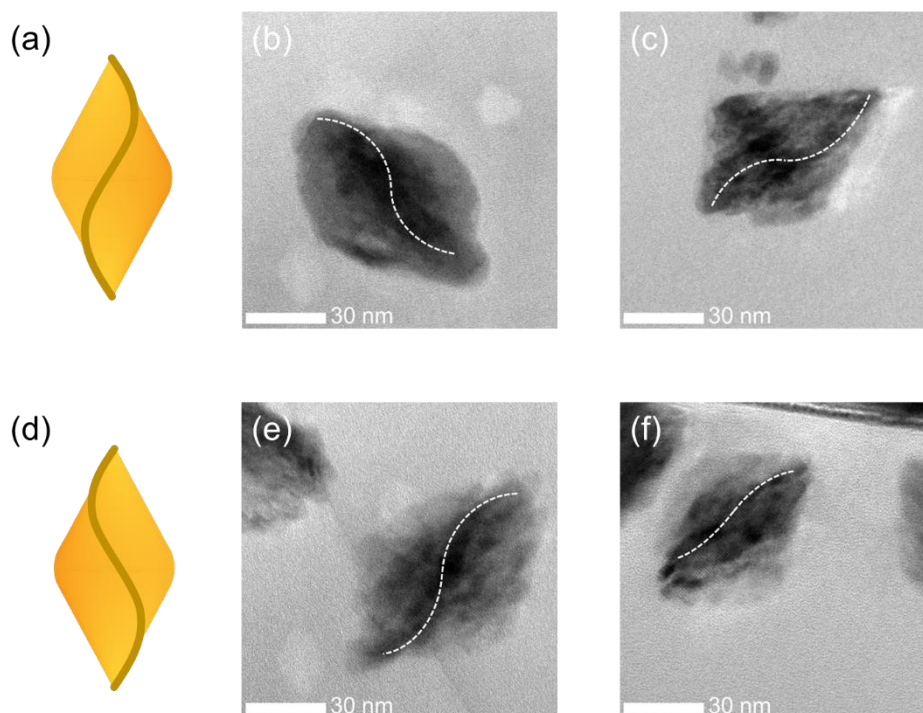
Figure 5-5. Schematic models (a) (+)P-NT and (d) (−)M-NT and TEM images (b) (+)P-NT@D-Pen, (c) (+)P-NT@**1**, (e) (−)M-NT@L-Pen, and (f) (−)M-NT@**1**.
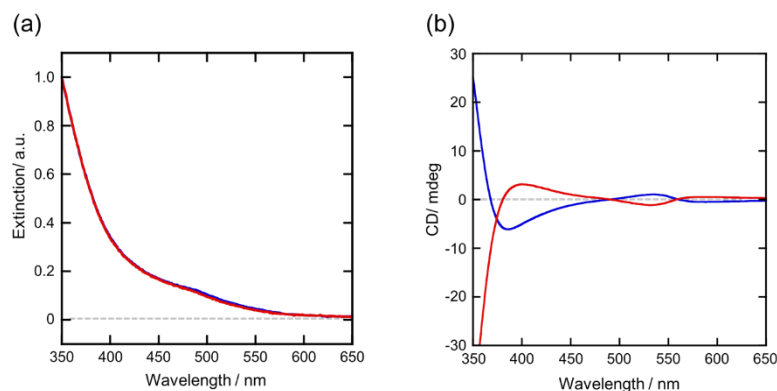

Figure 5-6. (a) Extinction and (b) CD spectra of (blue) (+)P-NTs@D-Pen and (red) (−)M-NTs@L-Pen.

To modify the NTs with compound **1**, the aqueous solution of NTs was subjected to ligand exchange by the mixture of oleylamine (OAm) and **1** through a biphasic phase transfer procedure.[39,47] The mixture solution of OAm and **1** in toluene was added to the aqueous dispersion of NTs followed by vigorous shaking over 2 hours (Chapter 5-8). After the ligand exchange process, the NTs (NTs@**1**) were stably dispersible in DMF rather than in lower-polar solvents such as toluene and chloroform, suggesting that a certain amount of residual hydrophilic ligands remained on the surface. The ligand

exchange was evaluated with attenuated total reflection Fourier transform infrared (ATR-FTIR) study (Figure 5-7). The (+)P-NTs were purified by repetitive dispersion/reprecipitation cycles to remove unbound ligands. The phosphoric (P(=O)OH) group of free **1** gave characteristic two peaks at 1267 and 1059 cm^{-1} corresponding to stretching modes of phosphine oxide ν(P=O) and phosphinate ν(POO$^-$), respectively.[48,49] The latter peak broadened and shifted to a lower wavenumber in (+)P-NTs@**1**, indicating that the POO$^-$ group coordinates to the NT surface. Furthermore, the disappearance of the ν(P=O) peak at around 1260 cm^{-1} suggests the bridging or chelating coordination mode, where the POO$^-$ group interacts with the surface using both oxygen atoms. Broad peaks around 1720 cm^{-1}, which could be assigned to the asymmetric stretching vibration mode of carboxylic group ν_{as}(COOH) may indicate the presence of residual D-Pen ligands.[50,51]
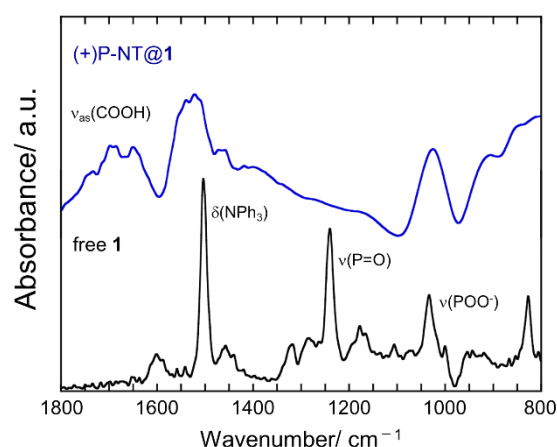

Figure 5-7. ATR-FTIR spectra of free **1** and (+)P-NT@**1**.

The ligand-exchange procedure had little effect on the size and shape of NTs (Figure 5-5). TEM images of (+)P- and (–)M-NTs@**1** demonstrated no obvious change in the size and shape of the NTs, confirming that the chiral morphology remained unchanged after the ligand exchange. The NT@**1** preserved the optical activity with an identical sign of the Cotton effect over 450 nm to the corresponding NTs before the ligand exchange, thus demonstrating the preservation of the crystallographic chirality in the NT core (Figure 5-8).

The successful modification with **1** was further supported by UV-vis extinction and emission spectra. The ligand-exchanged NTs gave an increase in the absorbance below 450 nm compared to the Pen-capped NTs (Figure 5-9). Both the (+)P- and (–)M-NTs@**1** exhibited yellow-green emission with maxima at 524 nm (Figure 5-10a) which slightly red-shifted compared to that of free **1** (at 511 nm). The excitation spectra of the NTs@**1** monitored at 525 nm were identical with that of free **1** (Figure 5-10b), indicating that the observed emission stems from capped **1** and that excitonic energy transfer from the HgS NT core did not take place.
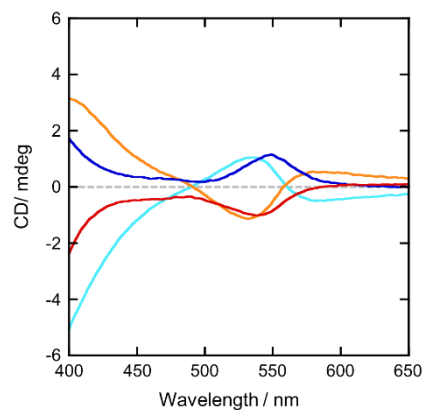
Figure 5-8. CD spectra of (+)P-NT@D-Pen (cyan), (−)M-NT@L-Pen (orange), (+)P-NT@**1** (blue), and (f) (−)M-NT@**1** (red).
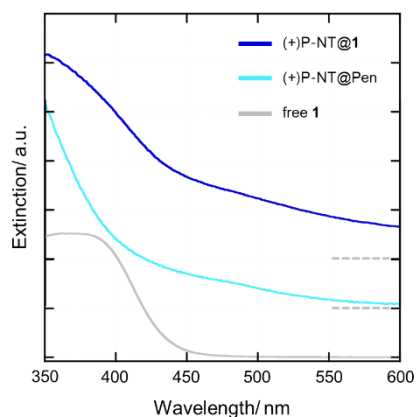

Figure 5-9. Extinction spectra of free **1**, (+)P-NT@Pen, and (+)P-NT@**1**.
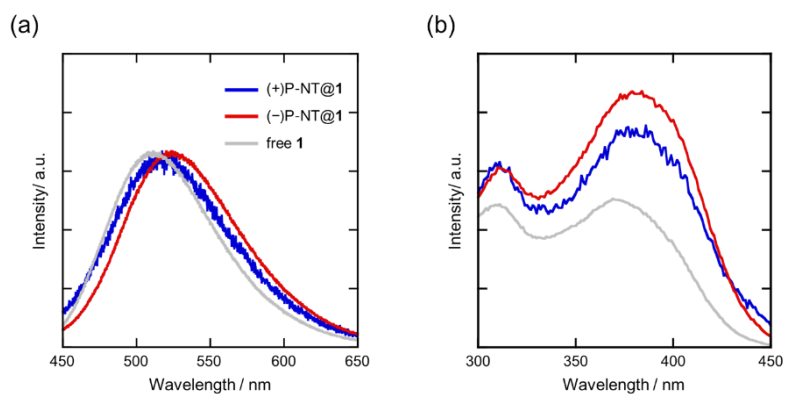

Figure 5-10. Emission (a) and excitation spectra (b) of free **1** (grey), (+)P-NT@**1** (blue), and (−)M-NT@**1** (red) in DMF.

5-4. Induced CPL of achiral 1 ligand on the surface of chiral α-HgS NTs.

Interestingly, the (+)P- and (−)M-NTs@**1** exhibited intense circularly polarized emission around fluorescence maxima (Figure 5-11). Positive and negative CPL signals were recorded for the (+)P- and (−)M-NTs@**1**, respectively, while no CPL signal was detected for free **1**. The degree of CPL can be evaluated by luminescence dissymmetry factor (g_{lum}), which is defined as $g_{lum} = 2(I_L − I_R)/(I_L + I_R)$, where I_L and I_R are the intensities of left- and right-handed circularly polarized emission, respectively. The $|g_{lum}|$ values at the peak wavelength were about 0.004 for both NTs@**1**. The apparent CPL signals suggested two possibilities as a mechanism for the chiral induction including conformational chirality and chiral arrangement of **1**. Compound **1** having two bulky triphenylamine moieties connected at the 2- and 3-positions of the benzophosphole-based ring could adopt chiral conformations with axial chirality (Figure 5-12). The enantiomeric interaction on the surface of intrinsically chiral HgS surface might induce such the conformational chirality. However, the compound **1** was expected to interact with the surface of NTs only via the phosphoric moiety. The single point interaction might not be enough to introduce chirality in the structure of **1**. Meanwhile, the chiral surface could also serve as a platform for the chiral assembly of **1**, leading to CPL generation based on intermolecular exciton coupling. [52]

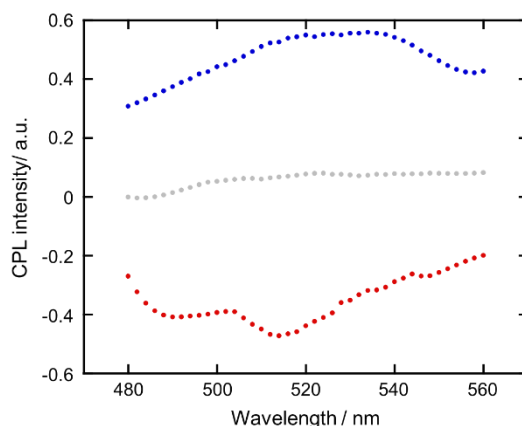**Figure 5-11.** CPL spectra of free **1** (grey), (+)P-NT@**1** (blue), and (−)M-NT@**1** (red) in DMF.

left-handed conformation   right-handed conformation
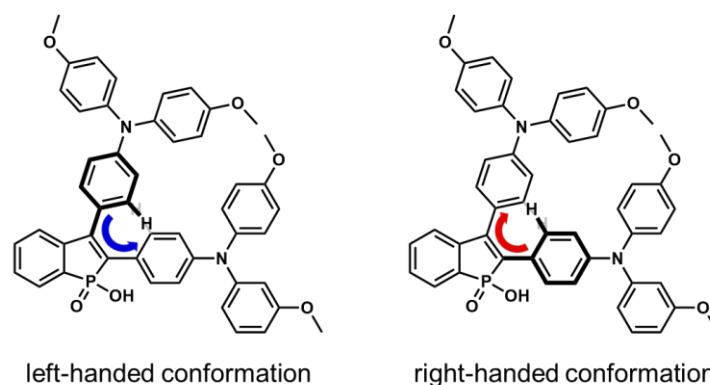
Figure 5-12. Left-handed and right-handed conformations of **1** molecule with axial chirality.

5-5. Mechanism of induced CPL of α-HgS NTs@1.

To get an insight into the chirality induction mechanism, I also modified the HgS NEs with the achiral morphology by **1**. UV-vis absorption, emission and excitation spectra after the ligand exchange confirmed the successful modification of **1** on the surface of NEs in a similar manner to the NTs@**1** (Figure 5-13). The preservation of crystallographic chirality was also identified by the CD spectra (Figure 5-14). The size and shape of NEs were also maintained as confirmed by TEM measurements (Figure 5-15). However, no effective CPL signal could be recorded for the NEs@**1** (Figure 5-16). The effective chirality could not be induced either in the conformation or ordering of **1** on the chiral surface of HgS NEs. The absence of chirality induction was also verified by using α-HgS nanorods (NRs) with an achiral morphology (Figure 5-16, 17, 18, 19). Those control experiments thus conclude that the crystallographic chirality has little effect on the chirality induction of **1**. The results of these experiments also indicate the role of chiral morphology in the chiral arrangement of **1** on the surface of NTs.
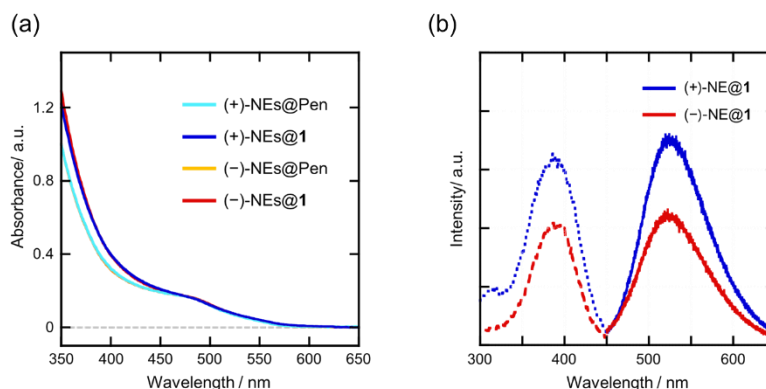
Figure 5-13. (a) UV-vis spectra of (+)-NEs and (−)-NEs capped with Pen and **1**. (b) Excitation (dashed line) and emission (solid line) spectra of (+)-NEs and (−)-NEs capped with **1**.

Figure 5-14. CD spectra of (+)-NEs@Pen (cyan), (−)-NEs@Pen (orange), (+)-NEs@**1** (blue), and (−)-NEs@**1** (red).

Figure 5-15. Typical TEM images of (+)-NEs@**1** (a) and (−)-NEs@**1** (b), respectively, together with their size distribution.
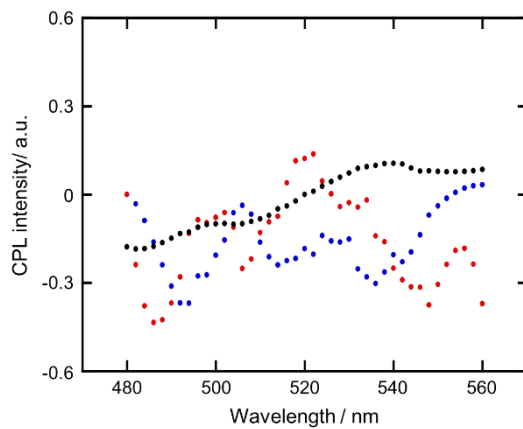
Figure 5-16. CPL spectra of (+)-NEs@**1** (blue), (−)-NEs@**1** (red), and (+)-NRs@**1** (black).

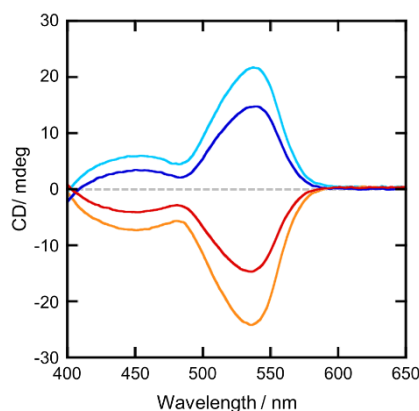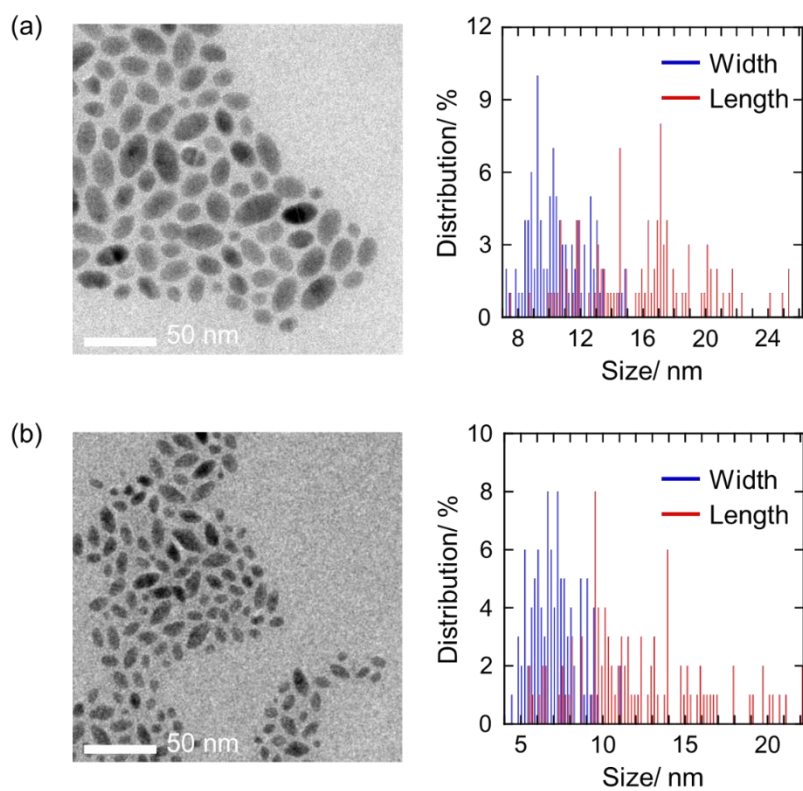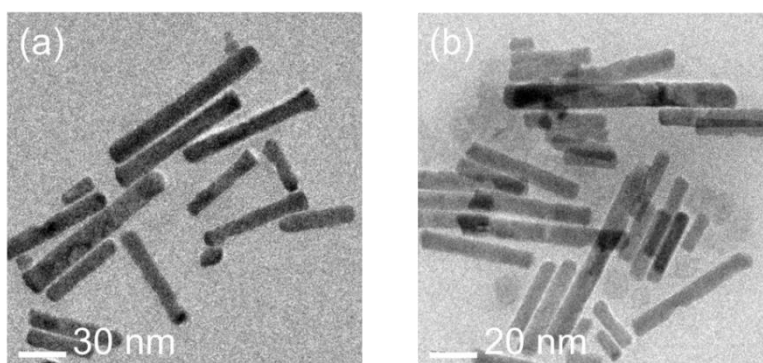**Figure 5-17**. TEM images of α-HgS NRs capped with (a) D-Pen and (b) **1**.
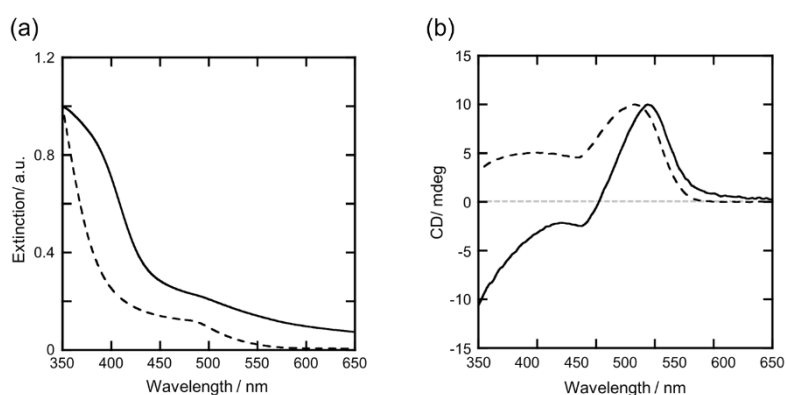
Figure 5-18. (a) UV-vis absorption and (b) CD spectra of NRs@Pen (dashed line) and NRs@**1** (solid line).
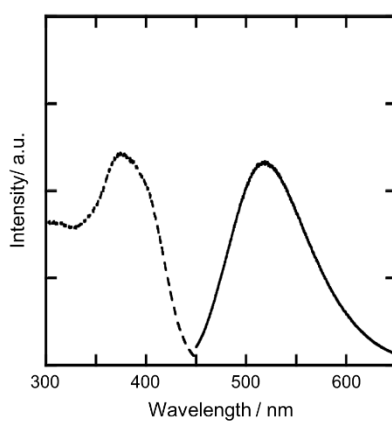
Figure 5-19. Excitation (dashed line) and emission (solid line) spectra of NRs@**1.**

The crystallographic chirality and twisting direction in the morphology could be independently controlled.[40,52] I therefore synthesized NTs with cross-structures using a combination of opposite enantiomeric Pen ligands in the seed preparation and growth stages. The (+)-NEs prepared with D-Pen were used as a seed for the growth of M-NTs in the presence

of L-Pen for the synthesis of (+)M-NTs, and vice versa for (–)P-NTs. Each NTs exhibited a CD profile with the sign of Cotton effect over 500 nm identical to the original NEs (Figure 5-20), indicating the preserved crystallographic handedness of HgS seed after the epitaxial growth. TEM images of the NTs revealed that M- and P-twisted morphologies were grown on the (+)- and (–)-NE seeds with an average length of 60-70 nm (Figure 5-21). The ligand exchange procedure with the mixture of OAm/**1** afforded (+)M- and (–)P-NTs@**1** dispersed in DMF with yellow-green emission (Figure 5-22). Spectroscopic characteristics of those NTs were similar to that of (+)P- and (–)M-NTs@**1** (Figure 5-20, 22, 23), also suggesting the successful preparation of **1**-modified (+)M-NTs and (–)P-NTs. The CD spectral profiles over 450 nm are mostly preserved for (+)M- and (–)P-NTs@**1** after the ligand exchange, indicating the unchanged crystallographic chirality of the NTs. As shown in Figure 5-24, the NTs@**1** displayed circularly polarized emission signals with amplitudes comparable to those of NTs with other chirality combinations ($|g_{lum}| \sim 0.004$). A negative CPL signal was observed for the (+)M-NTs@**1**, whereas a positive one was recorded for the (−)P-NTs@**1**. Considering this result together with that of (+)P- and (−)M-NTs@**1**, it should be noted that the sign of CPL signal can be regulated not by the crystallographic chirality but the morphological chirality of the twisted bipyramid NTs (Figure 5-25). The scale of curvature provided by the surface of NTs might be too small to have an impact on the unimolecular conformation of **1**, inducing the conformational chirality. The chirality is therefore considered to be induced in the arrangement of compound **1** on the chirally curved surface.
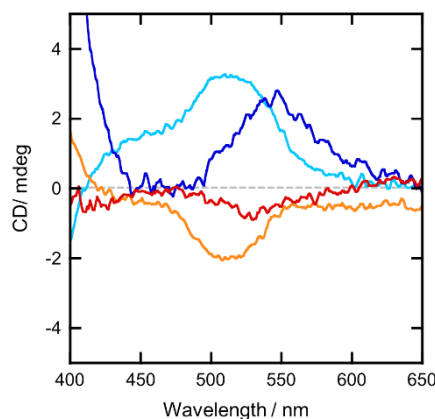
Figure 5-20. CD spectra of (+)M-NTs@Pen (cyan), (−)P-NTs@Pen (orange), (+)M-NTs@**1** (blue), (−)P-NTs@**1** (red) .
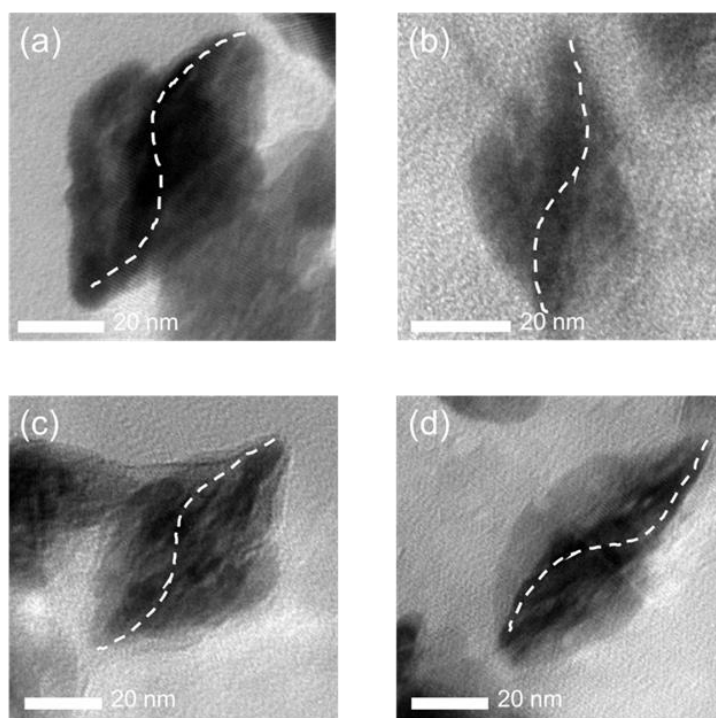
Figure 5-21. TEM images of (a) (+)M-NTs@Pen, (b) (−)P-NTs@Pen, (c) (+)M-NTs@**1**, (d) (−)P-NTs@**1**.
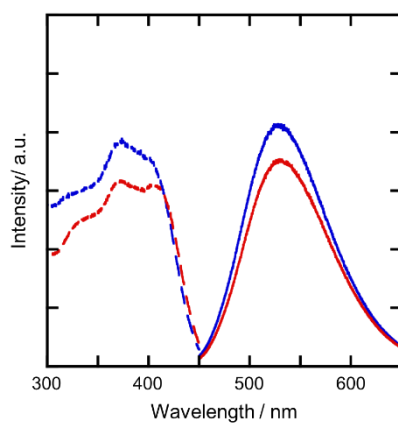
Figure 5-22. Excitation (dashed line) and emission (solid line) spectra of (+)M-NTs@**1** (blue) and (−)P-NTs@**1** (red).
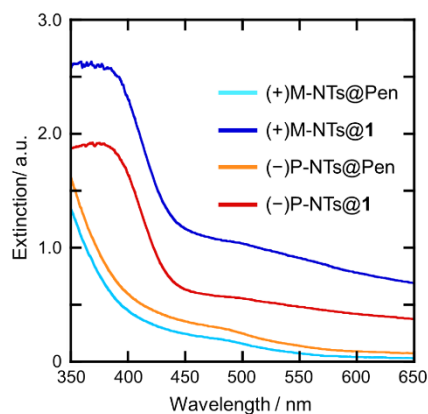
Figure 5-23. Extinction spectra of (+)M-NTs@Pen (cyan), (−)P-NTs@Pen (orange), (+)M-NTs@**1** (blue) and (−)P-NTs@**1** (red).
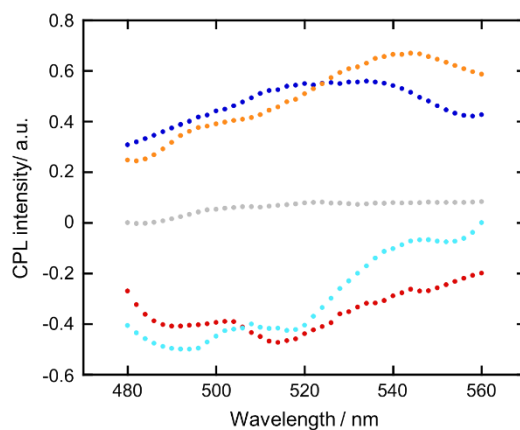
Figure 5-24. CPL spectra of free **1** (grey), (+)P-NT@**1** (blue), (–)M-NT@**1** (red), (+)M-NT@**1** (cyan), and (–)P-NT@**1** (orange).
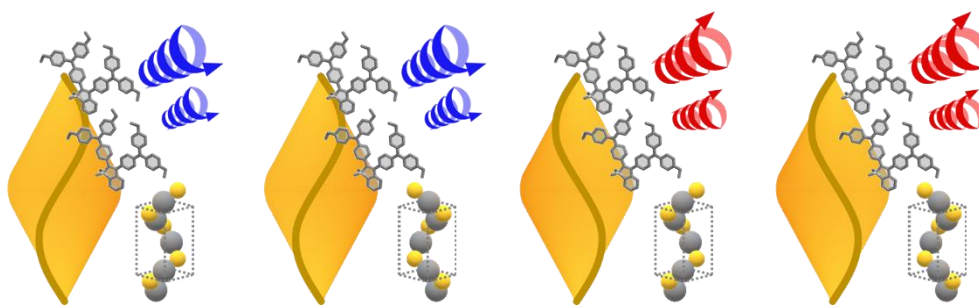
Figure 5-25. Illustration of induced CPL of **1** on the surface of chiral α-HgS NTs

5-6. Conclusions.

In conclusion, I developed a new approach to generate CPL-active materials system composed of a chiral inorganic nanoparticle and achiral fluorescent ligands. The achiral

molecule **1** adsorbed on the surface of α-HgS NTs exhibited noticeable CPL signals depending on the morphological chirality of NTs. The α-HgS NTs could possess the both handedness in the crystalline lattice and nanoparticle morphology. The present work demonstrated the latter played a key role in the chirality transfer from the curved surface of NTs to the arrangement of achiral **1**. Further design of organic luminescent molecules with appropriate coordinating groups would demonstrate the utility of the present chiral-inorganic and organic hybrid system as a versatile CPL generation system.

5-7. Experimental; Synthesis and characterization.

General. **1** was synthesized according to the reaction procedures as showed in Scheme 1. Their chemical structures were confirmed by high-resolution mass spectroscopy (Varian MAT 311 or ZabSpec TOF Micromass instrument), and ^{1}H, ^{13}C, and ^{31}P NMR spectra (Bruker AV 300 and AV III 400 MHz NMR spectrometers equipped with BBO or BBFO probe heads). Absorption spectra in solution were studied with a JASCO V-760 spectrophotometer. Fluorescence spectra were measured with a spectrofluorometer (Hitachi F7000). CD spectra were recorded by a JASCO J-725 spectropolarimeter. An absolute photocyclization quantum yield of **1** was determined by a Shimazu QYM-01 setup. TEM observation was conducted with a JEOL JEM-2200FS electron microscope. Specimens for TEM were prepared by drop-casting of solutions of NEs or NTs onto carbon-coated copper grids. XRD profiles were recorded using a RigakuSmartLab9kW/IP/HY/N X-ray diffractometer. ATR-IR measurements were performed using a JASCO FT/IR-4000 equipped with a JASCO ATR-PRO ONE. CPL spectra were measured using a home-made CPL spectroscopy system.
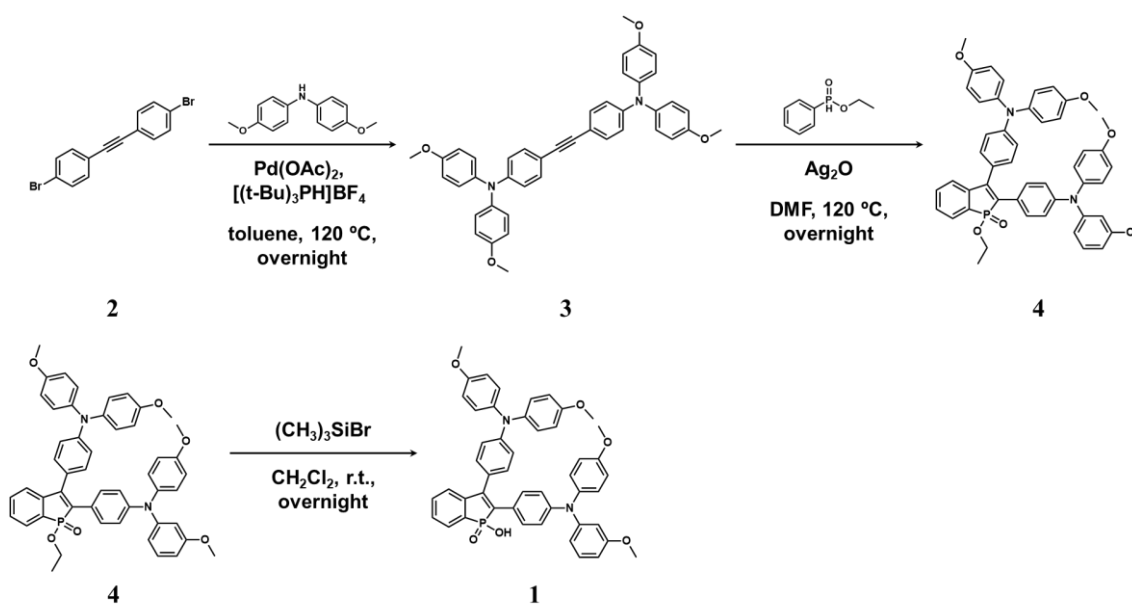
Scheme 1. Synthetic scheme of **1**

Synthesis of 4,4'-(ethyne-1,2-diyl)bis(*N,N*-bis(4-methoxyphenyl)aniline) (3). (1,2-Bis(4-bromophenyl)ethyne (600 mg, 1.79 mmol), bis(4-methoxyphenyl)amine (900 mg, 3.93 mmol), tBuOK(1.2 g, 10.7 mmol), palladium acetate (II) (40 mg, 0.18 mmol) and tri-*tert*-butylphosphonium tetrafluoroborate (150 mg, 0.5 mmol) were added into a Schlenk and three Argon-vacuum cycles were performed. Then, the Schlenk was filled up with 40 mL of degassed toluene. Subsequently, the mixture was heated to 120 ºC overnight, and, then, cooled to room temperature (r.t.). After removing the solvent under vacuum, the mixture was partitioned between CH₂Cl₂ and water. The combined organic layers were washed with brine, dried over Mg₂SO₄, the solvent was evaporated, and the crude purified by

column chromatography on silica gel (eluent: CH_2Cl_2/Pentane = 1/1), affording a yellow solid in 94% yield (1.06 g). ^{1}H NMR (400 MHz, CD_2Cl_2) δ 7.25 (d, J(H,H) = 8.8 Hz, 4H), 7.06 (d, J(H,H) = 8.8 Hz, 8H), 6.85 (d, J(H,H) = 8.9 Hz, 8H), 6.80 (d, J(H,H) = 8.8 Hz, 4H), 3.78 (s, 12H). ^{1}H NMR data fit with previously reported procedure.

Synthesis of 2,3-bis(4-(bis(4-methoxyphenyl)amino)phenyl)-1-ethoxy-1H-phosphindole 1-oxide (4). A mixture of **3** (500 mg, 0.79 mmol), ethyl phenylphosphinate (268 mg, 1.58 mmol), and Ag_2O (366 mg, 1.58 mmol) in 20 mL DMF was stirred at 120 ºC under Ar overnight. After cooling to r.t., the mixture was diluted with ethyl acetate (30 mL) and the insoluble solids were removed on a Celite plug. The filtrate was transferred in a round bottom flask and 2 mL of hydrogen peroxide were added and the solution was stirred for 30 minutes. The solution was washed with water and brine and dried over anhydrous Mg_2SO_4. After filtration, the solvent was evaporated under reduced pressure, and the residue was purified by column chromatography on silica gel by using CH_2Cl_2/ethyl acetate (95/5 v/v) as eluent to afford **4** as an orange solid (m = 196 mg, yield = 31%). ^{1}H NMR (300 MHz, CD_2Cl_2) δ 7.66 (dd, J(H,H)= 10.3, 7.1 Hz, 1H), 7.45 – 7.36 (m, 2H), 7.24 – 7.18 (m, 3H), 7.14 – 7.00 (m, 10H), 6.94 – 6.78 (m, 10H), 6.72 (d, J(H,H) = 8.7 Hz, 2H), 4.06 – 3.93 (m, 2H), 3.79 (s, 12H), 1.24 (t, J(H,H) = 7.1 Hz, 3H). ^{13}C NMR (101 MHz, CD2Cl2) δ 157.0 (Cq), 156.9 (Cq), 149.6 (Cq), 149.0 (Cq), 146.6 (d, J(C-P) = 28 Hz, Cq(β)), 143.5 (d, J(C-P) = 34 Hz, Cq(β)), 140.9 (Cq), 140.7 (Cq), 133.4 (d, J(C-P) = 2 Hz, CH), 130.3 (s, CH), 130.2 (d, J(C-P) = 7 Hz, CH), 128.9 (d, J(C-P) = 105 Hz, Cq(α)), 128.8 (d, J(C-P) = 11 Hz, CH), 128.0 (s, CH), 127.8 (s, CH), 127.7 (s, CH), 127.6 (d, J(C-P) = 115 Hz, Cq(α)), 126.0 (d, J(C-P) = 18 Hz, Cq), 124.6 (d, J(C-P) = 10 Hz, Cq), 124.0 (d, J(C-P) = 13 Hz, CH), 119.9 (s, CH), 119.1 (s, CH), 115.3 (s, CH), 115.2 (s, CH), 62.5 (d, J(C-P) = 6 Hz, OCH2), 56.0 (s, OCH3), 16.9 (d, J(C-P) = 6 Hz, CH3). ^{31}P NMR (162 MHz, CD_2Cl_2) δ +46.0 (s). HRMS (ESI, CH_2Cl_2): $[M]^+(C_{50}H_{45}N_2O_6P)$, m/z Calcd for: 800.3015, m/z Found: 800.3004.

Synthesis of 2,3-bis(4-(bis(4-methoxyphenyl)amino)phenyl)-1-hydroxy-1H-phosphindole 1-oxide (1) **4** (80 mg, 0.1 mmol) was dissolved in 10 mL of CH_2Cl_2 under Argon. Then bromotrimethylsilane (151 mg, 0.98 mmol) was added and the solution turned deep red. The solution was stirred at r.t. overnight. Then 10% HCl was added (20 mL) and the mixture was stirred 15 minutes. The solution was extracted with CH_2Cl_2 and dried over anhydrous Mg_2SO_4. After filtration, the solvent was evaporated, and the residue was purified by recrystallization in toluene/heptane to afford red solid (m = 75 mg, Yield = 97%). ^{1}H NMR (400 MHz, DMSO) δ 7.61 – 7.53 (m, 1H), 7.46 – 7.38 (m, 1H), 7.38 – 7.31 (m, 1H), 7.19 (d, J(H,H) = 8.5 Hz, 2H), 7.08 (d, J(H,H) = 8.9 Hz, 4H), 7.05 – 6.97 (m, 7H), 6.91 (d, J(H,H) = 8.7 Hz, 8H), 6.80 (d, J(H,H) = 8.7 Hz, 2H), 6.59 (d, J(H,H) = 8.7 Hz, 2H), 3.74 (s, 12H). ^{31}P NMR (162 MHz, DMSO) δ +39.10 (s). Due to solubility issues, no ^{13}C NMR spectra could be recorded. HRMS (ESI, CH_2Cl_2): $[M-H]^-(C_{48}H_{40}N_2O_6P)$, m/z Calcd for: 771.26240, m/z Found: 771.2632.
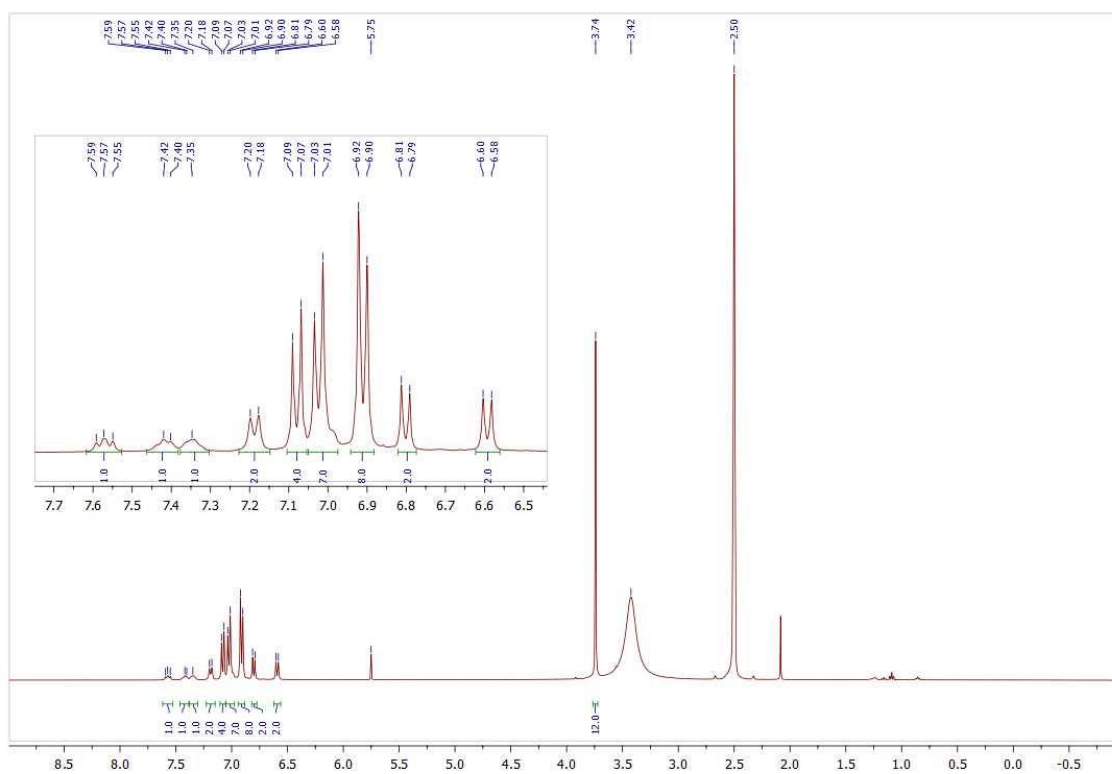
Synthesis of α-HgS NEs. 39.2 mg $Hg(NO_3)_2 \cdot nH_2O$ was dissolved in 3.9 ml of water, followed

by addition of 0.9 ml of D- or L-penicillamine aqueous solution (100 mM) under stirring to get a colorless solution. An aqueous 100 mM NaOH solution was added to adjust the pH value to *ca.* 11.5. After further stirring for 3 min, 0.9 ml of thioacetamide solution (100 mM) was injected quickly and the mixture was stirred for 24 h at room temperature for the synthesis of α-HgS NEs. The NEs was precipitated by the addition of acetone. The precipitate was redispersed in a minimum volume of water and then precipitated using acetone. This procedure was repeated at three times to remove unreacted species.

Synthesis of α-HgS NTs. Initially, A 100 mM thioacetamide stock solution was prepared by dissolving 60 mg of thioacetamide in 8.0 ml of water. A mercury stock solution was prepared by dispersing 41.3 mg of $Hg(NO_3)_2 \cdot nH_2O$ in 4.0 ml of water. Then, 1.1 ml of D- or L-Pen solution (100 mM) and 0.3 ml of NaOH (1 M) were added in sequent. In a three-neck round bottom flask, 0.25 ml of D- or L-NEs colloidal solution was diluted with 2.25 ml of water under N_2 atmosphere. Then, 0.3 ml of NaOH solution (1.0 M) was added, and 0.9 ml of D- or L-Pen solution (100 mM) were added to the D- or L-NEs solution respectively. The 1.1 ml of thioacetamide stock solution and 4.0 ml of mercury stock solution containing D- or L-Pen were co-injected into the D- or L-NEs solution, respectively, for 2 h at room temperature. The reaction solution was stirred overnight and mixed with acetone, followed by centrifugation at 5 000 rpm for 5 min. The precipitate was redispersed in a minimum volume of water and then precipitated using acetone. This procedure was repeated at three times to remove unreacted species.

Ligand exchange from water-soluble Pen ligands to the mixture of 1 and OAm. In a 2-ml glass vial, 0.3 ml of an aqueous solution of α-HgS NTs or NEs was mixed with 1.5 mg of **1** in 0.05 ml of toluene and 0.05 ml of OAm. The mixture was stirred vigorously for 2 h at room temperature. After the reaction, the two phases appeared by addition of 0.3 ml of water and toluene. The organic phase was carefully collected and mixed with methanol, followed by centrifugation at 5 000 rpm for 5 min. The particles were washed with methanol after re-dispersed in a drop of *N,N*-dimethylformamide. The washing step was repeated several times.

¹H-NMR spectrum of **4**

³¹P-NMR spectrum of **4**

Figure 5-26. ¹H-NMR (CD₂Cl₂, 300 MHz) and ³¹P-NMR (CD₂Cl₂, 162 MHz) spectra of **4**

¹H-NMR spectrum of **1**
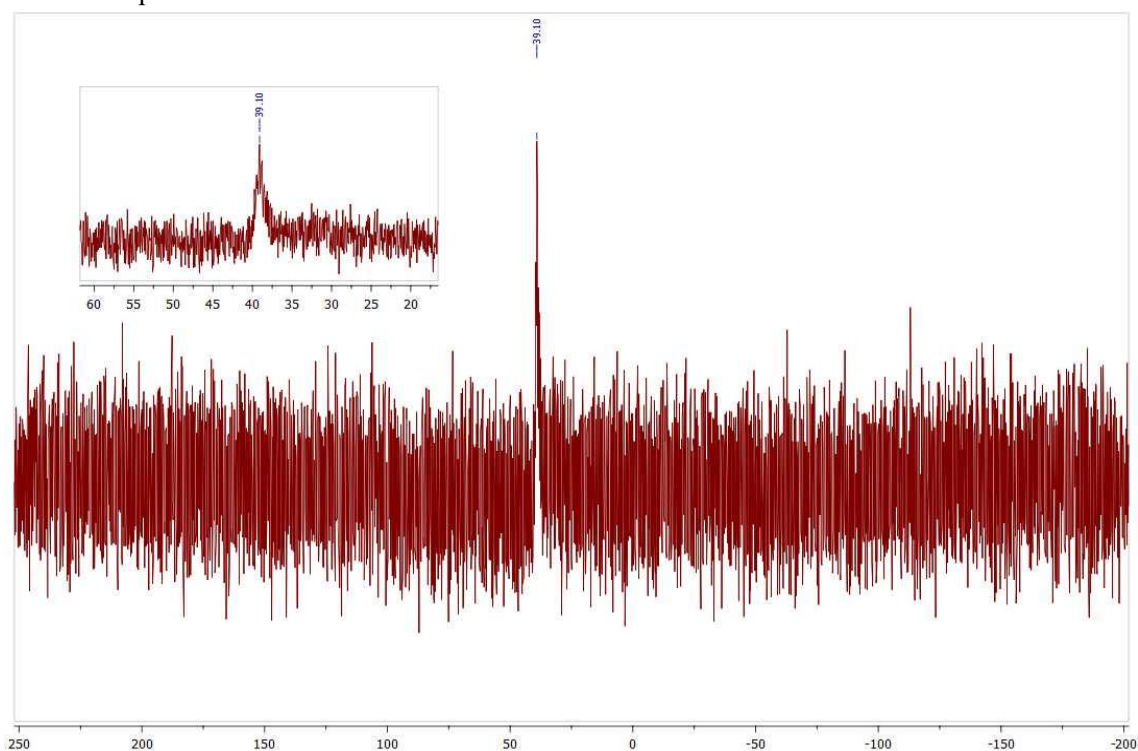

³¹P-NMR spectrum of **1**

Figure 5-27. ¹H-NMR (DMSO, 400 MHz) and ³¹P-NMR (DMSO, 162 MHz) spectra of **1**.

5-8. References.

1 F. Zinna, U. Giovanella, L. D. Bari, Highly Circularly Polarized Electroluminescence from a Chiral Europium Complex, *Adv. Mater.* **2015**, 27, 1791−1795

2 F. Song, Z. Xu, Q. Zhang, Z. Zhao, H. Zhang, W. Zhao, Z. Qiu, C. Qi, H. Zhang, H. H. Y. Sugn, lan D. Williams, J. W. Y. Lam, Z. Zhao, A. Qin, D. Ma, B. Z. Tang, Highly Efficient Circularly Polarized Electroluminescence from Aggregation-Induced Emission Luminogens with Amplified Chirality and Delayed Fluorescence, *Adv. Funct. Mater.* **2018**, 18, 1800051.

3 T. Imagawa, S. Hirata, K. Totani, T. Watanabe, M. Vacha, Thermally activated delayed fluorescence with circularly polarized luminescence characteristics, *Chem. Commun.* **2015**, 51, 13268−13271.

4 N. Sharma, S. Spuling, C. M. Mattern, W. Li, O. Fuhr, Y. Tsuchiya, S. Bräse, I. D. W. Samuel, E. Zysman-Colman, Turn on of sky-blue thermally activated delayed fluorescence and circularly polarized luminescence (CPL) via increased torsion by a bulky carbazolophane donor, *Chem. Sci.* **2019**, 10, 6689−6696.

5 Y. Kim, B. Yeom, O. Arteaga, S. Jo Yoo, S. G. Lee, J. G. Kim, N. A. Kotov, Reconfigurable chiroptical nanocomposites with chirality transfer from the macro- to the nanoscale, *Nature Mater.* **2016**, 15, 461−468.

6 Y. Yang, R. C. da Costa, M. J. Fuchter, A. J. Campbell, Circularly polarized light detection by a chiral organic semiconductor transistor, *Nat. Photon.* **2013**, 7, 634−638.

7 C. Chen, L. Gao, W. Gao, C. Ge, X. Du, Z. Li, Y. Yang, G. Niu, J. Tang, Circularly polarized light detection using chiral hybrid perovskite, *Nat. Commun.* **2019**, 10, 1927−1934.

8 E. M. Sánchez-Carnerero, A. R. Agarrabeitia, F. Moreno, B. L. Maroto, G. Muller, M. J. Ortiz, S. de la Moya, Circularly Polarized Luminescence from Simple Organic Molecules, *Chem. Eur. J.* **2015**, 21, 13488–13500.

9 N. Chen, B. Yan, Recent Theoretical and Experimental Progress in Circularly Polarized Luminescence of Small Organic Molecules, *Molecules*, **2018**, 23, 3376.

10 H. Tanaka, Y. Inoue, T. Mori, Circularly Polarized Luminescence and Circular Dichroisms in Small Organic Molecules: Correlation between Excitation and Emission Dissymmetry Factors, *ChemPhotoChem*, **2018**, 2, 386−402.

11 B. M. Langeveld-Voss, R. A. J. Janssen, M. P. T. Christiaans, S. C. J. Meskers, H. P. J. M. Dekkers, E. W. Meijer, Circular Dichroism and Circular Polarization of Photoluminescence of Highly Ordered Poly{3,4-di[(S)-2-methylbutoxy]thiophene}, *J. Am. Chem. Soc.* **1996**, 118, 4908−4909.

12 E. Peeters, M. P. T. Christiaans, R. A. J. Janssen, H. F. M. Schoo, H. P. J. M. Dekkers, E. W. Meijer, Circularly Polarized Electroluminescence from a Polymer Light-Emitting Diode, *J. Am. Chem. Soc.* **1997**, 119, 9909−9910.

13 T. Shiraki, Y. Tsuchiya, T. Noguchi, S. Tamaru, N. Suzuki, M. Taguchi, M. Fujiki, S. Shinkai,

Creation of Circularly Polarized Luminescence from an Achiral Polyfluorene Derivative through Complexation with Helix-Forming Polysaccharides: Importance of the meta-Linkage Chain for Helix Formation, *Chem. Asian J.* **2014**, 9, 218−222.

14   F. Zinna, L. D. Bari, Lanthanide Circularly Polarized Luminescence: Bases and Applications, *Chirality* **2015**, 27, 1−13.

15   Y. Kitagawa, M. Tsurui, Y. Hasegawa, Steric and Electronic Control of Chiral Eu(III) Complexes for Effective Circularly Polarized Luminescence, *ACS Omega* **2020**, 5, 3786−3791.

16   J. Kumar, T. Nakashima, T. Kawai, Circularly Polarized Luminescence in Chiral Molecules and Supramolecular Assemblies, *J. Phys. Chem. Lett.* **2015**, 6, 3445−3452.

17   Z. Shen, T. Wang, L. Shi, Z. Tang, M. Liu, Strong circularly polarized luminescence from the supramolecular gels of an achiral gelator: tunable intensity and handedness, *Chem. Sci.* **2015**, 6, 4267−4272.

18   H. Li, B. S. Li, B. Z. Tang, Molecular Design, Circularly Polarized Luminescence, and Helical Self-Assembly of Chiral Aggregation-Induced Emission Molecules, *Chem. Asian J*. **2019**, 14, 674−688.

19   T. Mori*, Circularly Polarized Luminescence of Isolated Small Organic Molecules*, Springer: Singapore, **2020**.

20   H. G. Brittain, Excited-state optical activity of a cyclodextrin inclusion compound, *Chem. Phys. Lett.* **1981**, 83, 161−164.

21   S. Haraguchi, M. Numata, C. Li, Y. Nakano, M. Fujiki, S. Shinkai, Circularly Polarized Luminescence from Supramolecular Chiral Complexes of Achiral Conjugated Polymers and a Neutral Polysaccharide, *Chem. Lett*. **2009**, 38, 254−255.

22   N. Inoue, K. Hayashi, Y. Yonenaga, T. Itoiuu, K. Fumimoto, T. Uchida, M. Iwamura, K. Nozaki, A Doubly Alkynylpyrene-Threaded [4]Rotaxane That Exhibits Strong Circularly Polarized Luminescence from the Spatially Restricted Excimer, *Angew. Chem., Int. Ed.* **2014**, 53, 14392−14396.

23   T. Goto, Y. Okazaki, M. Ueki, Y. Kuwahara, M. Takafuji, R. Oda, H. Ihara, Induction of Strong and Tunable Circularly Polarized Luminescence of Nonchiral, Nonmetal, Low-Molecular-Weight Fluorophores Using Chiral Nanotemplates, *Angew. Chem., Int. Ed.* **2017**, 56, 2989−2993.

24   J. Han, J. You, X. Li, P. Duan, M. Liu, Full-Color Tunable Circularly Polarized Luminescent Nanoassemblies of Achiral AIEgens in Confined Chiral Nanotubes, *Adv. Mater.* **2017**, 29, 1606503.

25   Y. Sang, J. Han, T. Zhao, P. Duan, M. Liu, Circularly Polarized Luminescence in Nanoassemblies: Generation, Amplification, and Application, *Adv. Mater.* **2019**, 32, 1900110.

26   J. Zhang, Q. Liu, W. Wu, J. Peng, H. Zhang, F. Song, B. He, X. Wang, H. H. -Y. Sung, M. Chen, B. S. Li, S. H. Liu, J. W. Y. Lam, B. Z. Tang, Real-Time Monitoring of Hierarchical Self-

Assembly and Induction of Circularly Polarized Luminescence from Achiral Luminogens, *ACS Nano* **2019**, 13, 3618−3628.

27 S. Huo, P. Duan, T, Jiao, Q. Peng, M. Liu, Self-Assembled Luminescent Quantum Dots To Generate Full-Color and White Circularly Polarized Light, *Angew. Chem., Int. Ed.* **2017**, 56, 12174−12178.

28 X. Jin, Y. Sang, Y. Shi, Y. Li, X. Zhu, P. Duan, M. Liu, Optically Active Upconverting Nanoparticles with Induced Circularly Polarized Luminescence and Enantioselectively Triggered Photopolymerization, *ACS Nano* **2019**, 13, 2804−2811.

29 Y. Shi, P. Duan, S. Huo, Y. Li, M. Liu, Endowing Perovskite Nanocrystals with Circularly Polarized Luminescence, *Adv. Mater.* **2018**, 30, 1705011.

30 M. Sugimoto, X. -L. Liu, S. Tsunega, E. Nakajima, S. Abe, T. Nakashima, T. Kawai, R. -H. Jin, Circularly Polarized Luminescence from Inorganic Materials: Encapsulating Guest Lanthanide Oxides in Chiral Silica Hosts, *Chem. Eur. J.* **2018**, 24, 6519−6524.

31 S. Tsunega, R. -H. Jin, T. Nakashima, T. Kawai, Transfer of Chiral Information from Silica Hosts to Achiral Luminescent Guests: a Simple Approach to Accessing Circularly Polarized Luminescent System, *ChemPlusChem,* **2020**, 85, 619−626.

32 P. Liu, W. Chen, Y. Okazaki, Y. Battie, L. Brocard, M. Decossas, E. Pouget, P. Muller-Buschbaum, B. Kauffmann, S. Pathan, T. Sagawa, R. Oda, Optically Active Perovskite $CsPbBr_3$ Nanocrystals Helically Arranged on Inorganic Silica Nanohelices, *Nano Lett.* **2020**, DOI: acs.nanolett.0c02013.

33 I. Doalmic, B. Varnholt, T. Bürgi, Chirality transfer from gold nanocluster to adsorbate evidenced by vibrational circular dichroism, *Nat. Commun.* **2015**, 6, 7117.

34 C. Zheng, Y. Chen, K. Kirschbaum, K. Appavoo, M. Sfeir, R. Jin, Structural patterns at all scales in a nonmetallic chiral $Au_{133}(SR)_{52}$ nanoparticle, *Sci. Adv.* **2015**, 1, e1500045.

35 C. Zheng, Y. Chen, K. Kirschbaum, K. J. Lambright, R. Jin, Emergence of hierarchical structural complexities in nanoparticles and their assembly, *Science* **2016**, 354, 1580−1584.

36 H. Yoshida, M. Ehara, U. D. Piyakumar, T. Kawai, T. Nakashima, Enantioseparation and chiral induction in Ag_{29} nanoclusters with intrinsic chirality, *Chem. Sci.* **2020**, 11, 2394−2400.

37 X. Wei, J. Liu, G. -J. Xia, J. Deng, P. Sun, J. J. Chruma, W. Wu, C. Yang, Y. -G. Wang, Z. Huang, Enantioselective photoinduced cyclodimerization of a prochiral anthracene derivative adsorbed on helical metal nanostructures, *Nat. Chem.* **2020**, 12, 551−559.

38 A. Ben-Moshe, A. O. Govorov, G. Markovich, Enantioselective Synthesis of Intrinsically Chiral Mercury Sulfide Nanocrystals, *Angew. Chem., Int. Ed.,* 2013, **52**, 1275-1279.

39 J. Kuno, T. Kawai, T. Nakashima, The effect of surface ligands on the optical activity of mercury sulfide nanoparticles, *Nanoscale,* **2017**, 9, 11590−11595.

40 P. Wang, S. -J. Yu, A. O. Govorov, M. Ouyang, Cooperative expression of atomic chirality in inorganic nanostructures, *Nat. Commun.* **2017**, 8, 14312.

41 E. Yamaguchi, A. Fukazawa, Y. Kosaka, D. Yokogawa, S. Irle, S. Yamaguchi, A Benzophosphole P-Oxide with an Electron-Donating Group at 3-Position: Enhanced Fluorescence in Polar Solvents, *BCSJ*, **2015**, 88, 1545−1552.

42 C. Wang, A. Fukazawa, M. Taki, Y. Sato, T. Hagashiyama, S. Yamaguchi, A Phosphole Oxide Based Fluorescent Dye with Exceptional Resistance to Photobleaching: A Practical Tool for Continuous Imaging in STED Microscopy, *Angew. Chem., Int. Ed.,* **2015**, 54, 15213−15217.

43 Y. Matano, Y. Motegi, S. Kawatsu, Y. Kimura, Comparison of 2-Arylnaphtho[2,3-b]phospholes and 2-Arylbenzo[b]phospholes: Effects of 2-Aryl Groups and Fused Arene Moieties on Their Optical and Photophysical Properties, *J. Org. Chem.* **2015**, 80, 5944−5950.

44 A. Puzder, A. J. Williamson, N. Zaitseva, G. Galli, L. Manna, A. P. Alivisatos, The Effect of Organic Ligand Binding on the Growth of CdSe Nanoparticles Probed by Ab Initio Calculations, *Nano Lett*. **2004**, 4, 2361−2365.

45 J. S. Owen, J. Park, P. -E. Trudeau, A. P. Alivisatos, Reaction Chemistry and Ligand Exchange at Cadmium−Selenide Nanocrystal Surfaces, *J. Am. Chem. Soc*. **2008**, 130, 12279−12281.

46 A. Hassinen, R. Gomes, K. De Nolf, Q. Zhao, A. Vantomme, J. C. Martins, Z. Hans, Surface Chemistry of CdTe Quantum Dots Synthesized in Mixtures of Phosphonic Acids and Amines: Formation of a Mixed Ligand Shell, *J. Phys. Chem. C* **2013**, 117, 13936−13943.

47 P. Wang, S. -J. Yu, M. Ouyang, Assembled Suprastructures of Inorganic Chiral Nanocrystals and Hierarchical Chirality, *J. Am. Chem. Soc*. **2017**, 139, 6070−6073.

48 E. E. Khawaja, S. M. A. Durrani, F. F. Al-Adel, M. A. Salim, M. S. Hussain, X-ray photoelectron spectroscopy and Fourier transform-infrared studies of transition metal phosphate glasses, *J. Mater. Sci.* **1995**, 30, 225−234.

49 S. Marivel, M. R. Shimpi, V. R. Pedireddi, Novel Supramolecular Assemblies of Coordination Polymers of Zn(II) and Bis(4-nitrophenyl)phosphoric Acid with Some Aza-Donor Compounds, *Cryst. Growth Des.* **2007**, 7, 1791−1796.

50 H. Yao, N. Nishida, K. Kimura, Conformational study of chiral penicillamine ligand on optically active silver nanoclusters with IR and VCD spectroscopy, *Chem. Phys.* **2010**, 368, 28−37.

51 J. Kuno, K. Miyake, S. Katao, T. Kawai, T. Nakashima, Enhanced Enantioselectivity in the Synthesis of Mercury Sulfide Nanoparticles through Ostwald Ripening, *Chem. Mater.* **2020**, 32, 8412−8419.

52 N. Harada, K. Nakanishi, *Circular Dichroic Spectroscopy–Exciton Coupling in Organic Stereochemistry*, University Science Books, Oxford, Mill Valley, CA, **1983**.

53 U. Hananel, A. Ben-Moshe, D. Tal, G. Markovich, Enantiomeric Control of Intrinsically Chiral Nanocrystals, *Adv. Mater*. **2020**, 32, 1905594.

Chapter 6
Conclusions and Prospects

6-1. Conclusions and Future Prospects.

This thesis summarizes my attempt to control the chirality of cinnabar-based nanoparticles (α-HgS NPs) through chiral ligand coordinations. All throughout the preceding chapters, I focused on the role of the chiral ligands, especially their coordination configurations, in determining the handedness of chiral crystalline structure of the α-HgS core.

In Chapter 1, I gave an introduction to a relatively new research field of nanoscale chirality in inorganics. Since the initial preparation of gold nanoclusters using chiral ligands, [1,2] large variety of chiral inorganic nanomaterials have been emerging for only two decades, [3-6] and rapidly developed due to their significant chiral properties as discussed in Chapter 1. Nevertheless, a central question in the field of nanoscale chirality still remains unanswered: How does chirality transfer operate from chiral ligand? I assumed that difficulty in the evaluation of detailed structure of such inorganic nanomaterials is the major issue. Very recently, a new class of chiral inorganic NPs has emerged with the synthetic demonstration of intrinsically chiral α-HgS NPs, [7] which crystallize in the chiral trigonal space group. In this dissertation work, I expected that the NPs composed of α-HgS with an intrinsically chiral crystalline system could be an ideal model to discuss how the chirality of surface ligand operates on the controlled synthesis of chiral NPs and vice versa (how the chirality of the core operates on the coordination structure or arrangement of surface ligands). The employment of intrinsically chiral inorganics makes the discussion simpler since their crystallographic structures adopt either right- or left-handed chiral atomic arrangement. In 2016, when I started this dissertation research, there was only one report on the chiral α-HgS NPs, which described the enantioselective synthesis of NPs by using an enantiomeric chiral ligand. [7] Therein, it was also reported that the formation of α-HgS NPs proceeded via the transient formation of metastable β-HgS (Figure 6-1). [7]

In the intrinsically chiral nanomaterial systems, chiral surface can be displayed at low Miller index surface. These nanomaterials have attracted much interest as a chiral source for asymmetric catalyst, affording enantioselective processes. Nevertheless, there are few studies on the chirality transfer from inorganic nanomaterials to adsorbed molecules on their surface. [10,11]
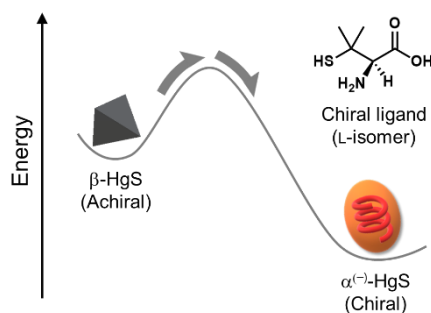

Figure 6-1. Schematic illustration of enantioselective synthesis of chiral α-HgS NPs.

This thesis aims to (1) reveal the mechanism on the translation of ligand chirality to HgS NPs, and (2) challenge the chirality transfer from chiral α-HgS NPs to surface ligand molecules.

In Chapter 2, the presence of chiral thiol ligands successfully led to the chiral cinnabar phase in the aqueous synthesis of mercury sulfide NPs, with large dissymmetry factors in their optical activity. A slight modification in the chemical structure of chiral ligands with an identical stereochemistry (L-form) resulted in the reversal of chirality in the HgS core. This finding suggests that the chirality of the HgS core can be dictated by the delicate balance of the (quasi-) enantiomeric coordination modes of ligands on the semiconductor surface. The chiral crystalline structure of semiconductor cores was successfully preserved after the ligand-exchange by an achiral ligand (chiral memory), keeping more than half of the dissymmetry factors. The chiral crystalline phase was robust enough to be preserved even at high temperature (100 ºC) in the absence of the chiral ligand. This study on the chiral memory effect shed light on chirality transfer from the α-HgS NP to an achiral molecule adsorbed on its surface (Chapter 5).

In Chapter 3, I have demonstrated the inversion of optical activity in the synthesis of HgS NPs with an identical capping ligand. The HgS NPs with *N*-acetyl-L-cysteine (Ac-L-Cys) underwent a continuous decrease in CD intensity followed by a reversal in CD pattern upon heating at 80 ºC. The modulation in the bidentate ligand coordination configurations of Ac-L-Cys with thiolate and either carboxylate or acetylcarbonyl groups is most likely responsible for the CD inversion, consistent with the FTIR study. The relative stability with respect to the coordination configurations on the enantiomeric HgS surface was proposed with the aid of first-principles calculations, leading a shift in the distribution of NPs formation to change the relative population of NPs with opposite handedness through the ripening processes. This chirality inversion system casts an important insight for my understanding in the roles of chiral ligands in the chirality induction in NPs, and indicates that the use of enantiopure ligands could not necessarily provide enantiopure HgS NPs with identical handedness. I further expect a future expansion of the present study with a ligand system capable of switching coordination modes in response to external stimuli such as light.

In Chapter 4, a detailed study on the formation and growth of α-HgS NPs led to two significant findings. First, a critical size of 5.5 nm seemed to exist for the transformation from the achiral β- to the chiral α-phase in the chiral induction stage. Second, the optical activity of HgS NPs was dependent on the preparation temperature and consequently on the average size of NPs. NPs with larger average size possessed higher enantiopurity in the handedness of the NP core structure, which was achieved by the growth of NPs aided by the Ostwald ripening process. This study not only gives an important insight into the enantioselective synthesis of nanomaterials but may also provide implications for the development of homochirality in nature, in which intrinsically chiral minerals are believed to play an important role.[12b]
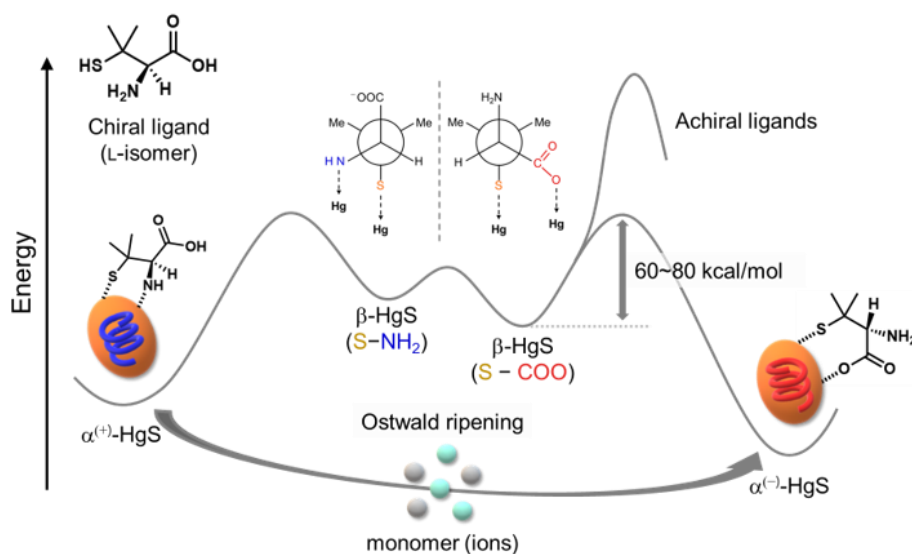
Figure 6-2. Energy diagram depicting synthesis of HgS NPs in the presence of chiral ligands.

Based on the studies in these chapters, the overall α-HgS NP formation mechanism, involving the chirality induction, can be formulated (Figure 6-2). The addition of thioacetamide to an aqueous solution of mercury ions in the presence of thiolate ligands leads to the immediate formation of kinetically favored HgS NPs with the metastable β-phase.[7] The β-HgS NPs have a spherical or polyhedral shape with diameter less than 5.5 nm (Chapter 4), and subsequently grow by mercury sulfide monomer attachment. The energy barrier of the growth is affected by a slight difference in the chemical structure of chiral ligands. The growth and formation of α-HgS NPs capped with (D, L)-cysteine (Cys), Ac-L-Cys, and *N*-isobutyryl-L-cysteine (Ib-L-Cys) could be observed at higher temperature (~50 ºC), while those events occurred even at room temperature and lower for (D, L)-penicillamine-(Pen) capped NPs (Chapter 2, 4). Since surface ligands regulate the growth of inorganic NP cores through continuous interactions with their topmost surface atoms, these cysteine-based derivatives may possess different binding affinity associated with the difference in their chemical structures. The growth of HgS NPs of size over 5.5 nm induced the β-to-α phase transformation (chirality induction) in the presence of chiral ligands (Chapter 4). In other words, the most stable phase is shifted from the cubic β-phase to the trigonal α-phase across the NP size of 5.5 nm. However, there has been some reports on the synthesis of β-HgS NPs with larger size than 5.5 nm by using achiral ligand molecules.[13-16] It might be suggested that the energy barrier of the chirality induction for achiral ligand-capped β-HgS NPs are remarkably higher, as compared to that for the NPs capped with chiral ligands. The intermediate of the β-to-α phase transformation should have a dissymmetrically distorted structure in the NP core. It is reasonable to assume that chiral surface ligands decrease the activation barrier of the transformation. As mentioned in Chapter 4, the dissipation of β-HgS NPs in the presence of D-Pen was monitored by the decrease of absorbance at 600 nm, which led to a rough estimation of metacinnabar content between 100 and 0% (Figure 4-3). This dissipation implies the β-to-α phase

transformation of the HgS NP along with NP growth (Chapter 4). The time-dependent absorption measurements were performed at four different temperatures (25, 30, 35 and 40 ºC). Plots of ln(absorbance) versus time yielded a straight line (Figure 6-3a), thus roughly indicating an apparent first order kinetics. Rate constants $k(T)$ were obtained by determining the initial reaction rates by linear fits (Table 6-1). The Arrehenius plot (Figure 6-3b) gives a linear fit (weighted linear regression), and the activation energy is determined to be 62.6 kJ/mol. Similar measurements were conducted for the NPs prepared with L-Pen, resulting in the activation energies of 74.1 kJ/mol (Figure 6-4 and Table 6-1). These values are difficult to put in context due to the mere lack of data (This is a first study to estimate the activation barrier for chirality induction of inorganic NPs).

On the basis of the bidentate coordination mode, the chiral cysteine-derivative ligand can give both handedness of $\alpha^{(+)}$- and $\alpha^{(-)}$-HgS NPs with different stability (Chapter 3). The bidentate coordination of the ligand could give nearly mirror-image coordination configurations on the NP surface. The difference in chemical structures of these ligands gives an effect on the relative populations between $\alpha^{(+)}$- and $\alpha^{(-)}$-HgS cores (Chapter 2). For example, the bulky isopropyl group in Ib-L-Cys should hamper the coordination of the acetylcarbonyl group to the surface of NPs, and Ib-L-Cys is considered to bind selectively in the thiolate−carboxylate (S−COO) bidentate coordination, leading to α-HgS NP ensembles with higher enantiomeric excess (*ee*) compared to the three other ligands (Chapter 3). Contrarily, Ac-L-Cys afforded two bidentate coordination configurations, S−COO and thiolate−acetylcarbonyl (S−Ac), on β-HgS NPs, and consequently gave a small *ee* in the NPs. From these findings, I concluded that the *ee* value of resulting α-HgS NPs could be determined by an energy difference in bidentate coordination configurations on the surface of β-HgS NPs. The study on the chiral memory effect in Chapter 2 showed that racemization cannot occur for the α-HgS NPs even with achiral ligands, indicating an insurmountable energy barrier for inversion of the handedness of the chiral crystalline structure. In fact, there have been no report on chirality inversion of inorganic NPs except for ultrasmall metal nanoclusters (size < 4 nm).[17-19] Therefore, the chirality inversion of NPs does not seem to proceed with atomic displacement in a single NP. The mode of ligand-coordination structures should differentiate the relative stability (surface energy) between $\alpha^{(+)}$- and $\alpha^{(-)}$-HgS NPs (Chapter 4). In Ostwald ripening, NPs with lower stability dissolved more rapidly providing monomeric species to the growing NPs with opposite crystal handedness. The inversion of relative population between $\alpha^{(+)}$- and $\alpha^{(-)}$-HgS NPs with the aid of ripening process was observed, leading to the optical activity inversion (Chapter 3). Moreover, the amplification of enantioselectivity for Pen-capped α-HgS NPs can be achieved through the Ostwald ripening (Chapter 4). As the dissolution of minor $\alpha^{(-)}$-HgS NPs required excess thermal energy, which was facilitated at a higher temperature, the optical activity was dependent on preparation-temperature. Thus, the chirality of the NPs, unequal population between right- and left-handedness of α-HgS cores, can be controlled by Ostwald ripening.
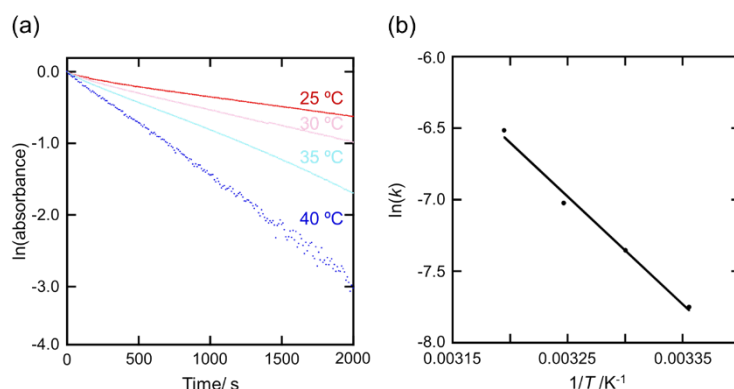
Figure 6-3. (a) Linear dependence of ln(absorbance) versus reaction time for the β-to-α phase transformation of the D-Pen-capped HgS NPs at different temperatures. (b) Arrhenius plot ln(k) vs. $1/T$ for the phase transformation at 25, 30, 35, and 40 °C.

Table 6-1. Initial reaction rate constants of the β-to-α phase transformation of HgS NPs at different temperatures.

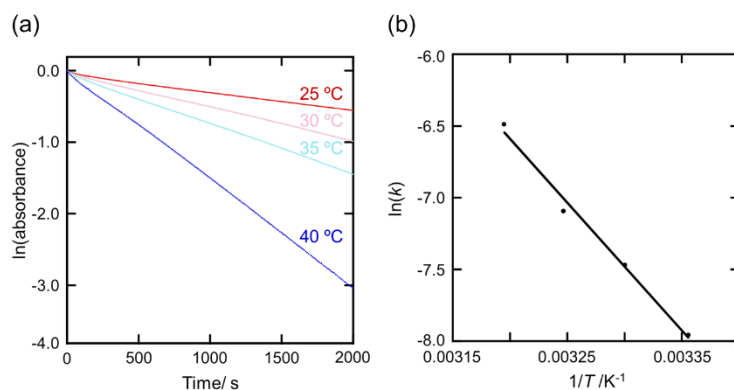|	k_{intial}			
	25 °C	30 °C	35 °C	40 °C
D-Pen	3.5	5.7	8.3	15.2
L-Pen	4.3	6.4	8.9	14.8
				$(\times 10^{-4})$

Figure 6-4. (a) Linear dependence of ln(absorbance) versus reaction time for the β-to-α phase transformation of the L-Pen-capped HgS NPs at different temperatures. (b) Arrhenius plot ln(k) vs. $1/T$ for the phase transformation at 25, 30, 35, and 40 °C.

In this dissertation research, I explored the mechanism to translate chirality of surface ligands to HgS NPs, and finally propose the three important roles of the chiral ligands: (1) differentiation in the stability of achiral β-HgS NPs with different ligand coordination modes (determination of handedness); (2) lowering the activation energy for the β-to-α phase transformation (chirality induction); (3) enantioselective stabilization of α-HgS NPs resulting in the facilitation of Ostwald ripening (control of chirality).

In Chapter 5, I developed a new approach to generate a CPL-active materials system composed of a chiral inorganic nanoparticle and achiral fluorescent ligands. The achiral fluorescent molecule adsorbed on the surface of α-HgS nanotwists (NTs) exhibited noticeable CPL signals depending on the morphological chirality of NTs. The α-HgS NTs could possess the both handedness in the crystalline lattice and nanoparticle morphology. This work demonstrated that the latter handedness played a key role in the chirality transfer from the curved surface of NTs to the arrangement of achiral luminophores. Further design of organic luminescent molecules with appropriate coordinating groups would demonstrate the utility of the present chiral-inorganic and organic hybrid system as a versatile CPL generation system.

This thesis offers deeper understanding of the mechanism to translate chirality of surface ligands to HgS NPs (Chapter 2-4), and is expected to have significant impacts on further advancement of nanoscience and nanotechnology in general. In addition to these studies, I succeeded in chirality transfer from α-HgS NPs to an achiral surface molecule, proposing a possible application, CPL-active material, of intrinsically chiral NPs (Chapter 5).

6-2. References.

1   T. G. Schaaff, G. Knight, M. N. Shafigullin, R. F. Borkman, R. L. Whetten, Isolation and Selected Properties of a 10.4 kDa Gold: Glutathione Cluster Compound, *J. Phys. Chem. B* **1998**, 52, 10643–10646.

2   T. G. Schaaff, R. L. Whetten, Giant Gold−Glutathione Cluster Compounds: Intense Optical Activity in Metal-Based Transitions, *J. Phys. Chem. B* **2000**,104, 2630 –2641.

3   S. Knoppe, T. Bürgi, Chirality in Thiolate-Protected Gold Clusters, *Acc. Chem. Res.* **2014**, 47, 1318–1326.

4   J. Kumar, K. G. Thomas, L. M. Liz-Marzán, Nanoscale chirality in metal and semiconductor nanoparticles, *Chem. Commun.* **2016**, 52, 12555–12569.

5   M. P. Moloney, Y. K. Gun'ko, J. M. Kelly, Chiral highly luminescent CdS quantum dots, *Chem. Commun.* **2007**, 38, 3900–3902.

6   F. P. Milton, J. Govan, M. V. Mukhina, Y. K. Gun'ko, The Chiral Nano-World: Chiroptically Active Quantum Nanostructures. *Nanoscale Horiz.* **2016**, 1, 14−26.

7   A. Ben-Moshe, A. O. Govolov, G. Markovich, Enantioselective Synthesis of Intrinsically Chiral Mercury Sulfide Nanocrystals. *Angew. Chem., Int. Ed.* **2013**, 52, 1275−1279.

8   B. Pal, S. Ikeda, B. Ohtani, Photoinduced Chemical Reactions on Natural Single Crystals and Synthesized Crystallites of Mercury(II) Sulfide in Aqueous Solution Containing Naturally Occurring Amino Acids, *Inorg. Chem*. **2003**, 42, 1518–1524.

9   H. Shindo, Y. Shirota, K. Niki, T. Kawasaki, K. Suzuki, Y. Araki, A. Matsumoto, K. Soai, Asymmetric Autocatalysis Induced by Cinnabar: Observation of the Enantioselective Adsorption

of a 5-Pyrimidyl Alkanol on the Crystal Surface, *Angew. Chem., Int. Ed*. **2013**, 52, 9135–9138.

10   I. Dolamic, B. Varnholt, T. Bürgi, Chirality transfer from gold nanocluster to adsorbate evidenced by vibrational circular dichroism, *Nat. Commun*. **2015**, 6, 7117.

11   X. Wei, J. Liu, G. -J. Xia, J. Deng, P. Sun, J. J. Chruma, W. Wu, C. Yang, Y. -G. Wang, Z. Huang, Enantioselective photoinduced cyclodimerization of a prochiral anthracene derivative adsorbed on helical metal nanostructures, *Nat. Chem.* **2020**, 12, 551−559.

12   D. S. Sholl, A. J. Gellman, Developing Chiral Surfaces for Enantioselective Chemical Processing. *AIChE J*. **2009**, 55, 2484−2490.

13   H. Wang, J. Zhu, A sonochemical method for the selective synthesis of α-HgS and β-HgS nanoparticles, *Ultrason. Sonochem*. **2004**, 11, 293−300.

14   W. Xu, S. Lou, S. Li, H. Wang, H. Shen, J. Z. Niu, Z. Du, L. S. Li, *Colloid Surf. A Physicochem. Eng. Asp*. **2009**, 341, 68−72.

15   A. Judy-Azar, S. Mohebbi, An easy route to synthesize superfine metacinnabar (β-HgS) semiconductor nanoparticles and their optical properties, *Mat. Lett*. **2013**, 106, 233−237.

16   S. D. Oladlpo, B. Omondl, Mercury(II) *N,N′*-diarylformamidine dithiocarbamates as single-source precursors for the preparation of oleylamine-capped HgS nanoparticles, *Transit. Met. Chem*. **2020**, 45, 391−402.

17   H. Qian, W. T. Eckenohoff, Y, Zhu, T. Pintauer, R. Jin, Total Structure Determination of Thiolate-Protected Au_{38} Nanoparticles, *J. Am. Chem. Soc*. **2010**, 132, 8280–8281.

18   S. Malola, H. Häkkeinen, Chiral Inversion of Thiolate-Protected Gold Nanoclusters via Core Reconstruction without Breaking a Au−S Bond, *J. Am. Chem. Soc*. **2019**, 141, 6006–6012.

19   S. Pollitt, V. Truttmann, T. Haunold, C. Garcia, W. Olszewski, J. Llorca, N. Barrabés, G. Rupprechter, The Dynamic Structure of $Au_{38}(SR)_{24}$ Nanoclusters Supported on CeO_2 upon Pretreatment and CO Oxidation, *ACS Catal*. **2020**, 10, 6144–6148.

Acknowledgement

Publications

1   J. Kuno, T. Kawai, T. Nakashima "The effect of surface ligands on the optical activity of mercury sulfide nanoparticles" *Nanoscale*, 2017, 9, 11590.

2   J. Kuno, Y. Imamura, M. Katouda, M. Tashiro, T. Kawai, T. Nakashima, "Inversion of Optical Activity in the Synthesis of Mercury Sulfide Nanoparticles: Role of Ligand Coordination" *Angew. Chem., Int. Ed*., 2018, **57**, 122022.

3   J. Kuno, K. Miyake, S. Katao, T. Kawai, T. Nakashima, "Enhanced Enantioselectivity in the Synthesis of Mercury Sulfide Nanoparticles through Ostwald Ripening", *Chem. Mater*., 2020, **32**, 8412. (Cover)

4   Y. Hashimoto, T. Nakashima, J. Kuno, M. Yamada, T. Kawai, "Dynamic Modulation of Circularly Polarized Luminescence in Photoresponsive Assemblies" *ChemNanoMat*, 2018, **4**, 815.

5   C. Martin, M. Minamide, J. Calupitan, R. Asato, J. Kuno, T. Nakashima, G. Rapenne, T. Kawai, "Terarylenes as Photoactivatable Hydride Donors", *J. Org. Chem*., 2018, **83**, 13700.